MATERIALS CHARACTERIZATION AND ANALYSIS COLLECTION

Richard Brundle, *Collection Editor*

A Practical Guide to Transmission Electron Microscopy

Fundamentals

Zhiping Luo

MOMENTUM PRESS ENGINEERING

A Practical Guide to Transmission Electron Microscopy

A Practical Guide to Transmission Electron Microscopy

Fundamentals

Zhiping Luo

MOMENTUM PRESS
ENGINEERING

A Practical Guide to Transmission Electron Microscopy: Fundamentals
Copyright © Momentum Press®, LLC, 2016

All rights reserved. No part of this publication may be reproduced, stored in a retrieval system, or transmitted in any form or by any means—electronic, mechanical, photocopy, recording, or any other except for brief quotations, not to exceed 250 words, without the prior permission of the publisher.

First published in 2016 by
Momentum Press, LLC 222
East 46th Street, New York, NY 10017
www.momentumpress.net

ISBN-13: 978-1-60650-703-2 (paperback)
ISBN-13: 978-1-60650-704-9 (e-book)

Momentum Press Materials Characterization and Analysis Collection

DOI: 10.5643/9781606507049

Collection ISSN: 2377-4347 (print)
Collection ISSN: 2377-4355 (electronic)

Cover and interior design by S4Carlisle Publishing Services
Private Ltd., Chennai, India

First edition: 2016

10 9 8 7 6 5 4 3 2 1

Printed in the United States of America.

Dedicated to

My dear parents, who taught
me the diligence—no matter
what kind of job it is.

Abstract

Transmission electron microscope (TEM) is a very powerful tool for characterizing various types of materials. Using a light microscope, the imaging resolution is at several hundred nanometers, and for a scanning electron microscope, SEM, at several nanometers. The imaging resolution of the TEM, however, can routinely reach several angstroms on a modem instrument. In addition, the TEM can also provide material structural information, since the electrons penetrate through the thin specimens, and chemical compositional information due to the strong electron–specimen atom interactions. Nowadays, TEM is widely applied in diverse areas in both physical sciences (chemistry, engineering, geosciences, materials science, and physics) and life sciences (agriculture, biology, and medicine), playing a key role in research or development for material design, synthesis, processing, or performance.

This book provides a concise practical guide to the TEM user, starting from the beginner level, including upper-division undergraduates, graduates, researchers, and engineers, on how to learn TEM efficiently in a short period of time. It is written primarily for materials science and engineering or related disciplines, while some applications in life sciences are also included. It covers most of the areas using TEM, including the instrumentation, sample preparation, diffraction, imaging, analytical microscopy, and some newly developed advanced microscopy techniques. In each topic, a theoretical background is firstly briefly outlined, followed with step-by-step instructions in experimental operation or computation. Some technical tips are given in order to obtain the best results. The practical procedures to acquire, analyze, and interpret the TEM data are therefore provided. This book may serve as a textbook for a TEM course or workshop, or a reference book for the TEM user to improve their TEM skills.

Keywords

Analytical Electron Microscopy; Ceramics; Chemical Analysis; Chemistry; Composites; Crystallography; Electron Diffraction; Electron Energy-Loss Spectroscopy (EELS); Forensic Science; Geosciences; Imaging; Industry; Life Sciences; Materials Science and Engineering; Metals and

Alloys; Microstructure; Nanomaterials; Nanoscience; Nanotechnology; Physics; Scanning Transmission Electron Microscopy (STEM); Polymer; Structure; Transmission Electron Microscopy (TEM); X-ray Energy-Dispersive Spectroscopy (EDS).

Contents

Preface .... *xiii*
Acknowledgments .... *xv*
About the Book .... *xvii*
Personnel Experiences with TEM .... *xix*

Chapter 1 Introduction 1
1.1 Microscope Resolution 2
1.2 Interactions of Electrons with Specimen 4
1.3 Comparison of TEM with Other Microscopy Techniques 6
References 11
Chapter 2 Sample Preparation 13
2.1 Material Samples 14
2.1.1 TEM Grids 15
2.1.2 Ion Milling 20
2.1.3 Electropolishing 26
2.1.4 Focused Ion Beam 30
2.1.5 Microtomy 31
2.2 Biological Samples 36
2.2.1 Particulate Samples 37
2.2.2 Cells and Tissue Samples 39
References 42
Chapter 3 Instrumentation and Operation 45
3.1 Construction 45
3.1.1 Electron Gun 45
3.1.2 Electromagnetic Lens 49
3.1.3 Condenser Lenses and Condenser Apertures 52
3.1.4 Objective Lens and Objective Aperture 55
3.1.5 Intermediate Lens and Diffraction Aperture 57

3.1.6 Projector Lens 59
3.1.7 Viewing Screen and Camera 59
3.2 Instrument Imperfections, Alignments, Corrections, and Calibrations 60
3.2.1 Beam Shift and Beam Tilt 60
3.2.2 Spherical Aberration 61
3.2.3 Chromatic Aberration 62
3.2.4 Depth of Field and Depth of Focus 63
3.2.5 Specimen Height 64
3.2.6 Astigmatism 65
3.2.7 Aperture Alignment 68
3.2.8 Magnification Calibration 69
3.2.9 Camera Length Calibration 71
3.2.10 Magnetic Rotation Calibration 75
3.3 TEM Operating Procedures 76
3.3.1 Startup 76
3.3.2 Specimen Loading and Unloading 76
3.3.3 Alignments 77
3.3.4 Data Recording 78
3.3.5 Finishing 78
References 79

Chapter 4 Electron Diffraction I 81
4.1 Formation of Electron Diffraction 82
4.2 Reciprocal Space 84
4.3 Indexing of Electron Diffraction Patterns 88
4.3.1 Indexing of Powder Patterns 88
4.3.2 Indexing of Single-Crystal Diffraction Patterns 90
4.3.3 Indexing of Compound Patterns: Twins 92
4.3.4 Indexing of Compound Patterns: Multiple Phases 96
4.3.5 Indexing of Compound Patterns: Double Diffraction 98
4.4 Experimental Procedures 101
4.5 Simulation of Diffraction Patterns 103

References 105
Chapter 5 Imaging I 109
5.1 Imaging Contrast 109
5.2 Imaging with Mass-Thickness Contrast 110
5.3 Imaging with Diffraction Contrast 111
5.3.1 Formation of Diffraction Contrast 111
5.3.2 Central Dark-Field Imaging 114
5.3.3 Two-Beam Condition 115
5.3.4 Bragg-Diffracted Beam Intensity 117
5.3.5 Thickness Fringes 120
5.3.6 Bend Contours 122
5.3.7 Weak-Beam Dark-Field Imaging 122
5.3.8 Planar Defects 125
5.3.9 Dislocations 127
References 137

Appendices
Appendix I. SAED Indexing Table of Primitive Cubic Structure ... 139
Appendix II. SAED Indexing Table of Body-Centered Cubic Structure 141
Appendix III. SAED Indexing Table of Face-Centered Cubic Structure 143
Appendix IV. SAED Indexing Table of Close-Packed Hexagonal Structure 145
Illustration Credits 147
Index 149

Preface

To study material structure, we need to use microscopes. With the naked eyes, we can barely see objects beyond 0.1 mm, while by using a light microscope composed of optical lenses, the resolution is improved beyond 1 μm to several hundred nanometers. However, to further improve the resolution, electron microscopy should be applied. Scanning electron microscopy (SEM) extends the resolution to several nanometers, and it can also provide elemental analyses, but it is hard to see objects below the several nanometer range. The transmission electron microscopy (TEM) has great advantages over other microscopy techniques, in that its ultrahigh imaging resolution can routinely reach several angstroms on a modern microscope, and it also has ability to study the structure using electron diffraction, and auxiliary capabilities to identify chemical compositions. Nowadays, TEM is a standard characterization approach in scientific research, academic education, industrial development, and governmental forensic investigations.

For over a decade at Texas A&M University, I held a TEM instrumental scientist position, where I taught TEM courses and trained many TEM users. During the user training, I realized that step-by-step instructions were always very helpful so that the user could work in the right way immediately, instead of learning from many trials. The users should learn the instructions first and then practice on the instrument to improve the working efficiency, rather than practice with minimum instructions.

This book provides a practical guide to the TEM user as a quick reference on how to utilize the various TEM techniques more efficiently to get meaningful results. It starts at the beginner level and introduces the TEM skills concisely, including practical instructions on how to operate the instrument correctly, how to avoid possible problems, how to understand the results, and how to interpret and compute the data. It is separated into two volumes with different levels. Volume 1 is on Fundamentals of TEM, including TEM sample preparation, instrumentation and operation procedures, electron diffraction I (selected-area electron diffraction), and imaging I (mass-thickness imaging and diffraction contrast

imaging). Volume 2 covers Advanced Microscopy, including electron diffraction II (Kikuchi diffraction, convergent-beam electron diffraction, and nano-beam electron diffraction), imaging II (scanning transmission electron microscopy, and high-resolution electron microscopy), analytical electron microscopy for elemental analyses, and some new developments and specific applications.

I hope you enjoy the power of the TEM. May TEM assist your research, provide you with good results, and bring you good luck in your career!

Zhiping Luo
Fayetteville, North Carolina
June 2015

Acknowledgments

First of all, I acknowledge my many collaborators who provided me with wonderful samples for the TEM investigations and made fruitful discussions on what we learned from the TEM. It is really hard to list all of their names on this page, while the following major contributors are apparently among them, alphabetically, Drs. M. Akbulut, S. Bashir, J. Batteas, L. Carson, C.C. Chen, W. Chen, D. Fang, J. Fang, B. Guo, Z. Guo, K.T. Hartwig, A. Holzenburg, X. Hong, X. Jiang, H.E. Karaca, I. Karaman, B. Kockar, J.H. Koo, A. Kronenberg, S. Kundu, D. Lagoudas, G. Liang, Y. Li, J. Liu, J. Ma, A.-J. Miao, D.J. Miller, J.F. Mitchell, O. Ochoa, A. Oki, V. Paredes-García, Z. Quan, P.H. Santschi, R.E. Schaak, L. Shao, D.H. Son, C. Song, Y. Song, L. Sun, X.S. Sun, Y. Tang, Y. Vasquez, H. Wang, W. Wu, J. Zhang, S. Zhang, X. Zhang, Q. Zhai, D. Zhao, H. Zheng, H.-C. Zhou, D. Zhu, J. Zhu, and M. Zhu.

I also thank my previous colleagues (Dr. A. Holzenburg, Mr. R. Littleton, Ms. A. Ellis, Dr. C. Savva, Dr. J. Sun, Dr. S. Vitha, Dr. H. Kim, etc.) at the Microscopy and Imaging Center, Texas A&M University for technical assistance and stimulating discussions on biological samples; Dr. D.J. Miller at the Electron Microscopy Center, Argonne National Laboratory, for advanced TEM skills; and Profs. H. Hashimoto and E. Sukedai at Okayama University of Science, Japan, for HREM.

Grateful appreciations should also be given to those professors who introduced me to the field of electron microscopy in my early career in China, alphabetically, Drs. K.H. Kuo, F.H. Li, and S. Zhang.

Finally, I am grateful to the book Collection Editor Dr. C. Richard Brundle for technical assistance to edit this book, and to those publishers for their permissions to reuse the materials presented in this book as specifically referenced.

About the Book

- This book is a concise practical guide for the TEM users to improve TEM skills in a short period of time.
- It is also a textbook for a short course (semester-long TEM undergraduate or graduate course, or intensive short-term workshop).
- It provides step-by-step instructions how to operate the instrument, how to analyze, and how to compute the data.
- It covers areas primarily for physical sciences (chemistry, engineering, geosciences, materials science, and physics) and some examples in life sciences (agriculture, biology, and medicine).
- It applies to scientific research, academic education, industrial developments, governmental forensic investigations, and others.

Personnel Experiences with TEM

1. Be aware of what you are doing with the microscope!
   - Read sufficient literature to make clear what is new and what has been done previously.
2. See both, the forest and the trees!
   - Information in both high and low magnifications should be known.
3. Good results are obtained out of the microscope room!
   - Post-experiment analyses (data processing, computation, and quantification) and documentation are very important.
4. A good habit is beneficial to your whole career!
   - Organize your samples and data well.

CHAPTER 1

Introduction

To reveal small objects that are beyond the visual capacity of human eyes, various microscopy techniques have been developed. Without the help of any instrument, the resolution of naked eyes is only about 0.1 mm, or 100 μm. The early developed light microscope (LM) is used to magnify objects by optical lenses using visible lights. The resolution of LM can be improved to below 1 μm at several hundred nanometers. After the LM technique, it was discovered that electrons could be used as the illumination source to improve the imaging resolution, and therefore various electron microscopy (EM) techniques have been developed to study different types of samples. Among them, bulk samples can be analyzed by scanning electron microscope (SEM), electron probe microanalyzer (EPMA) or electron microprobe analyzer (EMPA), or scanning Auger microscope (SAM) or scanning Auger microprobe (SAM). In these techniques, various detected signals come from the electron–specimen interactions. If the sample is thin enough, the electrons can penetrate right through the samples to form images using electromagnetic lenses. The instrument imaging samples using transmitted electrons is named as transmission electron microscope (TEM), and this technique is named as transmission electron microscopy (TEM). Nowadays the terminology TEM can mean either the microscope or the technique.

TEM is a very powerful tool to study the sample structures [1–6]. It can provide not only a high imaging resolution down to angstroms or even subangstrom level but also structural information through electron diffraction, and chemical composition information through the interactions of high-energy electrons with core electrons of the specimen. TEM has been widely applied in multidisciplines, including physical sciences (chemistry, engineering, geosciences, materials science, and physics) and life sciences (agriculture, biology, and medicine), and for technical development, product inspection, and forensic investigations.

1.1 Microscope Resolution

Fig. 1.1(a) illustrates that an object is magnified by a convex lens. Note that the magnified image is upside down with respect to the object. If the lens is perfect without any aberration, as shown in Fig. 1.1(b), a point object is imaged as a series of concentric rings due to a diffraction effect, rather than a single image dot. The central spot has high intensity, while the intensities of outer rings are attenuated. These rings are termed as an Airy disk or Airy pattern.

To discuss the resolution, we need to consider at what distance two image spots can be distinguished. For simplicity, we consider only the intensity profile of the central image spot that ends at the first zero (Fig. 1.1b). If these two image spots are far away without any overlap of their intensity profiles, as shown in Fig. 1.1(c), or even when minimum-intensity positions reach together, as shown in Fig. 1.1(d), the sum of their intensity profiles is the same as their individual intensities because there is no overlap of their intensity profiles. These two spots are, of course, well resolved. When they are getting closer, as shown in Fig. 1.1(e), the image intensity of the overlapped area is the sum of two intensities, as shown in dotted lines. They still remain resolved. If these two spots move even closer and when the maximum position of one spot meets the minimum position of another spot, as shown in Fig. 1.1(f), then it is a critical position to resolve these two spots. This condition is the Rayleigh criterion, and the distance δ is the microscope resolution.

$$\delta = \frac{0.61\lambda}{n\sin\alpha} \tag{1.1}$$

Here, λ is the wavelength, n is the refractive index of the medium between the sample and lens, and α is the semi-angle of collection of the magnifying lens. The product $n\sin\alpha$ is known as numerical aperture (NA). If these two image spots are spaced closer than the distance δ, as shown in Fig. 1.1(g), the overlapped intensity profile exhibits only one peak, that is, the two spots are not resolved.

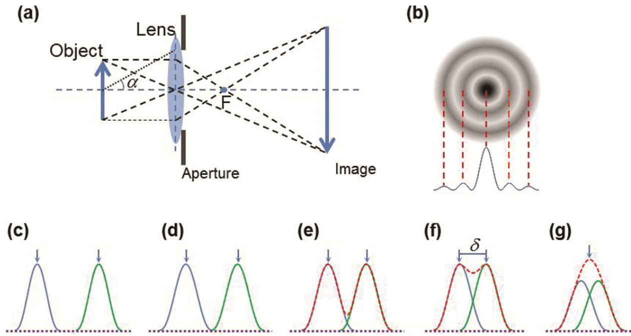

***Fig. 1.1** Image formation by a lens (a) and formation of Airy disks from a single image spot by diffraction effect (b). Separation of two image spots is shown in (c–g) with a series of different distances. The microscope resolution is defined in (f) for Rayleigh criterion that the minimum intensity of one spot coincides with maximum intensity of another spot.*

A better resolution means a shorter distance δ for identifying two image points. From Eq. 1.1, it is possible to improve the resolution (or decreasing δ) through the following methods:

1. Increasing the NA by using medium with higher refractive index *n*. The *n* of vacuum is 1, and air is also very close to 1. However, for some liquids, the *n* is normally greater than 1. Therefore, immersion oil, with *n* approximately 1.516, is used in LM to improve microscope resolution. However, such oil cannot be used in the electron microscopes.
2. Decreasing the wavelength λ by using different illumination sources. The wavelength of visible light ranges from about 390 to 700 nm (violet to red). The ultraviolet (UV) source has shorter wavelength λ in the range of 10 to 400 nm. If UV is used, the resolution can be somehow improved. Although X-rays have short wavelength (0.154 nm for Cu Kα), they cannot be focused for imaging. Electrons, however, have even shorter wavelengths of 0.0123 nm at 10 kV, or 0.0025 nm at 200 kV, and they can be deflected to focus images. The improvement of the resolution using electrons is huge.

It should be mentioned that the resolution in Eq. 1.1 is diffraction-limited resolution of an optical system, without considering the aberration or distortion in the optical system. If aberrations and distortions are present in the system, they degrade the microscope resolution.

1.2 Interactions of Electrons with Specimen

Upon bombardment of electrons on the specimen, the high-energy incident electrons strongly interact with the specimen atoms [7] to generate various signals, as shown in Fig. 1.2(a). The following types of signals are formed:

1. Transmitted electrons, including unscattered, elastically scattered (without energy loss), and inelastically scattered (with energy loss) electrons. These electrons contain the major information in TEM for (i) electron diffraction, including selected-area electron diffraction (SAED), convergent-beam electron diffraction (CBED), Kikuchi diffraction, and nano-beam electron diffraction (NBED); and

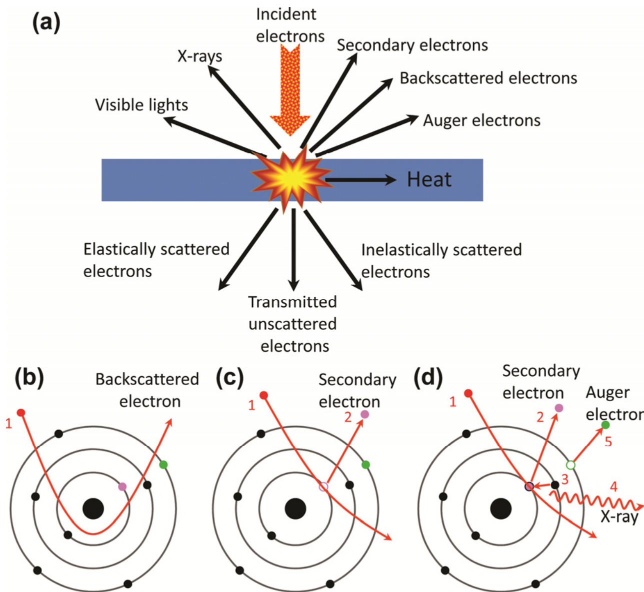

Fig. 1.2 Interaction of electrons with specimen to generate various signals (a), and formation of backscattered (b), secondary (c), and Auger electrons and X-rays (d).

(ii) imaging, including mass-thickness contrast imaging, diffraction-contrast imaging, Z-contrast imaging in scanning transmission electron microscopy (STEM), and phase-contrast or high-resolution TEM (HRTEM) or high-resolution electron microscopy (HREM). In addition, by analyzing the energy loss of the transmitted electrons, chemical information can be obtained by electron energy-loss Spectroscopy (EELS). All these techniques will be explained later.

2. Other signals of backscattered electrons, secondary electrons, and Auger electrons, as shown in Fig. 1.2(b–d), respectively. The backscattered electrons are original primary incident electrons, which are scattered backward due to the interactions with the sample atomic nucleus (Fig. 1.2b). If the incident electrons collide and eject inner shell electrons, as shown in Fig. 1.2(c), the electrons knocked off by incident electrons are secondary electrons, that is, they are not the primary incident electrons but they are from the specimen atoms. If the inner shell electrons are ejected, these atoms are in an ionized state, and subsequently the inner shell vacancy is filled by an electron from outer shell with a higher energy level, generating an energy surplus (Fig. 1.2d). Therefore, either X-rays are emitted, or Auger electrons (the third electrons) can also escape from the sample surface to use up this excess energy. Auger electrons escape from the surface with a kinetic energy characteristic of the parent atom. In TEM, the backscattered, secondary, and Auger electrons are normally not used although it is possible to use secondary electrons [8] in STEM. In fact, the secondary and the backscattered electrons are primarily used for imaging by secondary electron imaging (SEI) and backscatter imaging (BSI) detectors in SEM or EPMA, and Auger electrons with the kinetic energy are analyzed by Auger electron spectroscopy (AES) in SAM [9].
3. Visible lights, which are generated by cathodoluminescence (CL) phenomenon during the interaction of high-energy electrons with specimen. The CL can be used in TEM to study the sample optical properties [10, 11]. It is more commonly used in SEM or EPMA for bulk samples due to the much stronger electron–specimen interactions than the thin specimens.

4. X-rays, including characteristic X-rays and Bremsstrahlung (continuum) X-rays, are formed by incident electrons with core electrons of specimen atoms. The X-rays are used for chemical analysis by X-ray energy-dispersive spectroscopy (XEDS or EDS). In SEM or EPMA, such X-rays are also used for chemical analysis by EDS and wavelength-dispersive spectroscopy (WDS), while WDS is not used for TEM since the sample is too thin to generate sufficient X-ray signals. More details about X-ray analyses will be given in Chapter 8 in Volume 2.
5. Heat generated by the electron beam, which causes the temperature rise and sometimes sample damage. If the sample is a bulk conductive metal, the heating effect is not evident. For less conductive samples, the temperature may go few hundreds Celsius degrees high [6]. It is common to observe melting of nanoparticles (including Ag and Au) in TEM. Although the melting points of bulk Ag and Au are 961.8 °C and 1,064 °C, respectively, the melting points of nanoparticles are lower than their bulk forms, so it is possible to see their melting in TEM by this heating effect. The heat is not used for analysis in TEM.

1.3 Comparison of TEM with Other Microscopy Techniques

Compared with different microscopy techniques of LM, SEM, EPMA, SAM, or atomic force microscope (AFM), the samples for TEM must be thin enough, typically thinner than 100 nm, so that the electrons can penetrate them, while there is no such requirement for other microscopes.

Each microscopy has its own unique pros and cons. A comparison of the imaging ray diagrams of TEM, SEM, AFM, LM, and slide projector is shown in Fig. 1.3. In TEM, as shown in Fig. 1.3(a), the sample is very thin, so that the electrons penetrate the sample, and the images are magnified by the following objective and projector lenses. The final image is a 2D projection of the specimen. Below are comparisons of TEM with some of these microscopy techniques.

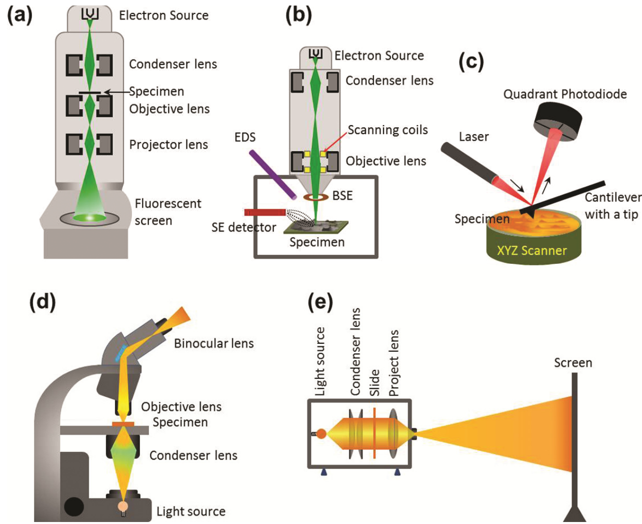

Fig. 1.3 Comparison of different magnifying methods: (a) TEM; (b) SEM; (c) AFM; (d) LM; and (e) projector.

1. *SEM, EPMA, or SAM.* In SEM or EPMA, as shown in Fig. 1.3(b), electron beam is focused to a fine spot on the sample, and the image is formed by raster scanning the electron beam to produce signals from the bulk sample surfaces, which are collected by SEI or BSI detectors. A distinct advantage of this imaging method is that the sample can be in a bulk form, without the requirement for special preparation to become transparent to electrons. This imaging mechanism is totally different from TEM using transmitted electrons. Although STEM imaging in TEM also uses focused beam that raster scans the sample in a similar way, only transmitted electrons are collected under the specimen. All these electron microscopes (SEM, EPMA, and SAM) use electromagnetic lenses to focus the electron beams. They have their specific applications. For example, EPMA is mainly for X-ray quantitative elemental analysis using WDS. The sample must be polished to be very flat at the correct height, so that the X-rays can be displayed in wavelength by detector crystals according to Bragg's law. For SAM, ultrahigh vacuum conditions are required, and AES is produced by focused incident

electrons on the sample surface generating Auger electron emission from the top few nanometers (Fig. 1.2d). Electron backscatter diffraction (EBSD) can be used to study the sample structure and orientation mapping to elucidate texture or preferred orientations. It is based on backscatter Kikuchi diffraction, which is similar to the Kikuchi diffraction in TEM in principle that will be discussed in Chapter 6 in Volume 2. To do EBSD, the sample surface must be flat and well-polished, which is placed in the SEM chamber at a highly tilted angle (~70°) horizontally toward the diffraction camera, to increase the contrast in the resultant electron backscatter diffraction pattern. The analysis of the EBSD Kikuchi pattern is similar to the Kikuchi pattern in TEM.

2. *AFM.* Unlike other microscopes to image magnified visualization, AFM imaging is conducted by using a sharp tip on a cantilever to detect the sample surfaces by touching or near touching the sample, as shown in Fig. 1.3(c). AFM can generally measure the vertical and lateral deflections of the cantilever by using an optical lever, which operates by reflecting a laser beam off the cantilever. As the sample stage scans along *XYZ* directions, the reflected laser beam strikes a position-sensitive quadrant photodiode to indicate the position of the laser spot on the detector and thus the angular deflections of the cantilever. The experiment is done at atmospheric ambient conditions, and the samples can be liquid or solid. Compared with electron microscopes, the AFM system does not use any lens and thus it is not suffered from a limitation of space resolution due to a diffraction limit or aberration. The sample is not subjected to any beam irradiation damage either, and it is also not subjected for special sample preparation with dehydration or staining. AFM can reach high resolution at nanometer scale, but it does not provide structure or chemical compositional information. It is essentially an extremely high-resolution profilometer.
3. *LM.* For imaging in LM, there are no restrictions for the sample preparation. All kinds of samples are adaptable to LM, including liquid, solid, and even gas. It can be used to image live biological samples, and it is the only imaging technique performed using a

signal that can be directly observed by eye (optical wavelengths; different colors). If the sample is a thin slice and the light goes through the sample, the imaging optics are actually similar to TEM, as shown in Fig. 1.3(c). From bottom to top, the lights travel in the sequence of light source → condenser lens → specimen → objective lens → binocular lens (projector lens), which is the same order of ray path in the TEM from top to bottom in Fig. 1.3(a). However, the resolution of LM is low, mainly due to the much longer wavelength of the illumination source.

4. *Slide projector.* The ray path of a slide projector is shown in Fig. 1.3(e). From left to right, the ray path is light source → condenser lens (two pieces of lenses combined together) → slide (specimen) → projector lens → screen. The ray path is similar to LM and TEM, except the objective lens that is missing since there is no need to focus down the beam. The magnified image is a 2D projection of the slide, which is similar to the TEM image.

A comparison of these microscopy techniques is listed in Table 1.1, and examples for SEM/TEM images are shown in Fig. 1.4. From a sample of carbon nanofiber (CNF)/polymer composite [12], the SEM image in Fig. 1.4(a) exhibits a 3D morphology of the surface with surface holes and pullouts of CNFs. No further information, such as atomic layers, can be gained if it is further magnified using this SEM. Its TEM image in Fig. 1.4(b) exhibits a 2D projection through the CNFs in the polymer matrix, a structure inside the material. At high magnifications, depending on the TEM resolution, it is possible to see the lattice fringes (refer to Chapter 7 in Volume 2 for an explanation) of CNFs, as shown in the inset. The SEM image of another sample of clay/polymer composite [13] shows well-dispersed clay sheets in the matrix (Fig. 1.4c). A further magnified SEM image shown in Fig. 1.4(d) does not reveal any detail. These clay sheets exhibit bright contrast, since they are pullouts from the surface by etching away the matrix, so that more secondary electrons emit from these sharp inclined areas. The clay sheets are not resolved in SEM. However, in the TEM image shown in Fig. 1.4(e), single or bundle of clay sheets can be easily identified.

Table 1.1 Comparison of TEM with LM, SEM, and AFM.

	TEM	LM	SEM	AFM
Sample preparation	Samples must be very thin (<100 nm). Solid or thin sliced samples should be dehydrated and preferably conductive (carbon coating needed for nonconductive samples). Liquid can be prepared by cryo-EM method.	No restriction.	Normally dehydrated and surface is coated with a thin carbon or metal layer if nonconducting. Hydrated samples can be done using low-vacuum mode, special capsules, or cryo-SEM.	No restriction.
Resolution	Angstroms or sub-angstroms.	Sub-micrometers.	Nanometers.	Vertical: angstroms to 1 nm; Lateral: nanometers
Imaging	Mass-thickness contrast imaging, diffraction-contrast imaging, Z-contrast imaging in STEM, and phase-contrast in HRTEM; 2D only, except 3D reconstruction by electron tomography.	Low-magnification imaging. 2D for thin sections, or 3D using stereoscope or optical sectioning.	3D sample surface observation.	3D sample surface imaging by profiling at high resolution.
Structure	By electron diffraction or atomic imaging.	No.	By EBSD.	No.
Chemical analysis	By EDS, EELS, or STEM.	No.	EDS or WDS, while spatial resolution is lower than TEM.	No.

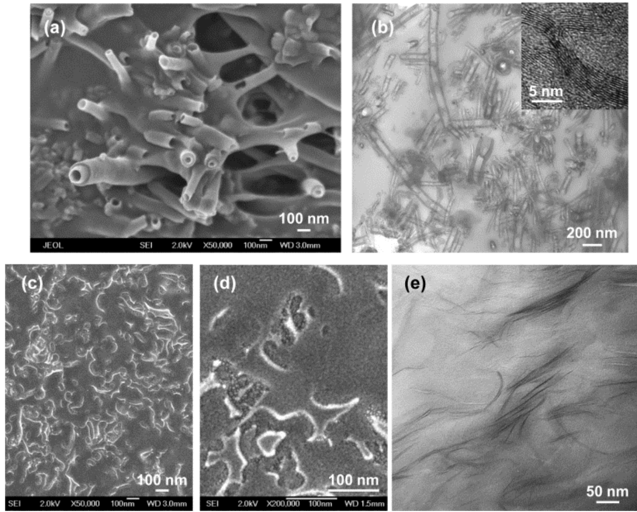

Fig. 1.4 Comparison of SEM and TEM images: SEM (a) and TEM (b) image of carbon nanofibers in polymer, and SEM (c, d) images and TEM image (e) of clay in polymer.

References

[1] P.B. Hirsch, A. Howie, R.B. Nicholson, D.W. Pashley, M.J. Whelan. *Electron Microscopy of Thin Crystals*. Krieger, Florida, 1977.

[2] G. Thomas, M.J. Goringe. *Transmission Electron Microscopy of Materials*. John Wiley & Sons, New York, 1979.

[3] J.W. Edington. *Practical Electron Microscopy in Materials Science*. Techbooks, Herndon, Virginia, 1991.

[4] L. Reimer. *Transmission Electron Microscopy: Physics of Image Formation and Microanalysis*. Springer, Heidelberg, Berlin, 1997.

[5] J.J. Bozzola, L.D. Russell. *Electron Microscopy: Principles and Techniques for Biologists*. Jones and Bartlett Learning, Massachusetts, 1999.

[6] D.B. Williams, C.B. Carter. *Transmission Electron Microscopy: A Textbook for Materials Science*. Springer, New York, 2009.

[7] J.I. Goldstein, A.D. Romig, Jr., D.E. Newbury, C.E. Lyman, P. Echlin, C. Fiori, D.C. Joy, E. Lifshin. *Scanning Electron Microscopy and X-Ray Microanalysis: A Textbook for Biologists, Materials Scientists, and Geologists*. 2nd Edition. Plenum Press, New York, 1992.

[8] H. Inada, D. Su, R.F. Egerton, M. Konno, L. Wu, J. Ciston, J. Wall, Y. Zhu. Atomic imaging using secondary electrons in a scanning transmission electron microscope: Experimental observations and possible mechanisms. *Ultramicroscopy* **111**, 865–876 (2011).

[9] J. Wolstenholme. *Auger Electron Spectroscopy: Practical Application to Materials Analysis and Characterization of Surfaces, Interfaces, and Thin Films*. Momentum Press, New York, 2015.

[10] N. Yamamoto, J.C.H. Spence, and D. Fathy. Cathodoluminescence and polarization studies from individual dislocations in diamond. *Phil. Mag.* **A49**, 609–629 (1984).

[11] D. Nakaji, V. Grillo, N. Yamamoto, T. Mukai. Contrast analysis of dislocation images in TEM–cathodoluminescence technique. *J. Electron Microsc.* **54**, 223–230 (2005).

[12] Z.P. Luo, J.H. Koo. Quantitative study of the dispersion degree in carbon nanofiber/polymer and carbon nanotube/polymer nanocomposites. *Mater. Lett.* **62**, 3493–3496 (2008).

[13] Z.P. Luo, J.H. Koo. Quantification of the layer dispersion degree in polymer layered silicate nanocomposites by transmission electron microscopy. *Polymer* **49**, 1841–1852 (2008).

CHAPTER 2

Sample Preparation

The first step to work with transmission electron microscopy (TEM) is the sample preparation, which is the most critical step to get meaningful TEM results. Basically, the prepared TEM samples should meet the following requirements:

1. To preserve the original structure of the sample, and if any artifacts are introduced, they should be at the minimum extent and are recognizable;
2. To be as thin as possible, typically at least less than 100 nm to be transparent to electron beam;
3. To be physically supported for loading and unloading to the specimen holder;
4. To be mechanically stable without causing vibrations in the TEM;
5. To be dehydrated or stay in a frozen state, so that it does not evaporate or release much vapor or gas during the observation inside the TEM vacuum chamber;
6. To be preferably electrically conductive to avoid beam charging effect causing beam damage;
7. To be surface clean with minimum contaminations.

If a sample does not meet all of these requirements, it will necessitate special efforts during the TEM operations. For example, if a sample is very beam sensitive, such as biological soft matter, low-dose imaging can be used.

Depending on the sample type, property, and the information needed to learn from TEM, many different sample preparation methods have been developed, including material samples and biological samples. Material samples refer to these samples from physical sciences, including these hard materials (metals and alloys, ceramics and composites) and soft polymers, whereas biological samples refer to those samples from life sciences,

including biological particulates, cells, and tissues. TEM sample preparation methods are classified into these two classifications although sometimes these methods are cross used, for example, the method for biological sample preparation can also be used for material samples.

2.1 Material Samples

Material samples are generally solid and dehydrated, while they can be in forms of particles, powders, wires, films, or condensed solids. Different preparation methods have been proposed, primarily by TEM grids, ion milling, electropolishing, focused ion beam (FIB), and microtomy. Table 2.1 lists a comparison of these major methods and their common applications to different materials. Depending on a particular sample, the method may change accordingly.

Table 2.1 TEM sample preparation of material samples.

	Grids	Ion milling	Electropolishing	FIB	Microtomy
Metal and alloy	No	Yes	Yes	Yes	No
Ceramic	Not common	Yes	No	Yes	No
Rock/mineral	Not common	Yes	No	Yes	No
Polymer and polymer composite	No	Yes	No	Yes	Yes, if not too hard
Metal or ceramic composite	Not common	Yes	Yes if conductive	Yes	No
Solid thin film	No	Yes	Not common	Yes	No
Powder	Yes	Yes (with embedding)	No	Yes (with embedding)	Yes (with embedding)
Particles for fibers in liquid solution	Yes	No	No	No	No

2.1.1 TEM Grids

To particle or powder samples, TEM grids should be used to provide the support. A common type of grid is 3.05 mm in diameter, whereas another type of grid is 2.3 mm in diameter. The thickness and mesh size vary. Normally the thickness is in the range of 5–30 μm. The mesh size number defines the spacing of the grid lines. For example, 100 mesh means 100 lines in an inch (25.4 mm). Table 2.2 lists the line spacing with different mesh sizes. Note that because of the bar width, the available open space is less than the line spacing listed in the table. Generally, 400 mesh grids can meet the majority needs with appropriate grid opening, whereas 150 mesh grids are normally used for large opening requirement, and 1,000 mesh grids are used for very small opening. These grids are made into different patterns, such as square, rectangular, hexagonal, or a single hole.

The TEM grids are made of different materials, such as Cu, Ni, Au, Mo, Ti, Be, and stainless steel. Normally Cu is selected because of its lower cost and it is nonmagnetic. Other metals may be selected for different purposes, for example, to analyze Cu element in the sample using energy-dispersive spectroscopy (EDS), it is preferable not to use Cu grids to avoid signals from the grids (refer to Chapter 8 in Volume 2). In the *in situ* heating experiment, if temperature is near or higher than Cu melting point (1,085 °C), Cu grids should not be used.

Some grids are coated with support films, including carbon, formvar, silicon monoxide, silicon nitride, or their combinations with different thicknesses. Some of the films are continuous, whereas some of them contain holes to eliminate the film background. Normally pure carbon is selected because of its high mechanical strength, chemical stability with specimen, and good electrical conductivity. For some special purposes to achieve better dispersion or attraction with the specimen, other types of thin film may be selected. However, if the grid film is not conductive, a final carbon coating is recommended to stabilize the film under the electron beam. Note that the support film is only coated on one side of the grids. Normally the dark side is the film side, with the labels showing correctly (such as the number "1" as indicated by an arrow in Fig. 2.1a). The support film can be easily identified using a low-magnification stereo microscope. The thickness of the film may vary greatly.

Referring to Fig. 2.1, the TEM grid preparation involves the following procedures.

Table 2.2 TEM grids' mesh size.

Mesh size	50	100	150	200	250	300	400	500	1,000	1,200	2,000
Line spacing (μm)	508	254	169	127	101.6	84.7	63.5	50.8	25.4	21.1	12.7

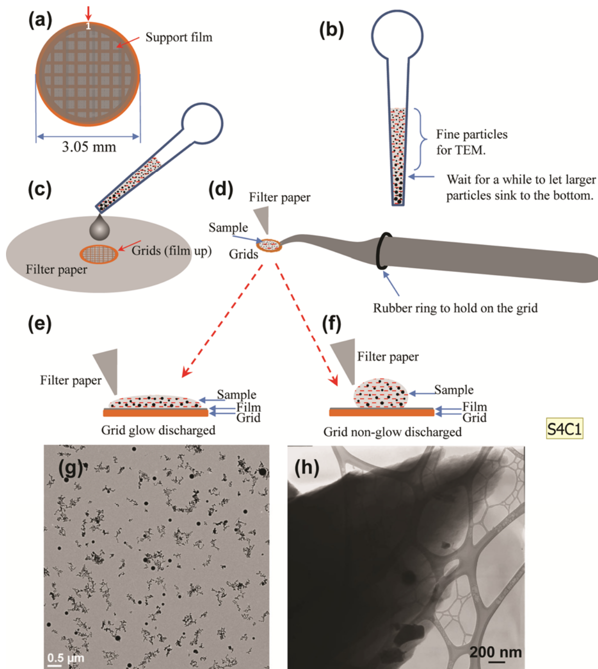

Fig. 2.1 TEM grid preparation. (a) A TEM grid with a support film coated on the top side; (b) a dropper to transfer the solution; (c) a droplet of solution is dropped onto a piece of grid on a piece of filter paper; (d) a pair of tweezers to hold a piece of upward grid and a small droplet of solution is deposited on its surface. A small piece of filter paper is used to remove any extra solution; (e) glow discharged grid with hydrophilic surface so that the droplet solution spreads on the surface; (f) non-glow discharged grid with hydrophobic surface, where the droplet does not spread on the surface; (g) TEM image of well-dispersed alumina particles on pure carbon support film; (h) a fragment of carbon fiber powders deposited on holey mesh support film.

1. *Solution preparation.* If the sample is in the form of powders, use an agate motor and a pestle to further grind the sample into finer particles if needed, and then prepare a solution using a solvent that does not react with the sample. Normally pure ethanol is used.
   Note that the solution can provide better attraction of the powder particles on the support film, when the solvent evaporates. If the powders are directly spilled on the grids, the fine particles may drop off the grids and contaminate the instrument. A carbon coating may help to retain the particles on the film to reduce the contamination.
2. *Glow discharge the TEM grids.* Place the TEM grids into a glow discharge device, with the support film facing the ion source. The glow discharge process is to provide plasma flows, generated by a high-voltage electrical filed, to clean the support film surfaces, so that the surfaces are modified from hydrophobic to hydrophilic. This process should be done in a short period of time since a long-time process may damage the film. Some devices have automatic controls for the glow discharge process.
3. *Transferring the solution onto the grids.* Use a plastic dropper or a micropipette with a tip to suck a certain amount of the prepared solution, and hold it vertically for a certain period of time (60 s or longer) to let larger particles to sink to the bottom side. Push to remove away these larger particles from the dropper (Fig. 2.1b). There are two common ways to deposit the sample on the film: (i) place the grid on a piece of filter paper with the film facing upside, and deposit a drop of solution on the grid directly, as shown in Fig. 2.1(c); (ii) hold the grid with the film side facing up using a pair of reverse tweezers, or a pair of tweezers held by a rubber ring on it (Fig. 2.1d). Then place a small droplet of solution (3–5 μL) containing fine particles on the top of support film, and use a small piece of filter paper to remove any extra solution as needed. If the grid is glow discharged, the droplet can spread on the film surface evenly (Fig. 2.1e), while if not, the droplet may not spread on the film surface, leaving a larger contact angle between them (Fig. 2.1f). If the glow discharge is not available, washing the grid using the pure solvent for several times may help to achieve better hydrophilic property. When the solution is dried, the TEM grid sample is ready for TEM experiment.

Two examples are shown here. Fig. 2.1(g) shows a TEM image of alumina particles taken at a low magnification, showing well-dispersed alumina particles on pure carbon support film. In Fig. 2.1(h), the sample was prepared by crushing carbon fibers into powders and a drop of solution, with powders in pure ethanol, was deposited onto a grid with holey mesh support film. At the edge of the wedge-shaped particle, it is thin enough for electron diffraction or high-resolution imaging.

It is noticed that *air drying* may cause some modifications on the sample during the air drying process, such as nanoparticles aggregation or change of the hydrated specimen. To avoid these artifacts, *freeze drying* should be used. Freeze drying is a dehydrating process to gradually remove the water in ice by sublimation in a low-air pressure environment. To freeze dry the TEM grid, in the process 3 mentioned previously, when a sample droplet is placed on the film surface (Fig. 2.1d), the tweezers with the grid are quickly dipped into liquid nitrogen until they are completely cooled. Then they are quickly placed into a freeze drying device, which can continue to cool the grid at a low temperature in a vacuum. When the ice on the grid disappears visibly, the water sublimation is completed, and the grid sample is ready for TEM.

If the freeze drying facility is not available, one may build a simple freeze drying device. Find a large piece of metal block, such as aluminum with relatively high specific heat (0.22 cal/g°C), and dip the metal into liquid nitrogen unit it is completely cooled, and then place it in a vacuum chamber (ensure the vacuum system works with high moisture). Quickly place the TEM grid with frozen sample on the top surface of the cooled metal, and close the chamber and pump down the air pressure of the chamber until the specimen sublimation is completed. In this case, the metal block provides the cooling source for the specimen.

Another method to dry the solution is *critical point drying*, which is done using a chemical of hexamethyldisilazane (HMDS) as follows:

1. Transfer a droplet of solution (3–5 μL) onto the grid film and wait for 30 s;
2. Wear cryogenic gloves to hold the tweezers and dip the grid into liquid nitrogen to cool the solution completely for 60 s;

3. Move the grid from the liquid nitrogen and dip it into methanol (for few seconds), followed with a dip in HMDS (for few seconds), and then evaporate it in air (in the hood).

This critical point drying method is easy to operate, but the chemical HMDS is involved to the prepared samples.

Some samples may be deposited on bare grids even without any support films, so that support film background is eliminated. In this case, bare grids with high mesh numbers (finer spacing), at least 1,000 mesh, are preferred (Fig. 2.2a). To deposit more samples on the grid bars, the grid should be held by a pair of tweezers until the solution is dried on the grid (Fig. 2.2b), instead of placing the grid on a filter paper. Sometimes it is possible to observe the sample particles attached on the grid bars, as schematically shown in Fig. 2.2(c).

The users may invent new preparation methods for special needs. Two examples are demonstrated in Fig. 2.3. In order to achieve self-assembly of nanoparticles on the TEM grid, as shown in Fig. 2.3(a), a piece of 200-mesh TEM grid with support film was held with a pair of self-closing tweezers and submerged into a hexane suspension of Pt_3Ni nanoctahedra solution in a vial [1]. The solvent was allowed to evaporate in ambient conditions until the level of the colloidal solution moved below the TEM grid so that the grid emerged out of the solution. During the evaporation process, the nanoparticles well assembled on the top surface of the TEM grid, as shown in a scanning transmission electron microscopy (STEM) image in Fig. 2.3(c), where three-layer assembly was formed.

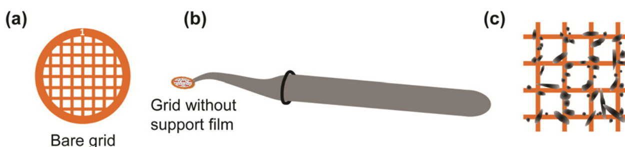

Fig. 2.2 TEM grid preparation without support film. (a) Bare grid; (b) a droplet is deposited until it is dried; and (c) particles attached on the grid bars for TEM.

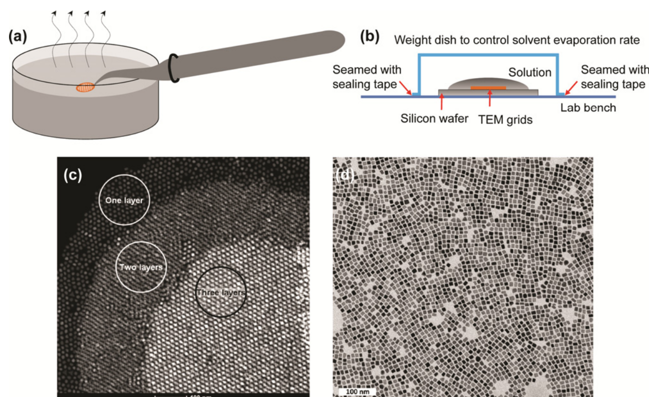

Fig. 2.3 Special TEM grid preparation. (a) A grid is immersed into the solution until the solution in the container is gradually dried; (b) a grid is placed on the top of a silicon wafer, and covered with solution drops. This setup was covered with a weight dish and seamed with a sealing tape to control the evaporation process; (c) STEM image of Pt_3Ni nanoparticles assembled in three layers prepared by method in (a); and (d) TEM image of Pt nanocubes prepared by method in (b).

Another TEM grid preparation example is shown in Fig. 2.3(b) [2]. A piece of 200-mesh film-supported grid was placed on the top of a (111) surface-polished square Si wafer with dimensions of 15 mm × 15 mm, and then the solution drops of Pt nanocubes were placed on the grid. Because of the considerable surface tension of the colloidal suspensions on the Si wafer, the bottom Si wafer was intentionally designed to constrain Pt nanoparticle suspensions without spreading out, while assemblies on the Cu grid were collected. In a typical sample preparation, 20 μL of the stock dispersion was drop cast onto the substrate, immediately covered with a weight dish (41 mm in length and 8 mm in height), and seamed with sealing tape. A TEM image of the self-assembled Pt nanocubes is shown in Fig. 2.3(d), where nanocubes in a monolayer are well assembled over large areas.

2.1.2 Ion Milling

If the sample is a bulk hard material, the preparation process is different to powders to preserve its microstructural integrities. A common method

is ion milling, which is a universal method workable to all solid samples, whether conductive or not. Its procedures are demonstrated in Fig. 2.4, including the following steps:

1. *Cutting.* Use a precision saw with a piece of abrasive wheel to cut the bulk sample into thin slices (Fig. 2.4a). The slice thickness can be controlled by the saw. If it is too thin, the slice may break or get distorted; while if too thick, more materials are consumed and it will take much effort to thin it in the following procedures. Normally 0.7 mm is an optimal thickness. Cutting fluids should be used to prevent the specimen from heating and lubricate the cutting tool, and cutting dressing should be used to remove fragments on the saw surface every few minutes. This cutting process is normally done in few minutes, and the operator should stay onsite until it is completed.
2. *Grinding and polishing.* In order to handle easily, the thin slice is bonded to a sample holder (Fig. 2.4b), such as a big Al stub, using crystal bond wax (it melts between 120 and 150 °C upon heating, so that it can bond the sample when it cools down). The wax dissolves in acetone solvent. Precaution should be taken during grinding to avoid the sample being worn away or peeled off from the bond. Grind the sample from coarse grits gradually to fine grits, then polish it. Both sides should be polished, and the backside that is not used for dimpling should be well polished. After polishing, the specimen thickness is expected thinner than 100 μm, and normally 60 μm is achievable.
3. *Drilling* to small disks, with diameter about 3 mm or little smaller, using an ultrasonic disk cutter (Fig. 2.4c). If the sample is ductile, like metals, use a sample puncher to get thin disks.

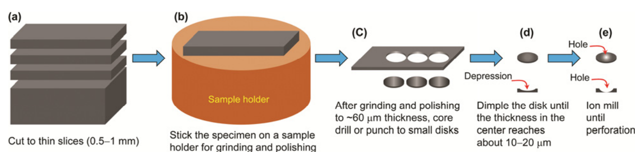

Fig. 2.4 Ion milling procedures. (a) Cutting; (b) a slice on a sample holder for grinding and polishing; (c) drilling to small disks; (d) dimpling; (e) ion milling.

4. *Dimpling.* Mount a piece of disk on a dimpler holder using crystal bond, and dimple its top surface to get a depression (Fig. 2.4d). To obtain a good TEM sample, this process is very critical, since it is a mechanical process to remove the material without artifacts on the final sample. The remaining thickness should be as thin as possible while not penetrated at this stage. If it is too thick, it will take long time for ion milling, which may enhance ion milling artifacts. Slightly further dimpling to thin the thickness, if possible, will significantly reduce the following ion milling time, while precautions should be taken to avoid holes or breakage of the specimen. Generally after the dimpling process, the remaining sample thickness should reach 10–20 μm. In addition, dimpling can be used to roughly select the perforation location.
5. *Ion milling.* If the sample is brittle, it may be fixed onto a metal washer (or ring) using epoxy resin. Ion milling can be done either on both sides or on a single side. Cooling will reduce the ion beam damage on the specimen. When a small hole appears, the milling should be terminated immediately.

The sample dimpling process is schematically shown in Fig. 2.5(a). The specimen mounted on the holder spins on the bottom, and the dimpling wheel also spins on the top surface of the specimen. A few drops of grinding slurry are applied, starting with a coarse grit (~5 μm) and ending with a fine grit (0.5 μm or smaller). Finally polish the surface using a polishing wheel. The depth of the depression can be estimated using the dimpler if available, or using the geometry as shown in Fig. 2.5(b). The wheel radius R can be measured, which is a constant. When a depression appears, measure its radius r, thus thickness t of removed material is

$$t = R - \sqrt{R^2 - r^2}\,. \tag{2.1}$$

The remaining thickness is therefore, $T{-}t$, where T is the original sample thickness. One may print a table showing the relationship between the thickness t for measured r. If the sample is silicon, use a strong light to illuminate the backside of the sample. If the dimpled area appears to

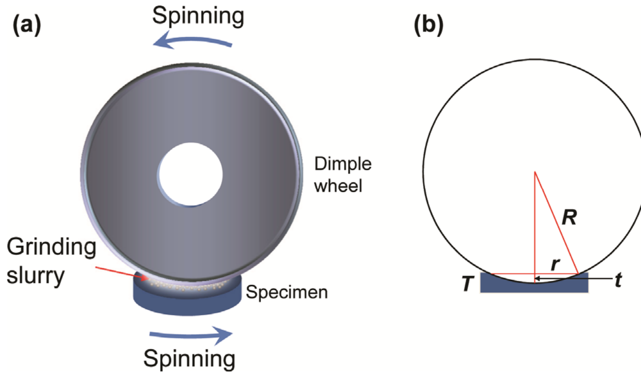

Fig. 2.5 (a) Dimpling process; (b) geometry.

be transparent with red, the remaining thickness is ~10 μm; if it appears as orange color, the thickness is even thinner, ~5 μm. At least red color should appear by the dimpling process.

Alternatively, the thickness of the dimpled sample can be inspected using a light microscope. First focus on the sample top surface, and then focus it on the bottom of the depression. The focus difference from the top to the bottom (or backward), which can be read on the microscope, is the thickness t of the removed material.

The ion milling equipment uses impinging incident Ar^+ ion beams to remove, or sputter, sample atoms away from the surface (Fig. 2.6a), so that the center area is gradually thinned during milling. Sputtering is a result of momentum transfer between the incident ions and the sample atoms on the surface. There are several factors controlling the ion milling process:

1. Ion mill voltage, which controls the average energy of incident ions;
2. Ion mill current, which controls the flux of ions;
3. Angle θ, which can be low angle (few degrees) or high angle (over 20°);
4. Specimen rotation, which controls the specimen rotation speed, or rocking so that the specimen only rotates back and forth in a certain angle range to avoid beam damage on certain locations, such as interface of two pieces of thin films.

The ion milling can be done using two guns to speed up, or just one gun to protect the other side. Higher voltage, flux, or angle θ produces faster milling rate, which causes large damage on the sample. Therefore, normally the samples are first milled at a higher voltage, flux, and angle θ before the perforation, while when the perforation is approached these parameters are decreased to reduce the ion mill damage. Roughly, the ion milling rate is around a few micrometers per hour. The instrument should be periodically maintained to ensure the ion beam shoots at the center of the specimen. Examples of $Nd_{0.5}Sr_{0.5}MnO_3$ [3] and Bi-based superconductor [4] samples prepared by the ion milling methods are shown in Fig. 2.6(b) and (c), respectively.

Solid thin film samples, as shown in Fig. 2.7(a), can be prepared by the ion milling method, along plane-view (Fig. 2.7) or cross-sectional view (Fig. 2.8) as follows.

1. *Plane-view sample preparation.* To prepare plane-view TEM sample, mount the sample on a sample holder with face down to protect the thin film side (Fig. 2.7b). After thinning the sample by grinding and polishing the substrate side only, drill small disks, with diameter of 3 mm (Fig. 2.7c). Again only dimple the substrate side to protect the thin film (Fig. 2.7d). Finally, ion mill the substrate side only until the perforation is done (Fig. 2.7e). If the thin film is relatively thick, ion mill the thin film side slightly as needed.

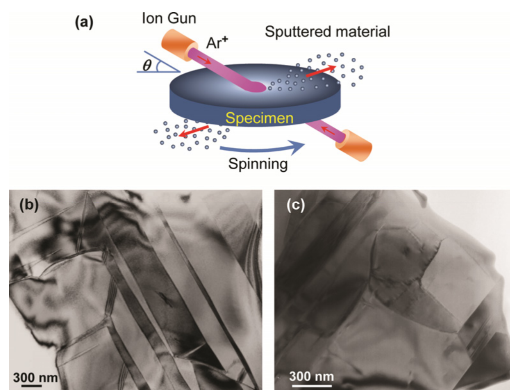

***Fig. 2.6** Ion milling process (a), and TEM images of $Nd_{0.5}Sr_{0.5}MnO_3$ (b) and Bi-based superconductor (c) prepared by ion milling.*

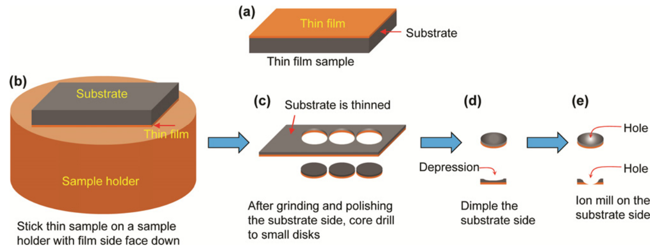

Fig. 2.7 Thin film plane-view preparation. (a) Thin film on a substrate; (b) the sample is mounted on a sample holder with film side down; (c) after grinding and polishing the substrate side, drill small disks; (d) dimpling the substrate side; (e) ion milling primarily on the substrate side only to protect the thin film.

2. *Cross-sectional view sample preparation.* To prepare cross-sectional view of the sample, bond two pieces of thin film samples face-to-face together using a strong epoxy resin (Fig. 2.8a), such as Torr Seal resin. Machine the sample into a circular cylinder shape (more practice and patience needed to do so), then insert it into a tube with an outer diameter of ≤3 mm, which is filled with the strong epoxy resin (Fig. 2.8b). At this time, bond this tube (filled with sample) on a glass slide with the epoxy for the next step of sectioning. When the epoxy cures, cut the tube into thin slices (Fig. 2.8c). Mount the sample on a holder and thin it by grinding, polishing, and dimpling (Fig. 2.8d). Dimpling should be done on the thin film area to control the final perforation location. Precautions should be taken to avoid breaking of the two pieces of boned samples, and attach with a piece of metal washer after dimpling if needed. Finally, ion mill the sample on both sides until perforation occurs on the thin films (Fig. 2.8e). If a hole appears on the substrate, continue the ion milling process until a hole appears on the thin film. Use a light microscope to check the sample to ensure there are sufficient thin areas in the thin film and thin film/substrate interface (Fig. 2.8f) and continue the ion milling process if needed. Fig. 2.9 shows an example of the cross-sectional thin film sample preparation using the method descripted in Fig. 2.8. Two pieces of thin films are face-to-face bonded by glue, and such a gap is large if viewed in TEM.

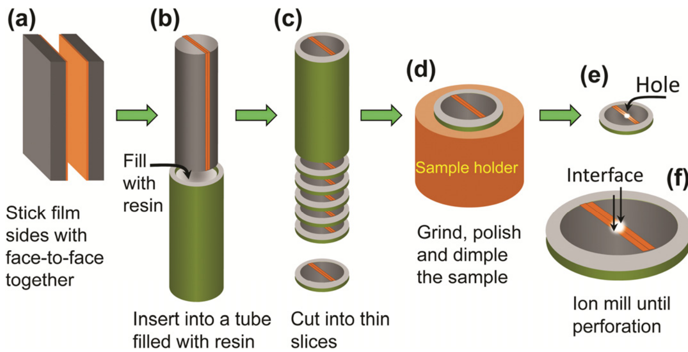

Fig. 2.8 Thin film cross-sectional view preparation. (a) Bond two pieces of thin film samples face-to-face together; (b) machine the sample into a circular cylinder shape, then insert it into a tube with an outer diameter of ≤3 mm, which is filled with resin; (c) cut it into thin slices; (d) thin the sample by grinding, polishing, and dimpling (ensure the thin film area is dimpled); (e) ion milling (ensure the perforation occurs on the thin films); (f) enlarged view of (e).

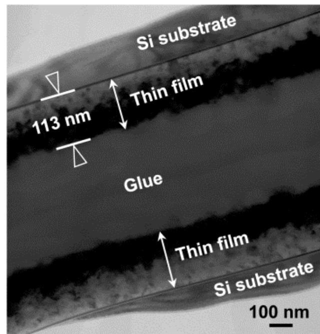

Fig. 2.9 Example of cross-sectional TEM sample of two pieces of thin films on Si, prepared using the method shown in Fig. 2.8.

2.1.3 Electropolishing

Although ion milling method can work on a wide variety of samples, the entire procedure takes a long time, and some samples may exhibit artifacts caused by ion milling, such as wave-shaped structure, or limited thin areas. Sometimes it is even possible to detect Ar from the ion milled samples. For conductively metallic materials, a more effective way to prepare good TEM samples with sufficient thin areas is electropolishing [5, 6].

The procedures for electropolishing are similar to ion milling method as demonstrated in Fig. 2.4, including cutting, grinding, polishing, and punching into 3-mm disks. Although the metals are normally ductile that do not break into smaller pieces, try to avoid deformations such as bending, which may introduce artifacts. The 3-mm disk sample is used for twin-jet electropolishing, as shown in Fig. 2.10(a). A pump runs to supply the electrolyte ejecting on both sides of the sample to thin it by chemical etching. The sample is connected to the anode of the power supply (positive part), and ensure the sample is in contact with electrode metal wires inside the sample holder. The electrolyte is an acid solution. Depending on the sample type, different compositions of electrolyte, voltage, and electrolyte temperature should be chosen. Fig. 2.10(b) shows the electrochemical process. Since the sample is connected to the anode of the battery, the metal dissolves into the solution to become M^{n+}, while the jet nozzle is connected to the cathode side, where H^+ in the acid solution gain electrons to reduce to H_2 and release in the atmosphere. When perforation occurs, the process should be immediately terminated, and the sample with the holder should be taken away from the acid solution as quickly as possible and it should be rinsed using the same pure solvent (such as pure ethanol or methanol) for several times until it is clean from the acid. Normally a light detector is used in the device for detecting the perforation. The electropolishing experiment, including electrolyte preparation, should be done in a fume hood, and the operator should wear lab coat, gloves, and safety goggles.

Table 2.3 lists 10 types of common recipes for twin-jet electropolishing. The electrolyte containing 5%–20% perchloric acid ($HClO_4$) in methanol or ethanol is a universal one, which works for most metals and alloys. However, one should be very careful while dealing with the perchloric acid since it is highly corrosive. Nitric acid (HNO_3) and sulfuric acid (H_2SO_4) are also commonly used and can be used for a variety of metals. Some electrolytes can be used only once and cannot be stored, like nitric acid in ethanol, which becomes explosive if it is stored in bottle.

Table 2.3 Common recipes for twin-jet electropolishing (all in volume percent).

No.	Electrolyte	Conditions	Sample	Comments
1	5%–20% perchloric acid in methanol	Low temperature to room temperature, 10–30 V	Al and its alloys; Be and its alloys; Fe and steels; Ni and its alloys; Ti and Ti alloys; Zr and Zr alloys	20%–30% butoxyethanol or glycerol may be added.
2	5%–20% perchloric acid in ethanol	Low temperature to room temperature, 10–30 V	Al–Cu–Ti; stainless steel	
3	10%–20% perchloric acid in acetic acid	Low temperature to room temperature, 20–80 V	Co and Co alloys; Fe and Fe–Ni–Cr alloy; Ni–Cr; Ni–V	
4	10%–33% nitric acid in methanol	–30 to –10 °C, 10–20 V	Al and its alloys; Cd; Cu and its alloys; Fe and alloys	
5	30% nitric acid in ethanol	–10 °C, 10–20 V	Mg and its alloys	This electrolyte may become explosive if stored in a bottle
6	5%–20% sulfuric acid in methanol	–40 to 5 °C	Al–Cu; Be–Ti; Mo and its alloys; Ti and Ti alloys; Zr and Zr alloys	
7	6% sulfuric acids and 1% hydrofluoric acid in methanol	–40 °C, 40 V	Nb and its alloys	Hydrofluoric acid dissolves glass parts of the device!
8	6% hydrochloric and 6% sulfuric acids in H_2O	25 °C, 10 V	Al–Fe	
9	25% phosphoric acid and 25% ethanol in H_2O	Room temperature, 8–10 V	Cu and its alloys	
10	13% saturated solution of ammonium fluoride in methanol	–30 °C, 150 V	Nb and its alloys	

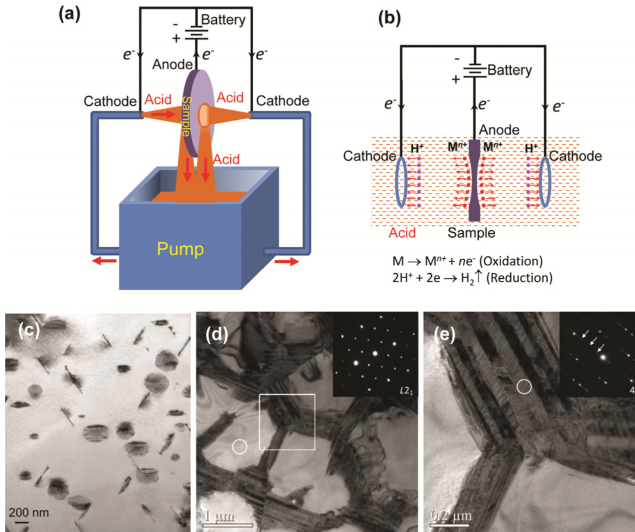

***Fig. 2.10** (a) Schematical twin-jet electropolishing device; (b) electrochemical process; (c) NiTi alloy; (d, e) Ni–Mn–Sn–Co alloy.*

To prepare the electrolyte solutions, it is very important to cool the solvent first, and then slowly pour the acid to the solvent. An opposite way to pour the solvent into the acid may cause hazardous explosion! Normally the electrolyte should be cooled, either by the cooling system of the device or by manually pouring a small amount of liquid nitrogen into the solution slowly. The voltage and flow rate can be controlled by the device, while the current is an indication whether electropolishing is occurring or not. If no current is shown (0 A), the circuit is not closed and thus the sample is not thinned. If this happens, check the sample holder to ensure the sample touches the metal wires.

When all samples are done, it is important to rinse the entire device thoroughly and pump it with clean water. All acid solutions should be stored for the next use or properly disposed. If the sample is quickly corroded in air, store it in dried desiccator, vacuum desiccator, or even pure ethanol in a small bottle.

Fig. 2.10(c) shows an example of NiTi alloy prepared by using a solution of 20 vol.% H_2SO_4 in a methanol solution at ~0 °C temperature [7]. Uniform thickness in this view area was obtained, and four variants of Ni_4Ti_3 precipitates are evident. In Fig. 2.10(d), the Ni–Mn–Sn–Co

alloy was prepared using a solution of 5 vol.% perchloric acid and 95 vol.% alcohol at a voltage of 30 V at a low temperature of –33 °C [8]. Large thin area was obtained. The grains are $L2_1$ austenite. An enlargement from the framed area in Fig. 2.10(d) is shown in Fig. 2.10(e) for details of martensite plates, as confirmed by electron diffraction pattern inserted.

2.1.4 Focused Ion Beam

FIB instrument resembles a scanning electron microscope (SEM), while instead of using electron illumination, Ga^+ ions are used. It demonstrates versatility for imaging, ion-induced deposition, gas-assisted etching, implantation, and milling. The FIB operated at a low beam current is used for imaging using collected sputtered secondary ions or secondary electrons, while at a high beam current, for site-specific sputtering or milling. This cutting manner using energetic Ga^+ ions is similar to the ion milling using Ar^+ ions, while the ion beam of FIB is well focused and can move with controls. Either conductive or nonconductive samples can be milled with FIB. If the sample is nonconductive, a low-energy electron flood gun is used to provide charge neutralization, and highly insulated samples can be imaged and milled even without a conducting surface coating.

FIB can be used to prepare TEM samples, with the capability to select specific sites to get thin sections. A lift-out method is currently widely used. An example is shown in Fig. 2.11. Major steps are listed as follows:

1. Select a specific site of the sample and deposit 1-μm-thick strip of platinum (Pt) by electrodeposition to protect the area from being contaminated by Ga^+ ions in the following process (Fig. 2.11a).
2. Select a cutting area on both sides of the Pt strip, as shown by dotted lines in Fig. 2.11(a), and remove the materials in these areas to get two trenches, as shown in Fig. 2.11(b).
3. Further thin the sample near the Pt strip and enlarge the two trenches, as shown in Fig. 2.11(c). Tilt the specimen to an inclined position to cut into gaps along the indicated lines to form a frame (Fig. 2.11c).

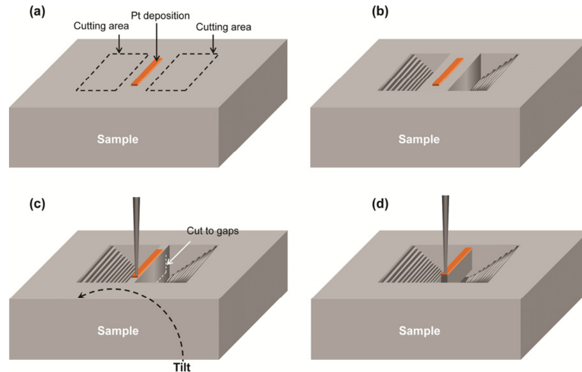

Fig. 2.11 FIB preparation of bulk sample. (a) Deposition of a Pt strip and selecting areas for removal; (b) two trenches after milling; (c) further thinning to near the Pt strip thickness, rotating the sample to cut gaps (indicated), and attaching to of a probe; (d) removing the sample to free the piece.

4. Use a probe to attach the sample piece at the Pt area. The deposited Pt binds the tip tightly (Fig. 2.11c). Then cut off the remaining material so that it is separated from the bulk sample (Fig. 2.11d).
5. Lift out the sample from the trench. Align the piece vertically and further thin it on both sides. When it is thin enough, move and deposit it onto a TEM grid.

An example of the FIB preparation of Ni–Mn–Sn ribbon sample is shown in Fig. 2.12 [9]. The procedures are shown in Fig. 2.12(a–f) in sequence. When this sample was installed in TEM, it showed large thin area, as shown in an STEM image take at a low magnification to show the entire FIB sample in Fig. 2.12(g). Martensite plates are clearly revealed. A magnified TEM is shown in Fig. 2.11(h), exhibiting high density of martensite twins.

2.1.5 Microtomy

Although ion milling and FIB are universal sample preparation methods with versatilities, for polymers or polymer-based composites, a more effective way to prepare TEM thin sections is microtomy, that is, to use an ultramicrotome to directly cut the sample into thin sections that are thin enough for imaging in TEM.

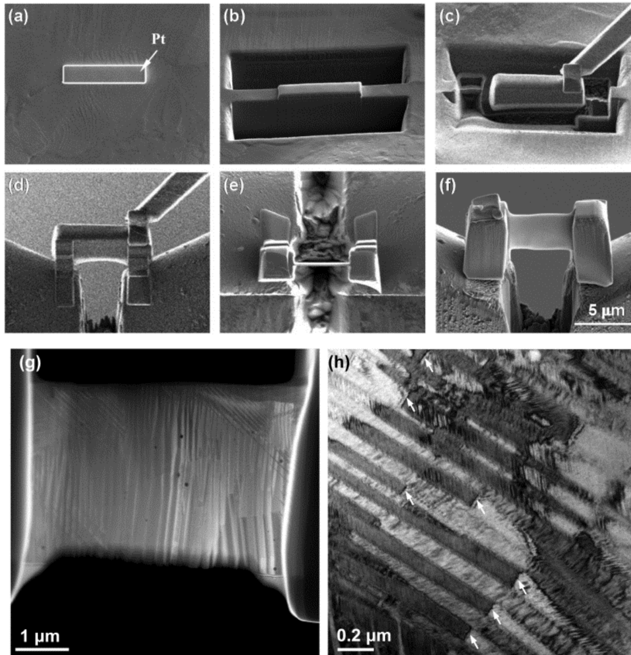

Fig. 2.12 Preparation steps of a thin foil from a Ni–Mn–Sn ribbon using FIB. (a) Depositing Pt to protect the interested area; (b) cutting to get two side trenches; (c) attaching a micromanipulator to the sample and free the sample to lift out; (d) lifting out the sample; (e) further thinning and cleaning of the sample; (f) final thin foil; (g) STEM image of the sample at a lower magnification to show the entire TEM sample prepared by FIB; (h) enlarged TEM image of the prepared sample.

Fig. 2.13 illustrates the microtomy process. A diamond knife is attached to a trough, which is filled with deionized (DI) water (Fig. 2.13a). If a homemade glass knife is used, then the knife is attached to a separate trough filled with water. On the microtome instrument, the knife is at the fixed position, whereas the sample moves up and down, and also forth and back to produce thin sections. The procedure details are shown in Fig. 2.13(b–e). Staring from the position in Fig. 2.13(b), the block moves forward (the thickness of the thin section), so that it reaches above the blade (Fig. 2.13c). It moves down so that a section is made, and the section is floated on the water surface (Fig. 2.13d). Then the block moves backward to reach the position in Fig. 2.13(e). When it moves up, it reaches the position in Fig. 2.13(b) for the next cycle.

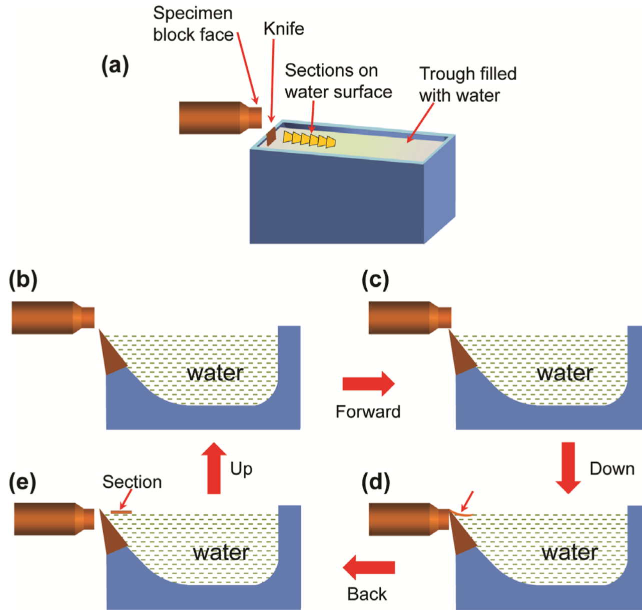

Fig. 2.13 Microtomy process. (a) Setup; (b–e) different block positions during a cycle.

The microtomy is done in the following procedures:

1. *Embedding.* If the sample is too small to make a specimen block face for sectioning, embed it into epoxy resin first (if it is large enough, just stick it on to an epoxy holder or use it directly). The embedding medium should be strong enough, and some vendors can provide such embedding kits for material samples. Some polymeric samples need staining at this stage. Use a razor blade to trim the sample to make a block face and ensure the sample face is exposed from the embedding medium. Use newly prepared fresh stains to stain the sample with sufficient time. Such staining in fact also hardens the sample so that it becomes easier to get thin sections.
2. *Trimming.* Mount the sample on the microtome. Use a razor blade to trim the block face first, and then use a glass knife to smooth the surface. Normally a trapezoid (or rectangular) shape block face is made.

3. *Sectioning.* Using a diamond knife to cut enough number of thin sections that are floated on the water surface (Fig. 2.13a). The cutting angle (clearance angle) is normally 5–6°, which is indicated on the diamond knife. The section thickness can be estimated by interference color of the sections floating on the water surface, as listed in Table 2.4. Silver color sections have the optimum thickness of 60–90 nm for imaging at a lower voltage (120 kV), whereas gold color sections can be imaged at a higher voltage of 200 kV, in case a higher resolution is required.
4. *Collecting.* Clean several bare grids or film-coated grids (formvar or formva/carbon film). Use a pair of tweezers to hold a piece of grid to pick up the thin sections from top side parallel to the water surface, bottom side underneath the sections, or halfway down the water. The dull side of the bare grid, or film side of coated grid, should attach the specimen sections. Place the grid on a piece of filter paper with sections on the upside, and dry in air. Some sections may need staining, and if they are nonconductive, a thin carbon layer (~10 nm) should be coated.

When the experiment is completed, clean the diamond knife properly. Never touch the knife blade with anything besides a cleaning swab provided by the vendor as a specific diamond cleaning kit. Never use acetone to clean the knife, since the knife embedding resin dissolves in acetone!

Some TEM thin section examples are shown in Fig. 2.14. In Fig. 2.14(a), the polymer sample contains few large polyhedral oligomeric silsesquioxane (POSS) particles, and the image is taken at a low magnification, so the hexagonal grid bars are shown up. Some particles remain

Table 2.4 Interference color and thickness of thin section.

Interference color	Thin section thickness (nm)
Gray	<60
Silver	60–90
Gold	90–150
Purple	150–190
Blue	190–240
Green	240–280
Yellow	280–320

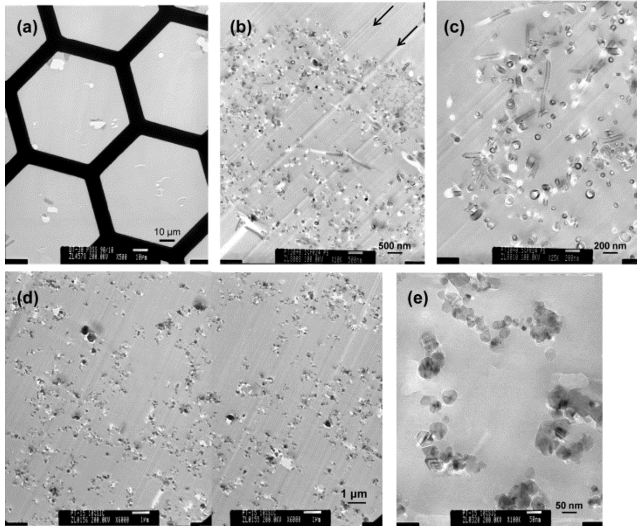

***Fig. 2.14** (a) A thin section at a low magnification showing grid bars; (b, c) TEM images of CNF/polymer nanocomposite; (d, e) TEM images of SiC/polymer composite.*

in the polymer matrix, whereas some particles are peeled off during the section, leaving broken holes. Fig. 2.14(b) shows a TEM image of carbon nanofiber (CNF)/polymer nanocomposite at a lower magnification [10], where parallel markers, as indicated by arrows, are artifacts produced by the knife during sectioning. At a higher magnification in Fig. 2.14(c), most of the CNFs are sectioned as circles along their cross sections. Fig. 2.14(d) shows a wide area composed of two TEM images from a SiC/polymer sample. Overall the SiC particles are well dispersed in the polymer matrix. At a higher magnification in Fig. 2.14(e), it is found that few SiC particles are peeled off during the sectioning.

Fig. 2.15 shows thin sections of carbon fibers. For cross-sectional views, carbon fibers are embedded perpendicular to the block face, as shown in Fig. 2.15(a). The diameter of the fiber is very large and after sectioning, small fragments are yielded. Therefore, the sections are collected using a grid with holey mesh support film, as shown in Fig. 2.15(b) for a cross section of a carbon fiber. An enlarged image in Fig. 2.15(c) is taken from the framed area in Fig. 2.15(b). From such a cross section, it is possible to identify the structural difference between core and shell areas [11, 12]. However, if the carbon fibers are prepared

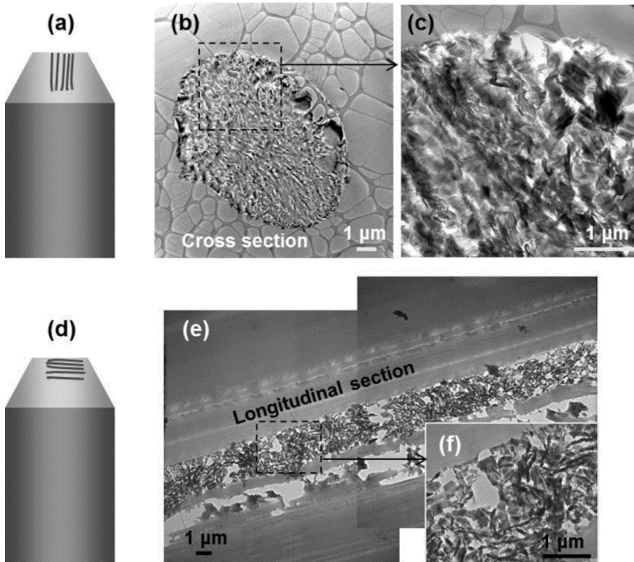

Fig. 2.15 Carbon fibers. Embedding carbon fibers in (a) is for cross-sectional views (b, c), and embedding in (d) is for longitudinal section (e, f).

by crushing into powders, such as the image in Fig. 2.1(h), it is impossible to recognize whether the particle is from the core or shell areas. When the carbon fibers are embedded parallel to the block face (Fig. 2.15d), longitudinal sections are made, as shown in Fig. 2.15(e), with an enlargement from its framed area shown in Fig. 2.15(f). Therefore, through the embedding and microtomy methods, information from both cross and longitudinal sections can be obtained.

2.2 Biological Samples

Unlike the material samples that are dried and condensed, most biological samples are aqueous or hydrated containing large portions of water [13]. They are soft, composed of light elements such as H, C, N, O, S, and P, and they are not electrically nonconductive. Therefore, biological sample preparations involve multiple steps to get TEM samples. Biological samples typically include particulate samples, and cells and tissue samples.

2.2.1 Particulate Samples

If the sample is a liquid solution containing particulates or fibers, it can be prepared by negative staining at room temperature [14], or plunge freezing at a cryogenic temperature, which will be presented in Volume 2 for details.

The negative staining process is shown in Fig. 2.16. Normally without any stains, a particle is imaged as a dark image in TEM, as shown in Fig. 2.16(a), since the particle scatters and absorbs the incident electrons (scattering absorption contrast). However, the hydrated samples cannot be directly inserted to the TEM for imaging. Negative staining is required to apply chemicals containing heavy metals to cover or partially cover the particles, depending on the properties of the sample, support film, and the stain, as shown in Fig. 2.16(b–e). In either case, after the sample is dried for imaging, in the TEM projection, the particle sample area exhibits lighter contrast since its surrounding areas contain thicker stains. Therefore, this particle exhibits a reversed contrast compared with its regular image, as shown in Fig. 2.16(f).

Negative staining can be done in the following methods.

1. Prepare staining solution.
2. Glow discharge a TEM grid with support film to increase its hydrophilicity.
3. Use a pair of self-closed tweezers to hold the grid, and place 1–3 μL sample solution on the grid. Use a piece of filter paper to wick away extra sample liquid.
4. After ~10 s, slowly pipette on 20 μL stain (uranyl acetate, phosphotungstic acid, sodium silicotungstate). While pipetting onto the grid, gently absorb stain on the opposite side using a filter paper sliver. Wick away extra liquid on the grid.
5. Dry the grid in air.

One may place a drop (~100 mL) of the staining solution onto a parafilm surface, and in the above step 4, flip the TEM grid upside down and let it float on the top surface of the staining solution for 20 s, and then take it away from the staining solution and dry it in air.

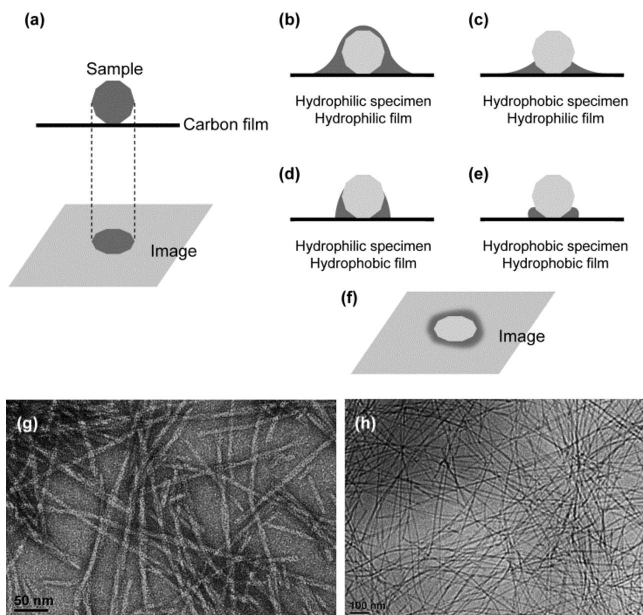

***Fig. 2.16** Negative staining. (a) Without stains, a particle would be imaged as a dark image in TEM; (b–e) different forms of negative staining depending on the property of stains with the specimen and support film; (f) TEM image of the sample by negative staining, where the particle is imaged as reversed contrast compared with (a); (g) TEM image of peptide nanofibers, which appear as bright contrast; (h) TEM image of peptide nanofibers prepared by plunge freezing, so that they are frozen in ice and thus directly imaged to show dark contrast.*

Another way for negative staining is to mix the sample solution and the stain in 1:1 ratio, and then apply the mixed solution to the grid.

Samples can also be positively stained so that the stain forms a complex with the specimen, and thus the particles exhibit dark contrast in TEM. In such a way, a positive stain will impart increased electron opacity to the specimen creating a darker specimen, whereas a negatively stained specimen remains more electron translucent relative to the surrounding stain. Negative staining has been routinely used in laboratory practices.

An example of hydrogel-forming peptide prepared by negative staining using staining solution of 2 wt.% uranyl acetate in water [15] is shown

in the TEM image in Fig. 2.16(g). The nanofibers exhibit brighter contrast over the surrounding areas. For comparison, Fig. 2.16(h) shows the nanofibers prepared by plunge freezing and imaged in the TEM at a low temperature. These fibers are embedded in ice without any other chemicals involved, so they exhibit darker contrast.

2.2.2 Cells and Tissue Samples

Biological cells and tissue samples contain large amount of water. In order to view the sample in TEM with high vacuum, the sample fixation is one of the most important and most critical steps. Upon appropriate fixation, the ultrastructure of the cells or tissues can remain as close to the living sample as possible. The samples can be prepared at room temperature as a classical preparation using chemical fixation, or at low temperature as a cryopreparation using cryofixation. Multiple steps are involved to prepare them for TEM, as shown in Fig. 2.17.

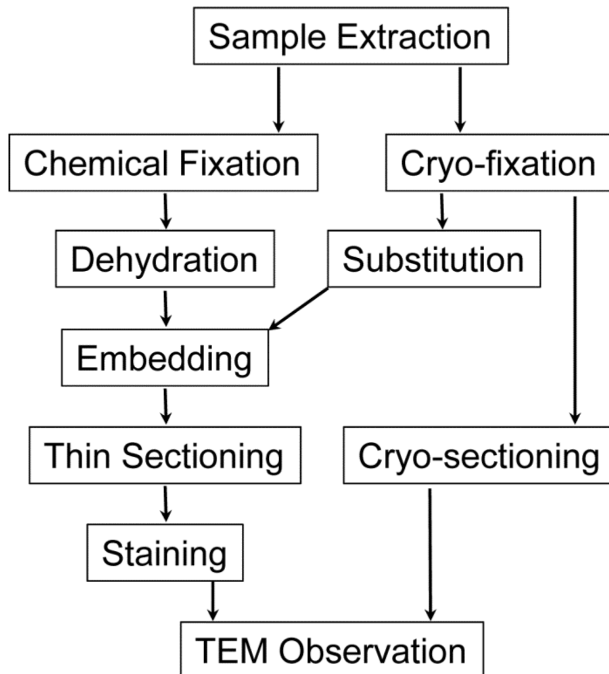

Fig. 2.17 Main pathways of biological sample preparation.

The classical room temperature preparation involves the following procedures [16]:

1. *Sample extraction.* Use a knife to extract a piece of representative sample with small size (approximately in centimeters), as shown in Fig. 2.18(a).
2. *Fixation.* It includes the following steps:
   a. Pre-fixation (fixes proteins) using 2.5% glutaraldehyde in phosphate buffer. Place a piece of extracted tissue on a slide, and dip glutaraldehyde solution on the sample (Fig. 2.18a). Use two pieces of razor blades to cut the sample with less deformation (Fig. 2.18b). Use a pair of tweezers to transfer the sample to a glass bottle filled with glutaraldehyde solution (Fig. 2.18c).
   b. Washing the samples in phosphate buffer for two to three times.
   c. Post-fixation (fixes lipids) using 1%–2% OsO_4 in phosphate buffer.
   d. Washing in phosphate buffer.

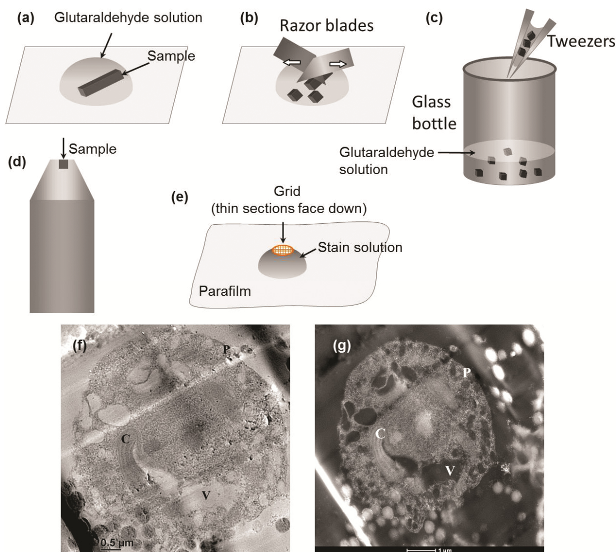

***Fig. 2.18** Sample preparation of cells and tissues (after [16]). (a–c) Pre-fixation and cutting into smaller pieces; (d) embedding into epoxy; (e) post-staining with uranyl acetate and lead citrate; (f) TEM and (g) STEM image of a single O. danica cell. The letter "P" represents the plasma membrane of the cell, "V" means vacuole, and "C" is chloroplast.*

3. *Dehydration.* The sample is dehydrated through an acetone or ethanol series following these steps: 50% ethanol (10 min) → 70% ethanol (10 min) → 80% ethanol (10 min) → 90% ethanol (10 min) → 95% ethanol (10 min) → 100% ethanol (20 min) → 100% ethanol (20 min).
4. *Substitution.* Use only propylene oxide (PO) and change liquid two to three times (each time 20 min).
5. *Embedding.* Use freshly mixed resin to embed the sample (Fig. 2.18d). The specimen is placed in a well of a silicone embedding plate, and resin is poured over the tissue. Ensure no air bubbles are trapped within the resin. The resin is polymerized at appropriate conditions for the specific resin used.
6. *Thin sectioning.* Refer to Section 2.1.5.
7. *Staining.* The post-staining with salts of heavy metals (uranyl acetate and lead citrate solutions) can enhance the contrast. Place a droplet of uranyl acetate solution on parafilm, and float the grid on the droplet with thin section down to react with the stain for 10 min (Fig. 2.18e). Wash with water very gently. Stain the grid on a droplet of lead citrate solution for 10 min, and then wash with water very gently and dry in air.
8. *TEM observation.* Biological samples are normally observed at relatively lower voltages (80–120 kV) to enhance the contrast, while in most cases high resolution is not required for the biological samples, so a lower voltage can be used.

An example of a single *Ochromonas danica* cell is shown in the images of TEM (Fig. 2.18f) and STEM (Fig. 2.18g) [17]. Briefly, the liquid algal samples were first mixed with Trump's Fixative and then filtered through a 0.45-μm-size plastic filter, so that the cells stayed on the surface of the filter. The cells were then stained in 1% (mg/mL, weight-to-volume ratio) osmium tetroxide (OsO_4 in the solution of 0.1 M 4-(2-hydroxyethyl)-1-piperazineethanesulfonic acid buffer with pH 7.4) for about 0.5 h, and dehydrated through methanol (10%–100%). Afterwards, they were embedded into epoxy resin and sectioned at 100 nm thickness to be analyzed by TEM and STEM. The cells are found attaching on the filter paper found at lower magnifications.

References

[1] J. Zhang, Z. Luo, Z. Quan, Y. Wang, A. Kumbhar, D.-M. Smilgies, J. Fang. Low packing density self-assembled superstructure of octahedral Pt_3Ni nanocrystals. *Nano Lett.* **11**, 2912–2918 (2011).

[2] Z. Quan, H. Xu, C. Wang, X. Wen, Y. Wang, J. Zhu, R. Li, C.J. Sheehan, Z. Wang, D.-M. Smilgies, Z. Luo, J. Fang. Solvent-mediated self-assembly of nanocube superlattices. *J. Am. Chem. Soc.* **136**, 1352–1359 (2014).

[3] Z.P. Luo, D.J. Miller, J.F. Mitchell. Structure and charge ordering behavior of the colossal magnetoresistive manganite $Nd_{0.5}Sr_{0.5}MnO_3$. *J. Appl. Phys.* **105**, 07D528 (2009) (3 pp).

[4] V.A. Maroni, N.N. Murphy, M. Mika, Z.P. Luo, Y. Tang, H. Claus, D.J. Miller, J.-H. Park, S.E. Dorris, G.N. (Bart) Riley, Jr., S. Fleshler, R. K. Williams. Search for a silver-sheathed 1212-type superconductor with a grain colony microstructure: $M_1Sr_2Y_{1-x}Ca_xCu_2O_z$ with M=(Bi, Pb), (Cd,Pb), and (Fe,Pb). *IEEE Trans. Appl. Supercond.* **13**, 7–16 (2003).

[5] J.W. Edington. *Practical Electron Microscopy in Materials Science*. Techbooks, Herndon, Virginia, 1991.

[6] P.J. Goodhew. *Thin Foil Preparation for Electron Microscopy*. Elsevier, Amsterdam, 1985.

[7] I. Karaman, A.V. Kulkarni, Z.P. Luo. Transformation behaviour and unusual twinning in a NiTi shape memory alloy ausformed using equal channel angular extrusion. *Philos. Mag.* **85**, 1729–1745 (2005).

[8] H. Zheng, W. Wang, J. Yu, Q. Zhai, Z. Luo. Martensitic transformation in melt-spun Heusler Ni–Mn–Sn–Co ribbons. *J. Mater. Res.* **29**, 880–886 (2014).

[9] W. Wang, J. Yu, Q. Zhai, Z. Luo, H. Zheng. Origin of retarded martensitic transformation in Heusler Ni–Mn–Sn melt-spun ribbons. *Intermetallics* **42**, 126–129 (2013).

[10] Z.P. Luo, J.H. Koo. Quantifying the dispersion of mixture microstructures. *J. Microsc.* **225**, 118–125 (2007).

[11] D.D.L. Chung. *Carbon Fiber Composites*. Butterworth-Heinemann, Boston, 1994.

[12] Z.P. Luo, J. Sue, O. Ochoa, A. Holzenburg. Cross-sectional examination of crystallinity of carbon fibers by transmission electron microscopy. *Microsc. Microanal.* **8** (Suppl. 2), 1254–1255 (2002).

[13] J.J. Bozzola, L.D. Russell. *Electron Microscopy: Principles and Techniques for Biologists*. Jones and Bartlett Learning, Massachusetts, 1999.

[14] M.A. Hayat, S.E. Miller. *Negative Staining*. McGraw-Hill, New York, 1990.

[15] H. Huang, A.I. Herrera, Z. Luo, O. Prakash, X.S. Sun. Structural transformation and physical properties of a hydrogel-forming peptide studied by NMR, transmission electron microscopy, and dynamic rheometer. *Biophys. J.* **103**, 979–988 (2012).

[16] JEOL. *Preparation of Biological Specimens for Electron Microscopy*. JEOL, Tokyo, Japan.

[17] A.-J. Miao, Z. Luo, C.-S. Chen, W.-C. Chin, P.H. Santschi, A. Quigg. Intracellular uptake: A possible mechanism for silver engineered nanoparticle toxicity to a freshwater alga *Ochromonas danica*. *PLoS ONE* **5**, e15196 (2010) (8 pp).

CHAPTER 3

Instrumentation and Operation

There are several major manufacturers of transmission electron microscopes (TEMs), alphabetically, FEI (merged with Philips Electron Optics), Hitachi, JEOL, and Zeiss. The appearance and construction of TEMs produced by these manufacturers are different, even for different models by the same manufacturer. However, the basic design and working principles are similar. Note that some parts or apparatus, such as specimen holder, charge-coupled device (CCD) camera, X-ray energy-dispersive spectrometer (EDS), or electron energy-loss spectrometer (EELS), are provided by other parties.

This chapter provides an outline of the basic construction of a TEM, and general operation procedures regarding the alignments.

3.1 Construction

A TEM may appear differently. Representative parts are schematically shown in Fig. 3.1. It is important to know how do these parts work and how to operate them correctly. We separate the TEM into the following sections.

3.1.1 Electron Gun

An electron gun provides the electron illumination source. There are two types of electron gun: thermionic gun and field-emission gun (FEG).

The construction of a thermionic gun is schematically shown in Fig. 3.2(a), and its current emission during heating is shown in Fig. 3.2(b). A filament is installed inside a Wehnelt cylinder. The filament can be a

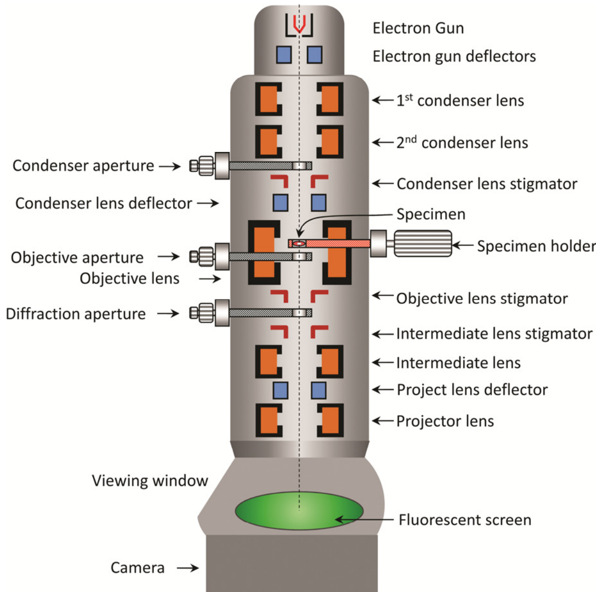

Fig. 3.1 Schematic construction of a TEM.

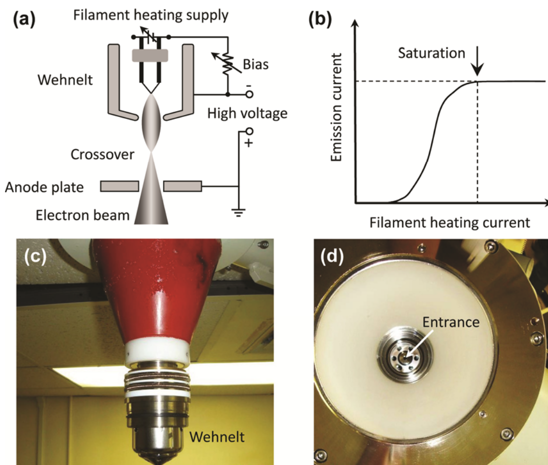

Fig. 3.2 (a) Construction of a thermionic electron gun; (b) emission current vs. filament heating current; (c) side view of the gun Wehnelt assembly; (d) top view of the TEM column that connects to the gun.

tungsten (W) filament, LaB_6 or CeB_6 (less commonly used than LaB_6) crystals. The filament is heated by a filament heating supply to a high temperature at 2,700 K for W, or 1,700 K for LaB_6 filament. A small

bias voltage (few hundred volts) is applied to extract the electrons out of the Wehnelt, and these electrons are accelerated by a high voltage (the TEM working voltage) between the Wehnelt and anode plate. A crossover is formed in this gap. A LaB_6 filament can provide about 10 times brighter beam than a W filament with several times extended lifetime, while a higher gun vacuum level is required. The LaB_6 filament can also provide improved coherency and reduced energy spread than the W filament. An appearance of the LaB_6 filament Wehnelt assembly is shown in Fig. 3.2(c), and a top view of the column that connects to the gun is shown in Fig. 3.2(d). It is seen that the hole for the electron passing through the column is very small.

For the thermionic gun, as shown in Fig. 3.2(b), the emission current increases with the filament heating current applied. However, once saturation is achieved, the brightness does not increase further even at a higher filament heating current. It is very important to notice that with increasing the filament heating current, the filament lifetime is significantly reduced. Therefore, in practice, the following general procedures should be obeyed:

1. Heat up the filament from cold very slowly until a stopper position is reached (in 5 min for W, and 20 min for LaB_6). If the filament is just turned off (the filament is still hot), it can be faster to turn it back to the final position.
2. From the filament image, make sure the filament is slightly undersaturated rather than oversaturated, to improve the filament lifetime. This slightly undersaturated condition determines the dial stopper position.
3. Also, turn off the beam slowly (in 1 min for W, and 2 min for LaB_6).

On an instrument with W filament, the specimen exchange can be done with the filament on, whereas on an instrument with LaB_6 filament, the filament is normally automatically turned off to protect the filament in case the vacuum breaks. Therefore, the filament should be turned off slowly, rather than suddenly as a protection, before the specimen exchange.

Depending on the emitter, there are two types of FEGs: (1) Schottky-type FEG, or hot FEG, using a ZrO_2 or W emitter working at a high temperature (1,600–1,800 K); and (2) cold FEG, using a very sharp W tip, working at a lower temperature (300 K) [1, 2]. The construction of an FEG is schematically shown in Fig. 3.3. There are two anodes. The first anode provides an extraction voltage (several thousands) to pull out the electrons from the gun tip, and the second anode provides a high voltage (the TEM working voltage) to accelerate these electrons. Compared with a thermionic gun, the FEG can provide ~100 times higher brightness than LaB_6, smaller beam spot size, higher coherency, and reduced energy spread, while a much higher vacuum level is required. In a normal condition, the FEG constantly stays on even when the microscope is not in use, unless for maintenance reason it is turned off. The filament on and off is normally done with computer controls, and thus such operations are straightforward. An FEG tip can be used for 1–2 years. It is very important to close the gun chamber when the beam is not in use. A comparison of different types of electron guns is given in Table 3.1.

The electrons travel in the microscope at very high speeds. Considering the relativistic effects, the electron wavelength λ is expressed as

$$\lambda = \frac{h}{\sqrt{2m_0 eV(1 + \frac{eV}{2m_0 c^2})}} \tag{3.1}$$

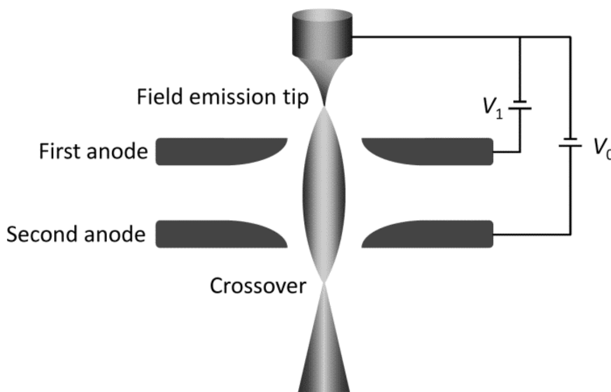

Fig. 3.3 Construction of FEG. V_1 is the extraction voltage, and V_0 is the acceleration voltage.

Table 3.1 Comparison of electron guns.

	Thermionic gun		FEG	
	W	LaB_6	Hot FEG	Cold FEG
Brightness (A/m^2Sr)	5×10^5	5×10^6	5×10^8	5×10^8
Crossover size (μm)	50	10	0.01–1	0.01–1
Energy spread (eV)	2.3	1.5	0.6–0.8	0.3–0.5
Vacuum (Pa)	10^{-3}	10^{-5}	10^{-7}	10^{-8}
Temperature (K)	2,700	1,700	1,600–1,800	300
Lifetime	30–100 h	500–1,000 h	1–2 yr	1–2 yr

Table 3.2 Electron wavelength.

Accelerating voltage (kV)	Wavelength (nm)
60	0.00487
80	0.00418
100	0.00370
120	0.00335
140	0.00307
160	0.00285
180	0.00267
200	0.00251
300	0.00197
400	0.00164
800	0.00103
1,000	0.00087

where h is Planck's constant (6.626×10^{-34} N·m·s), m_0 is the rest mass of electron (9.109×10^{-34} kg), e is the charge of electron (-1.602×10^{-19} C), V is the acceleration voltage (V), and c is the speed of light in vacuum (2.998×10^8 m/s). Table 3.2 lists the wavelength at different accelerating voltages (kV).

3.1.2 Electromagnetic Lens

The electromagnetic lenses are used to change the trajectories of electrons to focus the beam. They can magnify or demagnify the image.

A construction of the electromagnetic lens is shown in Fig. 3.4(a). Its pole pieces are made of soft iron materials, that is, soft magnetic materials with low hysteresis that do not retain magnetization when the applied magnetic field is turned off. Inside the iron shell wrapped with Cu coils, magnetic fields are generated by the coil when current passes

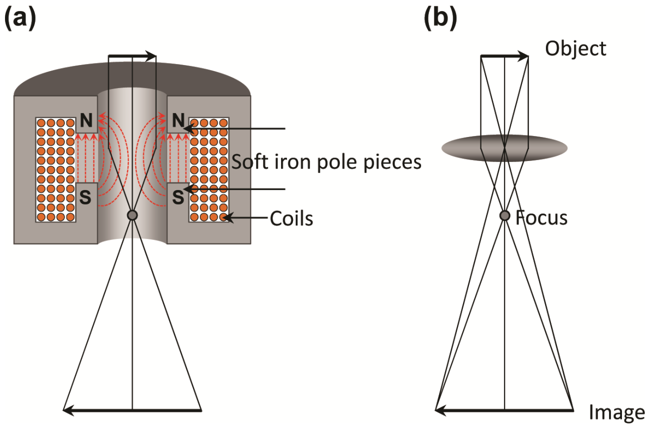

Fig. 3.4 (a) Electromagnetic lens; (b) optical lens.

through. Therefore, the charged electrons change their trajectories when they move through this magnetic field, so that it is possible to focus the electrons using the electromagnetic lens. An optical lens, which focuses lights, is shown in Fig. 3.4(b) for comparison.

In optics, for a given thin lens in air, the relationship between object distance u, image distance v, and focal length f is expressed as

$$\frac{1}{f}=\frac{1}{u}+\frac{1}{v} \tag{3.2}$$

The magnification M is thus

$$M=\frac{v}{u} \tag{3.3}$$

The optical lens has fixed f, so the image is focused by changing to the object distance u to meet Eq. 3.2 (suppose v is fixed), like a light microscope (LM). While in the case of TEM, the object is at a position with limited moving range (up or down slightly), while the focal length f can be changed largely to control the magnification and image position v. The focal length f in Fig. 3.5(b) is slightly shortened compared with Fig. 3.5(a), which changes the image magnification.

The lens focal length f is controlled by the lens current, which changes the magnetic field in Fig. 3.4(a). If the lens current is decreased

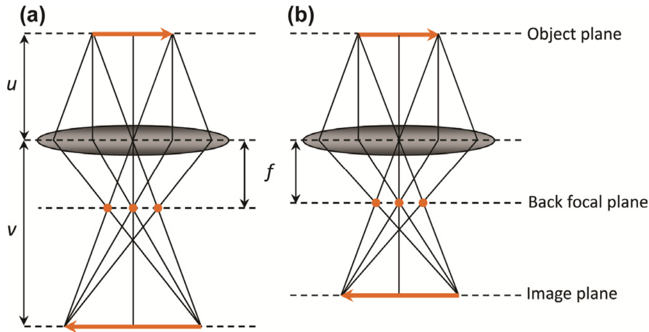

Fig. 3.5 Relationship between object distance u, image distance v and focal length f. (a, b) u remains the same, while f is changed.

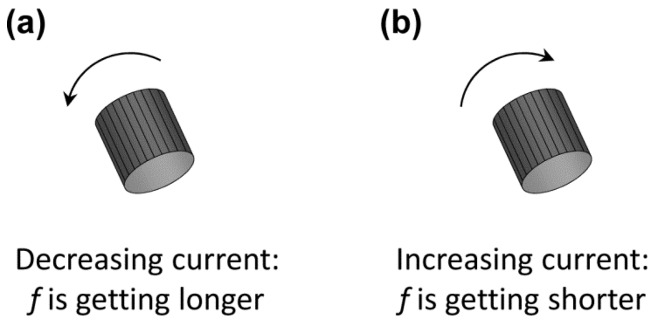

Fig. 3.6 Adjusting focal length f by changing lens current. (a) Decreasing current; (b) increasing current.

by turning the knob counterclockwise (CCW) or using computer controls, magnetic field is weakened, so the focal length f is getting longer (Fig. 3.6a). Turning the knob clockwise (CW) shortens the focal length f (Fig. 3.6b). The relationship between f and the lens current i is expressed as

$$f = K(\frac{V}{i^2}) \tag{3.4}$$

Here, V is the acceleration voltage, and K is a constant. As shown in Fig. 3.7, by controlling the lens current to change the focal length f, it is possible to get an overfocused image (the image appears above the image plan, Fig. 3.7a), in-focus or focused image (in the image plan, Fig. 3.7b), or underfocused image (below the image plan, Fig. 3.7c).

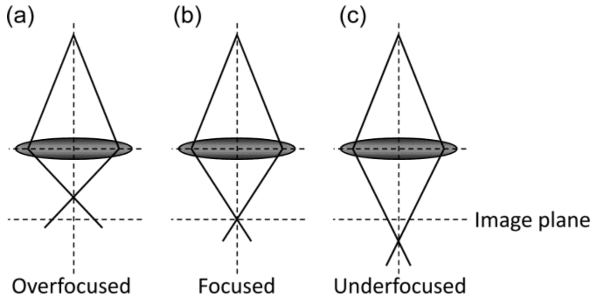

Fig. 3.7 Focus of lens. (a) Overfocused; (b) focused; (c) underfocused.

3.1.3 Condenser Lenses and Condenser Apertures

The condenser lenses are located above the specimen, as shown in Fig. 3.1. They function as controls of the electron beam illuminations on the specimen. Basically there are two condenser lenses, one is condenser lens 1 (C1), which controls the beam size, and another is condenser lens 2 (C2), which controls the beam intensity.

The C1 reduces the image of the filament so that it is possible to get small spot of the beam. In the example shown in Fig. 3.8, suppose the gun crossover is 50 μm. If the C1 is strengthened with a higher lens current to get a shorter focal length f (Fig. 3.8a), the image of the gun crossover is reduced, say 1.5 μm. This image is slightly magnified by C2 to get a final probe with a size, say 2 μm, on the specimen. However, if the C1 is weakened with a lower lens current to get a longer focal length f (Fig. 3.8b), the image of the gun crossover is reduced but at a larger size, say 5 μm, than in Fig. 3.8(a). This image is slightly magnified by C2 to get a final probe with a size, say 10 μm, on the specimen. In such a way, the spot size can be controlled by C1.

The C2 is used to control the beam brightness, as shown in Fig. 3.9. The brightness knob controls the lens current of C2. Turning the brightness knob CCW reduces the lens current, and if it passes the crossover point, the beam is spread on the screen (underfocused), as shown in Fig. 3.9(a). At the crossover point, the smallest beam is obtained, as shown in Fig. 3.9(b). One should be cautious for not leaving the beam on the screen for a long time, since it is at the strongest intensity on the illuminated area, which may damage the screen. After the crossover point, if the brightness knob is turned CW, the beam is again spread on the screen, but it is underfocused (Fig. 3.9c).

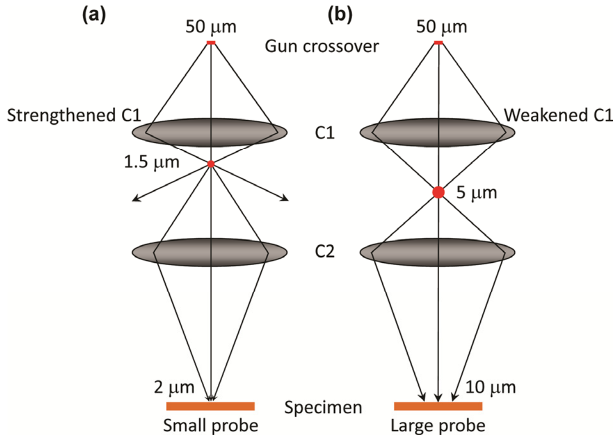

Fig. 3.8 Condenser lens 1 (C1) that controls the beam size. (a) Strengthened C1 to get a small probe on the specimen; (b) weakened C1 to get a large probe on the specimen.

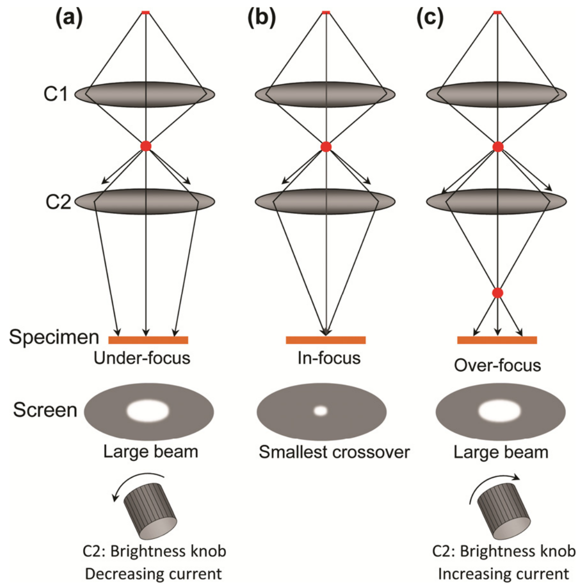

Fig. 3.9 Condenser lens 2 (C2) that controls the beam brightness. (a) Underfocus the beam to get a larger area illumination; (b) in-focus the image to get the smallest beam crossover on the specimen; (c) overfocus the beam to get a larger area illumination. The brightness knob controls C2.

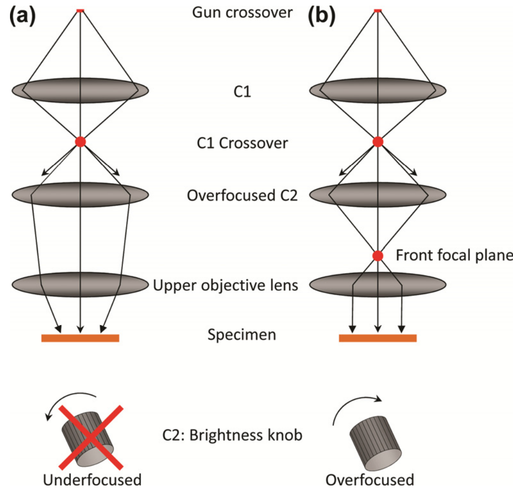

Fig. 3.10 (a) Underfocusing C2 (turning the brightness knob CCW beyond the crossover) results in nonparallel illumination on specimen; (b) overfocusing C2 produces parallel illumination.

It is very important to keep C2 overfocused for imaging. The reason is explained in Fig. 3.10. If C2 is underfocused, after the upper objective lens, the rays illuminating the specimen are not parallel, as shown in Fig. 3.10(a). While in the case of C2 that is overfocused, as shown in Fig. 3.10(b), after the upper objective lens, the rays become parallel before reaching the specimen. Therefore, during the TEM experiment, keep in mind to leave C2 overfocused (turn the brightness knob CW beyond the crossover point). If it is unsure whether the beam is underfocused or overfocused, turn the brightness knob to find out the focusing condition. For example, turn the brightness knob CW; if the beam is getting weaker, it is already overfocused, whereas if the beam is getting stronger it is underfocused.

The C1 aperture below the C1 lens is fixed, which is not changeable for the user. However, the C2 aperture (the condenser aperture) size can be selected. As shown in Fig. 3.11, a smaller condenser aperture reduces the semiangle α, but the intensity is reduced; a larger condenser aperture increases the semiangle α, and the intensity is also stronger. The user has the option to select a smaller aperture for high-resolution imaging, and a larger aperture for general observations. Normally it stays at the middle (#2 or #3). If the aperture is changed, proper alignments should be followed immediately (refer to Section 3.2).

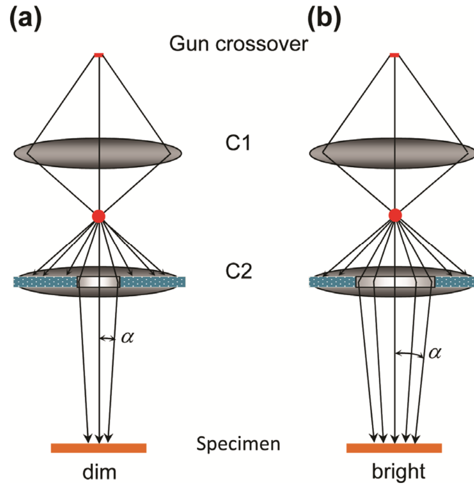

Fig. 3.11 Condenser aperture. (a) Smaller aperture; (b) larger aperture.

3.1.4 Objective Lens and Objective Aperture

The objective lens is used for focusing and magnifying the object. It is the most important lens since it forms the first image and diffraction pattern of the specimen, and the image and diffraction pattern are then further magnified by the following intermediate and project lenses. Any distortions in the first image or diffraction pattern will become severe after high magnifications.

The TEM specimen is inserted in the gap of the objective lens polepiece, as shown in Fig. 3.12(a). In the TEM design, the polepiece gap is very limited. Depending on the application, the polepiece configuration varies. An analytical type TEM has a larger gap for large-angle tilting and for EDS detector configuration, while a high-resolution-type TEM has a smaller gap for a higher resolution imaging. Some polepieces can compromise these two needs. On some TEMs, the types of polepieces can be switched, while extensive services are required.

The objective aperture normally locates in the back focal plane, which is just below the specimen (few millimeters). Therefore, it should be very cautious for not touching the aperture when the specimen is tilted to large angles or is lowered largely along z direction. This aperture is used for regular imaging, including high-resolution imaging.

Some microscopes contain a high-contrast objective aperture. As shown in Fig. 3.12(b), the high-contrast objective aperture only passes electron in the center of the diffraction beam for imaging, which is equivalent to a smaller aperture. The image thus has a higher contrast (the contrast will be discussed in Chapter 4). Since this aperture is far away from the specimen holder, no collision of them would happen.

The usual appearance of the TEM column is shown in Fig. 3.12(c). The inner objective lens polepiece is taken out in Fig. 3.12(d) and (e). An anticontamination device (ACD) is attached around the specimen, which is cooled down using liquid nitrogen to reduce the contamination on the TEM specimen and improves the vacuum level of the TEM column.

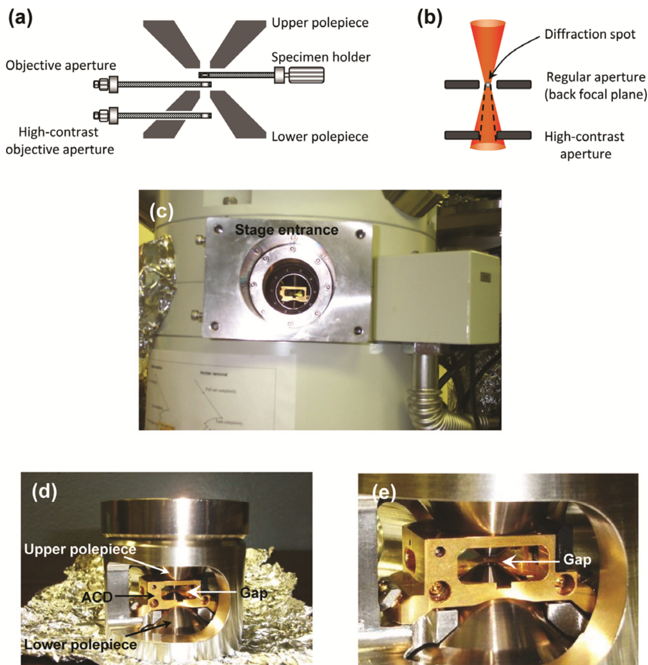

Fig. 3.12 (a) Objective lens and objective apertures; (b) comparison of regular objective aperture and high-contrast objective aperture; (c) appearance of a stage entrance (the stage was disassembled from the column) and the center is the gap that the specimen holder enters; (d) objective lens polepiece (the specimen holder enters to the gap); (e) enlarged view of (d).

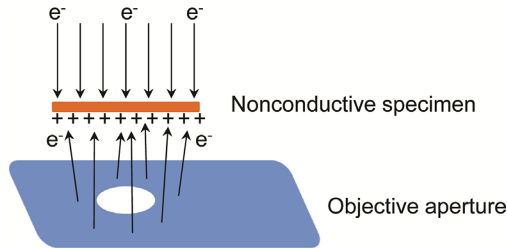

Fig. 3.13 Stabilization of sample by objective aperture under the specimen.

Another function of the regular objective aperture, which is below the specimen, is stabilizing nonconductive samples, such as polymer thin sections [3]. If the sample is nonconductive, upon high-energy electron bombardment, some portion of electrons of the specimen atoms are knocked off, leaving the sample positively charged, as shown in Fig. 3.13. However, if the objective aperture is inserted, electrons shooting on the aperture diaphragm may be backscattered to the bottom side of the specimen, so that the specimen is partially neutralized. This effect is very evident for thin sections prepared by microtomy. For this reason, the metal grid bar should be installed on the bottom side of support film or thin sections to minimize any possible charging effect. However, the high-contrast objective aperture makes no obvious stabilization effect on the specimen. These two apertures can be used simultaneously.

3.1.5 Intermediate Lens and Diffraction Aperture

The intermediate lens is used to magnify the image and for selection between imaging and diffraction mode. After the electrons pass through the specimen, a diffraction pattern is formed in the back focal plane, and then the first image is formed. As shown in Fig. 3.14(a), if the intermediate lens focuses on the first image, this image is further magnified by the following lenses, so that a magnified image appears on the screen. However, if the intermediate lens focuses on the first diffraction pattern in the back focal plane of the specimen, as shown in Fig. 3.14(b), this pattern is further magnified by the following lenses, so that a diffraction pattern appears on the screen. Note that the diffraction pattern always forms in the back focal plane, no matter whether the TEM is in the imaging mode or diffraction mode.

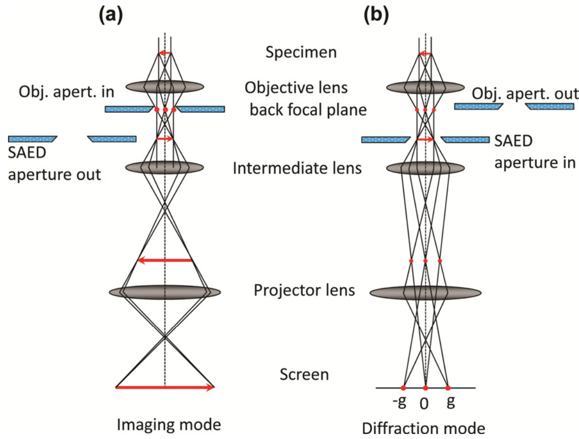

Fig. 3.14 Imaging and diffraction mode determined by intermediate lens. (a) Imaging mode; (b) diffraction mode.

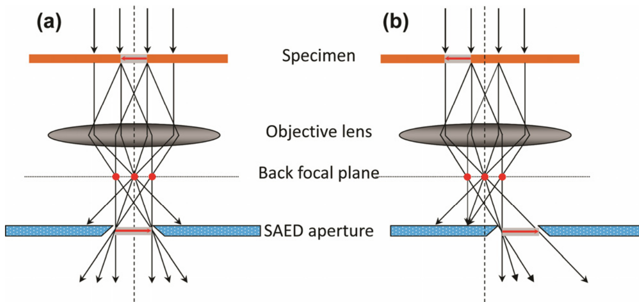

Fig. 3.15 Selecting an area for diffraction using SAED aperture. (a) SAED is centered; (b) SAED is off the central axis.

In order to get a selected-area electron diffraction (SAED) pattern from certain area, a diffraction aperture or SAED aperture is used to choose the area to be diffracted. It should be noticed that the SAED aperture does not locate above the specimen but below it, in the first image plane (Fig. 3.15). In Fig. 3.15(a), the SAED aperture is located along the central axis to select a small area for the diffraction, which limits diffraction information only from the central small area on the real sample on the top. If the SAED is off the optical axis, it still can be used to select an area, so that the diffraction pattern comes only from a specific area, as shown in Fig. 3.15(b). However, to get a higher quality pattern, the SAED aperture should be aligned in the center; therefore, move the specimen to the center and then insert the aperture for diffraction.

3.1.6 Projector Lens

The projector lens is used to further magnify the images formed by the intermediate lens. The projector lens has a great depth of focus—the final images remain in focus for a long distance along the optical axis.

The final image magnification M is

$$M = M_{\mathrm{Obj}} \times M_{\mathrm{Int}} \times M_{\mathrm{Proj}} \tag{3.5}$$

Here, M_{Obj}, M_{Int}, and M_{Proj} are the magnifications of the objective, intermediate, and projector lenses, respectively.

3.1.7 Viewing Screen and Camera

The viewing screen is coated with phosphorescent powders, which emit visible lights upon being bombarded by high-energy electrons. It should be noticed that intense exposure can damage the screen. A focused beam crossover in the image mode at a low magnification, or diffraction spots in the diffraction mode, possesses strong intensities, which may damage the viewing screen. Use beam stopper or other ways to reduce the beam intensity, or use a small screen to view the beam to protect the large screen.

Recording can be done by a film camera or a CCD camera. As the film camera directly connects to the viewing chamber, a high vacuum level is required. Negative films should be pre-evacuated for sufficient period of time (several hours) in a desiccator before they are placed in the TEM camera. The exposed films are processed by regular procedures, including developing, rinsing, fixing, rinsing, and drying. The final films may be used for printing on photographic papers, while nowadays few people work in this way, but the negative films should be scanned using a general scanner in a transparent mode so that the lights pass through the negative films. After scanning, the data on the negative films are transferred to digital forms.

If a CCD camera is available, the TEM data are recorded directly to digital files. Similar to viewing screen, precautions should be taken to avoid exposing the CCD camera to very high brightness spots.

It is a good habit to well organize the TEM data, such as using a folder name of "date_project name," and each file is named as "sample name_magnification (or camera length)_sequence number" or "sample name_sequence number." It is better to include the sample name and magnification (for images) or camera length (CL, for diffraction patterns) information in the file names. It is recommended to keep both the original data format (such as Gatan DigitalMicrograph) and converted image format (such as TIFF) in the archives.

3.2 Instrument Imperfections, Alignments, Corrections, and Calibrations

Since the TEM instrument is not perfect, imperfections always exist in the TEM system. Some of the imperfections can be aligned or corrected at the user level, while some of them have to be done by new designs of the components by manufacturers.

3.2.1 Beam Shift and Beam Tilt

The beam shift and beam tilt are controlled by condenser lens deflector coils, whose locations are indicated in Fig. 3.1. The deflection coils comprise a pair of upper and lower deflections, as marked with DEF 1 and DEF 2, respectively, in Fig. 3.16 (only a pair is shown in Fig. 3.1 for simplicity). If DEF 1 deflects the beam to an angle θ and DEF 2 deflects the beam to the same angle θ but in an opposite direction, the beam is shifted to a distance in the same direction (Fig. 3.16a). If this beam is parallel to the optical axis, it should be deflected to the center focal point in the back focal plane. This point is called as pivot point, which is used for the alignment. However, as shown in Fig. 3.16(b), if DEF 2 deflects at a larger angle $\theta + \beta$, the beam can return back to the same position (or any other location) on the sample (pivot point) while it is tilted with an angle β, the angle difference by DEF 1 and DEF 2. This beam is deflected by the objective lens to a path parallel to the optical axis, since the pivot point is at the front focal point position.

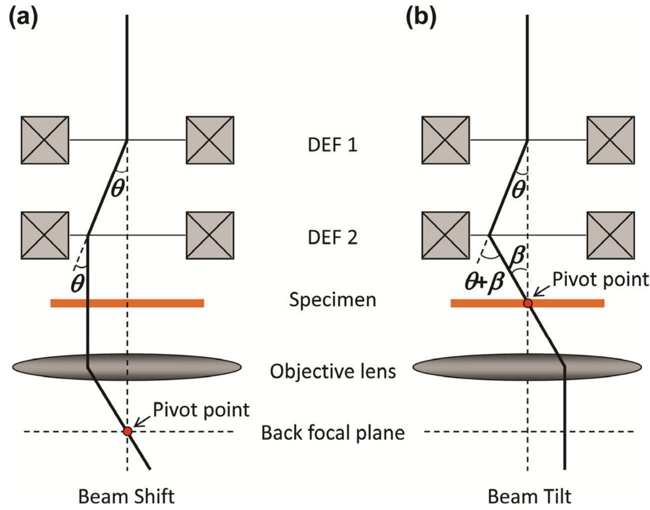

Fig. 3.16 Beam shift (a) and beam tilt (b) by deflector coils.

It should be noticed that the deflectors should be well aligned to get pure shift or pure tilt, or the shift and tilt could be mixed, that is, the operation of beam shift may produce beam tilt, and the beam tilt may produce beam shift. If high-resolution imaging is needed, such shift/tilt purity alignment using the pivot points is required to center the pivot points.

3.2.2 *Spherical Aberration*

Spherical aberration is caused by the imperfection of the lens, which cannot focus rays to the same point, as shown in Fig. 3.17. If the semi-angle of collection of the lens is β, the radius of the refracted rays on the image plane is

$$r_{\mathrm{sph}} = C_{\mathrm{s}}\beta^3 \tag{3.6}$$

where C_s is the coefficient of spherical aberration.

As will be discussed in the Chapter 7 in Volume 2, C_s is a major factor that limits the microscope resolution. A lower C_s improves the resolution. For a given conventional TEM, the C_s is always present, which cannot be corrected by the user. New developments in spherical aberration correction have made it possible to eliminate C_s to improve the resolution [4–10].

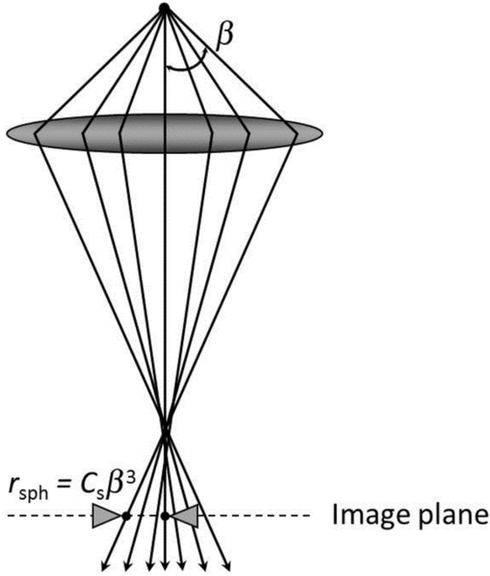

Fig. 3.17 Spherical aberration.

3.2.3 Chromatic Aberration

Generated by the electron guns, the accelerated electrons do not have the exactly same energy but with energy variations. Therefore, these electrons are deflected to different angles. Electrons with higher energy are deflected to a lower angle, while electrons with lower energy are deflected to a larger angle, as shown in Fig. 3.18. These electrons form a disk instead of a point, and the disk diameter r_{chr} is

$$r_{chr} = C_c \frac{\Delta E}{E_0} \beta \tag{3.7}$$

where C_c is the chromatic aberration coefficient of the lens, ΔE is the full range of energy, E_0 is the initial energy, and β is the semiangle of collection of the lens.

The presence of chromatic aberration will cause difficulties to focusing the image. A smaller ΔE, smaller β (smaller aperture if possible), or a higher E_0 (higher accelerating voltage) will result in a smaller chromatic aberration r_{chr}. It should be noted that although the energy spread of the electrons coming from the filament is small (refer to Table 3.1), ΔE

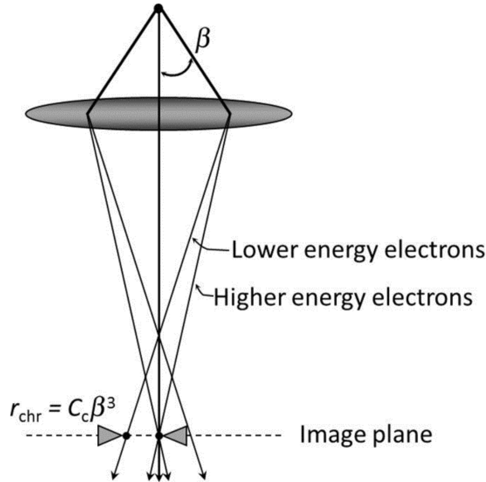

Fig. 3.18 Chromatic aberration.

becomes larger after passing through a thin sample, which typically reaches few tens eV. If it is a thick sample, ΔE is significantly even higher, causing a focusing problem. To reduce the chromatic aberration effect, possible solutions include reducing the sample thickness, using a smaller objective aperture to reduce β, and using the highest possible accelerating voltage. Similar to C_s correction, new developments have been made to correct C_c [11–15].

3.2.4 Depth of Field and Depth of Focus

The depth of field, D_{ob}, is the tolerance range of distance along the optical axis in which the specimen can move without detectable loss of sharpness near the object plane. As shown in Fig. 3.19(a), if the object moves to the upper position 1, the image moves to the lower position 4; and if the object moves to position 2, the image moves to position 3. Suppose the collection semiangle is β and the distance range in the object plane is d_{ob}, since β is very small we have

$$D_{ob} = \frac{d_{ob}}{\beta} \tag{3.8}$$

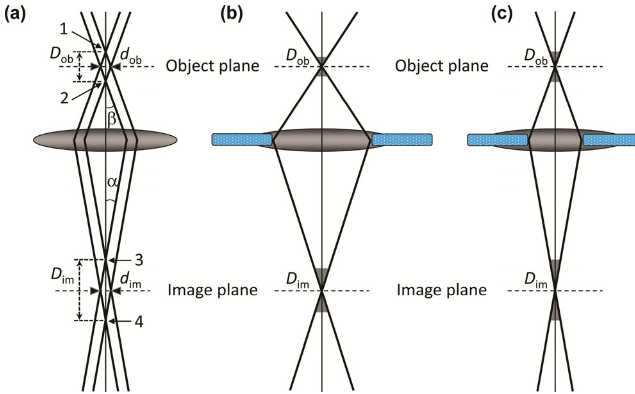

Fig. 3.19 (a) Definition of depth of field D_{ob} and depth of focus D_{im}; (b) larger aperture produces shorter D_{ob} and D_{im}; (b) smaller aperture produces longer D_{ob} and D_{im}.

The depth of focus, D_{im}, is the tolerance range near the image plane in which the image appears sharp (assuming the object and the lens are fixed). The lens magnification is expressed as

$$M = \frac{d_{\text{im}}}{d_{\text{ob}}} = \frac{\beta}{\alpha} \tag{3.9}$$

Thus,

$$D_{\text{im}} = \frac{d_{\text{im}}}{\alpha} = \frac{d_{\text{ob}}}{\beta} M^2 \tag{3.10}$$

From Eq. 3.8 and 3.10, it is apparent that if smaller aperture is used, β is lower and extended D_{ob} and D_{im} are obtained, as shown in Fig. 3.19(b) and (c). Since the TEM deals with high magnification, the depth of focus D_{im} is very large, that is, the image can stay in-focus within a wide range of distance using different cameras, for example, the film camera or CCD camera below it, although their magnifications will change.

3.2.5 Specimen Height

The TEM specimen in the holder has freedoms of *x* and *y* transitions in the *x*–*y* plane and moves up or down along the *z*-height, as shown in Fig. 3.20. If tilting capabilities are available, a single-tilt holder can tilt

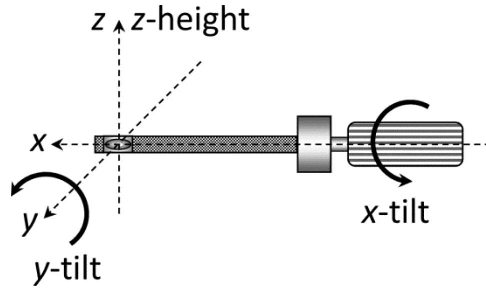

Fig. 3.20 Specimen holder with freedoms of x and y transitions, z-height, and x- and y-tilts.

the sample along the *x*-axis (*x*-tilt), and a double-tilt holder can tilt along both *x*-axis and *y*-axis (*y*-tilt). Depending on the objective lens polepiece configuration and the specimen holder, the range of tilting is limited.

Moving the specimen up or down mechanically can focus the image. This should not be confused with focusing using objective lens, which changes the lens current and thus the focal length *f*. If the objective lens focus is adjusted largely, the alignments may be getting worse and the image magnification also changes. Therefore, the objective lens current should stay around a standard value, and the current should be slightly changed for focusing. If the sample is largely out of focus, it should be focused using the *z*-height first and then finely tuned by the objective lens for focusing.

Tilting the specimen holder is a basic skill in TEM operation, such as for electron diffraction or tomography studies. In order to keep the same viewing area while tilting, the sample should be set at an eucentric position, so that the holder axis is the tilting axis. This can be done by adjusting *z* while tilting *x*-tilt largely until the image remains almost the same location.

3.2.6 *Astigmatism*

Astigmatism is caused by the lens soft iron polepieces, which cannot be machined perfectly with cylindrical symmetry. Inside the iron material, microstructural inhomogeneities may also cause variations of magnetic

field. In addition, the aperture geometry (a perfect circle), location (exactly aligned along the optical axis), and any built-up contaminations on the aperture will cause astigmatism. The astigmatism r_{ast} will cause difference in focus, that is,

$$r_{ast} = \beta \Delta f \tag{3.11}$$

where Δf is the maximum difference in focus induced by the astigmatism.

The astigmatism can be carefully corrected using stigmators (refer to Fig. 3.1), including condenser lens stigmator to correct the illumination beam, objective stigmator to correct the astigmatisms in the image, and intermediate lens stigmator to correct the astigmatisms in the diffraction pattern.

An example is shown in Fig. 3.21 for a LaB_6 beam. With the presence of condenser lens astigmatism, the beam is stretched and the stretching direction rotates 90° crossing from an underfocused to an overfocused condition, or from an overfocused to an underfocused condition, as shown in Fig. 3.21(a) and (b). However, if the astigmatism is carefully corrected, the beam becomes circular no matter it is at underfocused or overfocused condition (Fig. 3.21c).

The objective lens astigmatisms appeared in the image can be corrected with the aid of fast Fourier transformation (FFT) patterns of high-resolution TEM (HRTEM) image of amorphous carbon film, as shown in Fig. 3.22. If no astigmatism is present, the FFT displays only

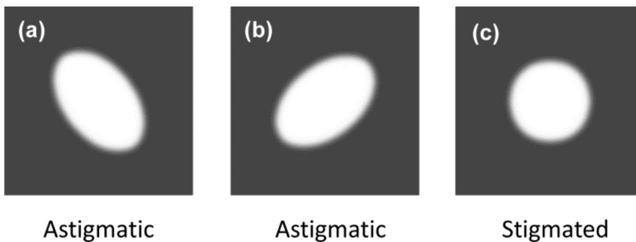

***Fig. 3.21** Schematic LaB_6 filament beam. (a, b) Astigmatic but one is underfocused and another one is overfocused, and the two image stretching directions are perpendicular; (c) stigmated, no distortions at either underfocus or overfocus conditions.*

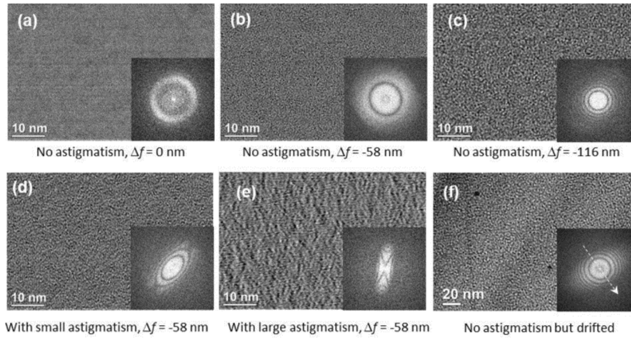

Fig. 3.22 Correction of objective lens astigmatism using FFT. (a–c) No astigmatism but at different defocus Δf; (d, e) with astigmatism at different defocus Δf; (f) no astigmatism but the sample drifts along the direction indicated with an arrow.

circular rings (Fig. 3.22a–c). However, if astigmatism is present, the FFT pattern is distorted, as shown in Fig. 3.22(d) and (e) at different defocus values. If the sample drifts, some information is cut off along the drifting direction, as shown in Fig. 3.22(f).

To correct the astigmatism, there are X and Y knobs (or X and Y controls in the computer interface) controlling the stigmators. While turning the X or Y knobs, check what changes are made on the beam shape for condenser lens astigmatism, or on real image and its FFT pattern for objective lens astigmatism, and adjust X and Y knobs accordingly. The following steps should be used:

1. Coarse tune the X knob in one direction (such as CCW) until the astigmatism is getting worse, and then turn it in the other direction (CW) until it gets worse again. Return to the middle point between the two extreme points;
2. Work on the Y knob in the same way to find out the middle point for the Y knob;
3. Finely tune X and Y knobs. For objective lens astigmatism correction, it is recommended to use the FFT patterns, since it is difficult to see small astigmatism from the image by naked eyes, especially if the FEG is used;
4. When the astigmatism is corrected, deactivate the X/Y knobs to avoid accidentally touching them.

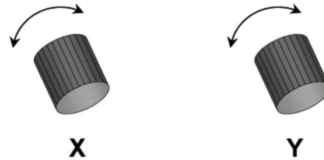

Fig. 3.23 Correction of astigmatism using X and Y stigmators. Turning X and Y knobs back and forth until the best position is found.

3.2.7 Aperture Alignment

There are several apertures on the TEM, such as condenser, objective, and diffraction apertures. Each aperture is controlled by two knobs on it to align it in the *x–y* plane. In practice, it is common to misalign these two knobs, especially for beginners, and sometimes it is hard to refind the correct alignment if both knobs are in incorrect positions. One could use the following way to find the aperture: turn both knobs to one end, and turn knob 1 gradually while doing a full range scan of the knob 2 until both knobs reach the right position to see the beam. This method would take a long time. A better solution is done in the following procedure:

1. When the knob is at the right position, stick or mark an arrow on the knob pointing up (there may be already a marker on the knob), as shown in Fig. 3.24(a).
2. Fully turn this knob CW slowly until it reaches the end and use a notebook to record down the number of turns. For example, after $2\frac{5}{8}$ turns, it reaches the position shown in Fig. 3.23(b).
3. Repeat the steps 1 and 2 for the other knob of this aperture.
4. In case the aperture is misaligned, fully turn both knobs CW until they stop. Then turn them CCW for the number of turns recorded in step 2, so that both knobs will return back to the right positions quickly. For example, turning the knob in Fig. 3.24(b) CCW for $2\frac{5}{8}$ turns will bring it to the original correct position with the arrow pointing up.

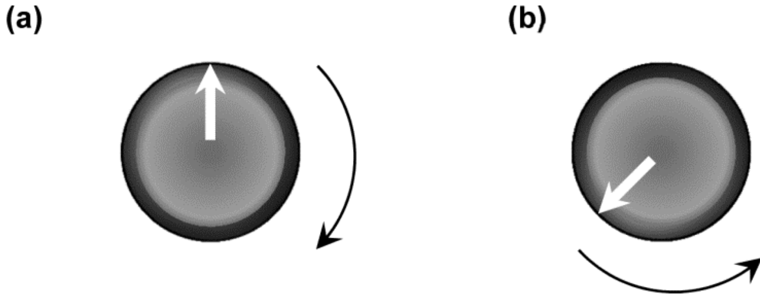

***Fig. 3.24 The way to find a missing aperture. (a) Position at normal position with an arrow pointing up; (b) the end position when the knob is fully turned* CW.**

3.2.8 Magnification Calibration

A magnification of an image given by the manufacturer is only an approximate value, and the real magnification may vary from time to time, with an error that could reach in the range of 3%–10%. Therefore, magnification calibration should be routinely performed.

Table 3.3 lists the results from a routine magnification calibration of a TEM instrument. The nominal magnification is the magnification displayed on the instrument panel, which is supposed to be the magnification of the film camera. (Note that the magnification on the screen should be smaller than the magnification on the film since it is located at a higher position.) Although these magnifications are mostly close, some errors are large, for example, the 600,000× is indeed 641,645× with 6.94% error. Without the calibration, it is impossible to know whether the error existed.

At magnifications of 80,000× or below, the magnification can be calibrated using commercial cross-grating replica, as shown in Fig. 3.25(a), which features 2,160 lines/mm, or 0.462963 μm/line. If it is calibrated using a film, draw a line perpendicular to the grating replica lines and cross as many lines as possible (to reduce error), and the magnification is

$$M = \frac{2160d}{n} \qquad (3.12)$$

Table 3.3 Example of magnification calibration showing the nominal and calibrated magnifications.

Nominal magnification	Calibrated magnification	Error (%)
1,000,000	992,234	–0.78
800,000	777,250	–2.84
600,000	641,645	6.94
500,000	529,192	5.84
400,000	416,738	4.18
300,000	317,515	5.84
250,000	257,981	3.19
200,000	205,062	2.53
150,000	157,104	4.74
120,000	125,683	4.74
100,000	102,369	2.37
80,000	81,976	2.47
60,000	62,288	3.81
50,000	50,545	1.09
40,000	39,652	–0.87
30,000	29,117	–2.94
25,000	24,985	–0.06
20,000	19,473	–2.64
15,000	14,710	–1.93
12,000	12,038	0.32
10,000	9,952	–0.48
8,000	7,981	–0.24
6,000	6,048	0.80
5,000	5,076	1.52

Here, d is the distance (mm) between lines on a film, and n is the number of spaces between grating replica lines. For accurate measurement, a longer distance d with more numbers n should be selected. The negative films should be used rather than using images printed on photographic paper, which may distort the distance.

If a CCD camera is used for calibration, it is needed to draw a line to cover as many lines as possible, and enter a known distance of $0.462963n$ μm, where n is the number of spaces measured.

However, if the magnification is at 100,000× or higher, as shown in Fig. 3.25(b), the replica is no longer suitable for the calibration since it would cause large error from uncertain lines. The user may choose other commercial standards or structures with known distance. For example, SiC crystal is good standard for the high magnification calibration. It has a hexagonal structure with a = 0.30807 nm, c = 1.51174 nm, and space group of $P6_3mc$ [16]. Its (0001) lattice fringes can be quickly found, as shown in Fig. 3.25(c) and (d). It does not require to get a well-aligned zone axis or a very thin area for the calibration. Only fringes are needed, and the fringe spacing is $d_{(0001)}$ = 1.51174 nm. This standard can be used for calibration from 100,000× to the highest possible magnification.

3.2.9 Camera Length Calibration

Similar to the magnification calibration in the image mode, the CL calibration in the diffraction mode also should be routinely conducted. An example from a routine calibration is given in Table 3.4, showing the error between nominal CL and calibrated CL.

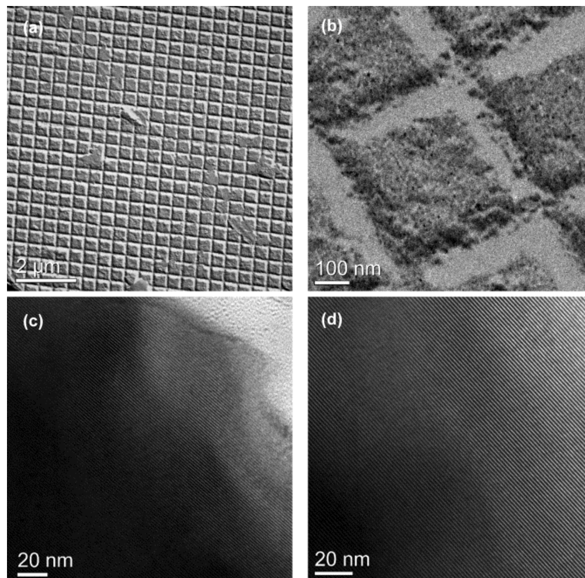

Fig. 3.25 Magnification calibration. (a, b) calibration using grating replica; (c, d) calibration using SiC lattice fringes with spacing of c = 1.51174 nm.

Table 3.4 Example of CL calibration showing the nominal and calibrated CL.

Nominal CL (cm)	Calibrated CL (cm)	Error (%)	Camera constant (Å·mm)
150	152.99	1.99	38.4
100	102.39	2.39	25.7
80	79.8	–0.25	20.03
60	59.63	–0.62	14.97
50	51.2	2.40	12.85
40	40.91	2.27	10.27

The CL calibration can be done using commercial standard of polycrystalline Al thin foil, which gives rise to a ring pattern. If the pattern is recorded on a film, as shown in Fig. 3.26, use a ruler to get the ring radiuses R (it is better to measure diameter to get the radius). The lattice constant d of each ring is known. As will be discussed in the Chapter 4, we have

$$Rd = L\lambda \tag{3.13}$$

Here L is the camera length, λ is the wavelength, and the product of $L\lambda$ is camera constant (mm·Å). The results of the example in Fig. 3.26 are listed in Table 3.5. From several rings, the averaged camera constant or camera length can be obtained.

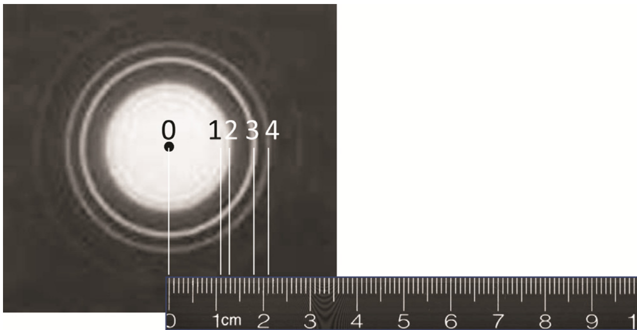

Fig. 3.26 Camera length calibration using polycrystalline Al thin foil, and the SAED pattern is taken on a film.

Table 3.5 Measurement of CL from the diffraction pattern in Fig. 3.26.

Radius, *R* (mm)	**Lattice spacing, *d* (Å)**	**Camera constant, $L\lambda$ (mm·Å)**	**Camera length, *L* (mm)**
11.1	d_{111} = 2.338	25.95	1,033.94
12.8	d_{200} = 2.025	25.92	1,032.67
18.1	d_{220} = 1.432	25.92	1,032.64
21.2	d_{311} = 1.221	25.89	1,031.28
Average		25.92	1,032.63

When the camera constant $L\lambda$ is known, for any reflection with a distance R to the center beam, its lattice spacing is thus

$$d = \frac{L\lambda}{R} \tag{3.14}$$

where R is measured in mm, and d is in Å.

If the calibration is done using a CCD camera, enter the known lattice spacing to each ring. At lower camera length (≤20 cm), polycrystalline Al rings are used for the calibration, as shown in Fig. 3.27.

A pattern taken on the film is indicated by a camera length (like 100 cm), while a pattern taken by a CCD camera is indicated with a length in reciprocal space. Using this scale bar, it is possible to measure the spacing of each reflection spot. For example, as shown in Fig. 3.27, the scale bar indicates a number of $5\frac{1}{\text{nm}}$, which corresponds to 0.2 nm spacing in real space ($\frac{1}{5} = 0.2$). If the scale bar length is measured as 380 pixels (or in any other unit), according to Eq. 3.13,

$$Rd = 380 \times 0.2 \text{ pixel} \cdot \text{nm} = L\lambda(\text{constant.}) \tag{3.15}$$

If the distance of any other reflection to the central spot is measured as R, its spacing is thus

$$d = \frac{380 \times 0.2}{R} \tag{3.16}$$

However, normally it is possible to read out the d spacing directly using the CCD acquisition software.

Similar to the magnification calibration, at higher camera length (>200 cm), the ring becomes too big for the measurement. Again, the SiC crystal can be used for calibration, as shown in Fig. 3.28. Its (0001) spot is very close to the center beam (0000), with spacing $d_{(0001)}$ = 1.51174 nm. If (0002) is selected (the second spot), its spacing $d_{(0002)}$ = 0.75587 nm, and so on.

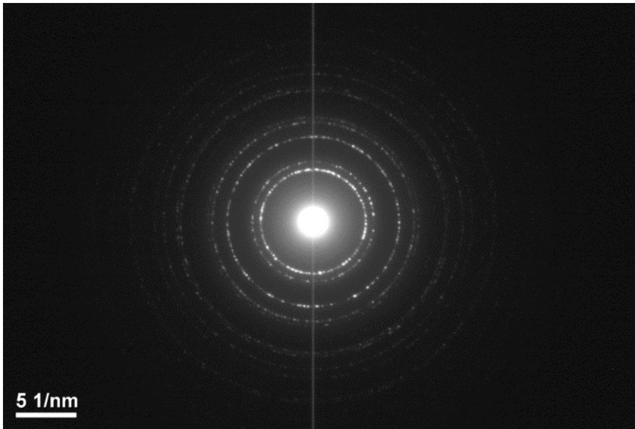

***Fig. 3.27** Diffraction pattern from polycrystalline Al thin foil taken by a CCD camera.*

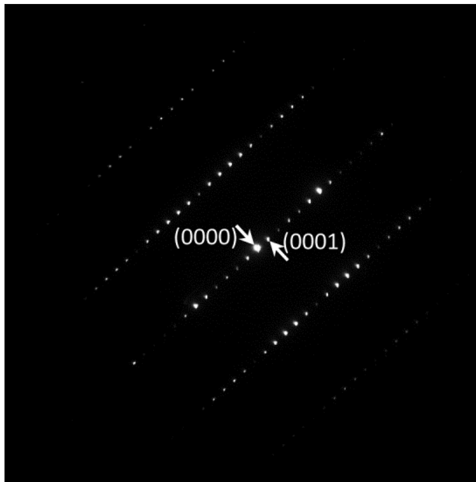

***Fig. 3.28** Camera length calibration using SiC single crystal with the nearest spot (0001) spacing d = 1.51174 nm.*

3.2.10 *Magnetic Rotation Calibration*

A magnetic rotation between the image and diffraction pattern is caused by the magnetic lenses. Some TEMs have already corrected such rotations, such as TEMs made by JEOL and Hitachi. If not corrected by the manufacturer, the TEM user needs to correct it in order to analyze the relationship between diffraction and image.

The magnetic rotation is related to two factors: magnification in the imaging mode and the camera length in the diffraction mode. At different magnification, the image may rotate; the same situation occurs for electron diffraction pattern, which may rotate with different camera length. Therefore, it is necessary to calibrate such rotation at each magnification with each different camera length.

The calibration can be done using any defined shapes with known crystallographic orientations, such as twins that will be given in Chapter 4, or long-period structures whose stacking basal planes can be visualized even at a lower magnification. An example of SiC crystal is shown in Fig. 3.29. On the image, the (0001) basal plane can be easily found, as indicated. Without the magnetic rotation, the diffraction row should appear on the perpendicular direction of the basal plane. However, in the SAED pattern, the diffraction row is rotated CW 23.4°. Therefore, the magnetic rotation is CW 23.4° for this magnification and camera length.

After the calibration at different magnification and camera length, one may list a table of magnetic rotation as a function of magnification and camera length.

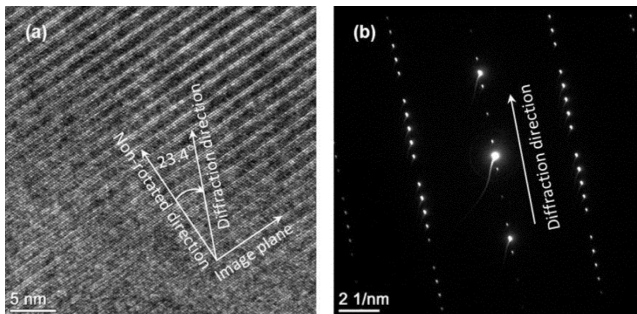

***Fig. 3.29** Magnetic rotation calibration. (a) Image with packing basal plane direction indicated; (b) diffraction pattern with diffraction direction of closely spaced rows indicated.*

3.3 TEM Operating Procedures

Depending on the type of TEM instrument, the operating procedures may vary. The following are common procedures to operate the TEM.

3.3.1 *Startup*

1. Login the user account or sign in the instrument.
2. Ensure the vacuum is normal.
3. Fill the cold-trap dewar with liquid nitrogen (remember to refill after 3 h to keep it cooled).
4. Set the accelerating voltage if it is not on. If it is a 200-kV TEM, raise the voltage to 100 kV, which can be done quickly (in few minutes), but raise slowly to 160 kV (in 10 min), and wait for 10 min, then to 200 kV in 15 min.

3.3.2 *Specimen Loading and Unloading*

Check the design of the specimen holder and look at the holder motion diagram for instruction. Special caution should be taken during this step, since the operating troubles often happen during the specimen loading and unloading process, either causing mechanical damage of the parts or breaking of the vacuum. The following are important steps:

1. Ensure the sample is clean, dried, and supported such that it will not drop off from the holder to contaminate the instrument.
2. On the instrument ensure the specimen holder positions (x, y, and z) and goniometer angles (x- and y-tilt) are all at zero positions, and if not, reset them first.
3. If it is a double-tilt holder, work with it very gently to avoid breaking its y-tilt pivots.
4. After a specimen is mounted on the holder, flip the holder to let the sample face down and gently tamp the holder to make sure the sample is securely mounted and does not drop off the holder.

3.3.3 *Alignments*

1. Eucentric height adjustment

   When the sample is inserted, slowly turn on the beam if it is off, or open the valve if the filament is already on. Tilt around *x*-axis extensively and adjust *z*-height to get a position that the image shifts only a minimum distance on the screen. This position is the eucentric height.

2. Gun alignment

   First check the Gun Tilt to get a maximum brightness. Then center the beam in the following way:

   a. Select spot size #1 (largest one) and center the beam using Gun Shift X and Y.
   b. Select spot size #4 or #5 (smaller size) and center the beam using Shift X and Y of the condenser lens.
   c. Repeat steps a and b for several times until the beam stays at the center while changing the spot size.
   d. Set the spot size at #2 or #3, which is the spot size to be used.

3. Condenser lens astigmatism correction

   a. Insert and select a condenser aperture if necessary (normally this is already done). Use the Brightness knob to get a beam crossover (smallest beam) and center it using Shift X and Y (on the panel) of the condenser lens. Expand the beam CW (overfocused) to the full screen size, and then center the beam using two screws on the condenser aperture apparatus.
   b. Correct for astigmatism to get a circular beam using condenser lens stigmators.

4. Voltage centering

   Move an object, such as a small particle or the tip of a sharp object, to the screen center. Activate high-tension (HT) Wobbler, which adds fluctuation to the accelerating voltage so that the image wobbles. Adjust the Tilt X and Y of the condenser lens deflectors until the center of the image is almost stationary. Use binoculars to align it finely. Turn off the HT Wobbler.

   Although some instruments have current centering function, only one centering alignment is needed. Normally it is the voltage centering that is aligned.

5. Objective lens astigmatism correction
   a. Find an amorphous thin area (such as carbon support film or the hole edge of ion-milled sample).
   b. Insert the diffraction aperture and center it using two screws on it.
   c. Switch to diffraction mode and center the diffraction pattern using Shift X and Y of the Project Deflector.
   d. Select an objective aperture and center it, then return back to image mode.
   e. Change the magnification to a higher magnification (over 200,000×) and focus the image.
   f. Adjust the beam brightness to ensure the beam is not too intensive and then turn the image to the CCD camera, or a video camera, or use binoculars to correct the objective astigmatism from the image (refer to Section 3.2.6).

3.3.4 *Data Recording*

1. Move the viewing image or diffraction pattern to the center of the screen and ensure the information falls into the recoding area of the film or CCD camera.
2. Adjust the beam brightness to avoid overexposure or damage to the CCD camera. For a diffraction pattern, a beam stopper may be used to cut off the intensity of the strongest beam.
3. Select an exposure time for recoding. Do not leave the pattern on the CCD camera for a long time, as the strong beam may damage the camera.

3.3.5 *Finishing*

1. Slowly turn off the filament or close the valve of the gun.
2. Return the specimen holder back to the original zero position and take out the specimen holder, remove specimen from the holder, and re-insert the holder to the column to keep it clean (in some labs it is preferred to leave it out).
3. Retract the diffraction aperture, which may block the beam for the next user, and retract the objective aperture (in some labs it is preferred to leave it in for the next user).

4. Stay at certain lower magnification (such as 10,000×) as requested; dim the screen on console; put the viewing screen down and cover the viewing window.
5. Convert and transfer all the data acquired.
6. Check the instrument scheduler and if you are the last user, complete all assignments as including turning off the HT if it is required, and run cryocycle manually or by computer interface to warn up the ACD.
7. Log out or sign out the instrument.

References

[1] D.B. Williams, C.B. Carter. *Transmission Electron Microscopy: A Textbook for Materials Science*. Springer, New York, 2009.

[2] D. Shindo, T. Oikawa. *Analytical Electron Microscopy for Materials Science*. Springer Japan, Tokyo, 2002.

[3] J. Brink, M.B. Sherman, J. Berriman, W. Chiu. Evaluation of charging on macromolecules in electron cryomicroscopy. *Ultramicroscopy* **72**, 41–52 (1998).

[4] M. Haider, H. Rose, S. Uhlemann, E. Schwan, B. Kabius, K. Urban. A spherical-aberration-corrected 200 kV transmission electron microscope. *Ultramicroscopy* **75**, 53–60 (1998).

[5] N. Dellby, O.L. Krivanek, P.D. Nellist, P.E. Batson, A.R. Lupini. Progress in aberration-corrected scanning transmission electron microscopy. *J. Electron Microsc.* **50**, 177–185 (2001).

[6] M. Lentzen, B. Jahnen, C.L. Jia, A. Thust, K. Tillmann, K. Urban. High-resolution imaging with an aberration-corrected transmission electron microscope. *Ultramicroscopy* **92**, 233–242 (2002).

[7] M. Lentzen. Progress in aberration-corrected high-resolution transmission electron microscopy using hardware aberration correction. *Microsc. Microanal.* **12**, 191–205 (2006).

[8] D.J. Smith. Development of aberration-corrected electron microscopy. *Microsc. Microanal.* **14**, 2–15 (2006).

[9] K.W. Urban, C.L. Jia, L. Houben, M. Lentzen, S.B. Mi, K. Tillmann. Negative spherical aberration ultrahigh-resolution

imaging in corrected transmission electron microscopy. *Phil. Trans. Roy. Soc.* **A367**, 3735–3753 (2009).

[10] H. Jiang, J. Ruokolainen, N. Young, T. Oikawa, A.G. Nasibulin, A. Kirkland, E.I. Kauppinen. Performance and early applications of a versatile double aberration-corrected JEOL-2200FS FEG TEM/STEM at Aalto University. *Micron* **54**, 47–58 (2012).

[11] P.W. Hawkes. Aberration correction past and present. *Phil. Trans. Roy. Soc.* **A367**, 3637–3664 (2009).

[12] J. Zach. Chromatic correction: A revolution in electron microscopy? *Phil. Trans. Roy. Soc.* **A367**, 3699–3707 (2009).

[13] M. Haider, P. Hartel, H. Müller, S. Uhlemann, J. Zach. Information transfer in a TEM corrected for spherical and chromatic aberration. *Microsc. Microanal.* **16**, 393–408 (2010).

[14] F. Hosokawa, H. Sawada, Y. Kondo, K. Takayanagi, K. Suenaga. Development of C_s and C_c correctors for transmission electron microscopy. *Microscopy* **62**, 23–41 (2013).

[15] T. Sasaki, H. Sawada, F. Hosokawa, Y. Sato, K. Suenaga. Aberration-corrected STEM/TEM imaging at 15 kV. *Ultramicroscopy* **145**, 50–55 (2014).

[16] Z.P. Luo. Crystallography of SiC/$MgAl_2O_4$/Al interfaces in a pre-oxidized SiC reinforced SiC/Al composite. *Acta Mater.* **54**, 47–58 (2006).

CHAPTER 4

Electron Diffraction I

Electron diffraction is caused by the wave nature of the electrons. Since the wavelength of accelerated electrons is very short (Table 3.2), diffraction happens through interactions within the crystal lattices of the specimen. The following information can be learned through diffraction studies:

1. Determination of the specimen structure and crystallinity—the degree of structural order. If it is crystalline, electron diffraction can be used to determine structure type, symmetry, and lattice parameters. Atomic positions may also be determined through quantitative refinement.
2. Identification of constituent phases, phase transformations through *in situ* or *ex situ* studies, crystallographic orientation, any orientation relationship (OR) with surrounding phase, and estimation of transmission electron microscope (TEM) specimen thickness.
3. Align the sample orientation for imaging, such as in the diffraction-contrast imaging, and high-resolution imaging.

Therefore, electron diffraction is a basic skill in the TEM operation.

This chapter Diffraction I deals with the formation of electron diffraction, the concept of reciprocal space, and selected-area electron diffraction (SAED) or selected-area diffraction (SAD). SAED is formed by using a diffraction aperture to select an area and then switch to diffraction mode, so that the intermediate lens is focused on the first diffraction pattern on the back focal plane instead of the image plane (Section 3.1.5). Such a diffraction pattern is further magnified until it reaches on the final screen. Kikuchi diffraction, convergent-beam electron diffraction (CBED), and nano-beam electron diffraction (NBED) will be covered in Diffraction II in Volume 2.

4.1 Formation of Electron Diffraction

Similar to X-ray diffraction (XRD), the formation of electron diffraction can be described by Bragg's law. As shown in Fig. 4.1, at an incident angle θ, an electron beam enters a crystal lattice with parallel planes in a spacing of d. After scattering, the distance difference between two adjacent rays is $2d\sin\theta$, and when

$$2d\sin\theta = n\lambda \tag{4.1}$$

these two rays have the same phase, the intensity along this direction is enhanced (constructive interference). Here, λ is the wavelength and n is an integral number (1, 2, 3, …). This relationship is the Bragg's law. Note that in the event of electron scattering, the electron can be scattered at any direction. Only along certain directions as defined in Eq. 4.1, the intensities are strong so that they become reflection spots, whereas along other directions there are also electrons that contribute to the background of the diffraction pattern.

In electron diffraction, the wavelength λ is much shorter than the lattice spacing d, so the angle θ is very small. For example, λ = 0.0251 Å for 200 kV, and the Cu lattice constant a = 3.61 Å and thus the (200) lattice spacing d_{200} = 1.805 Å, θ = 0.397° according to Eq. 4.1. The angle θ is typically less than 2° on the diffraction patterns.

Note that the angle difference between reflected and incident beams is 2θ, that is, the diffracted beam is at 2θ angle with respect to the incident direct beam. Fig. 4.1 is drawn at the exact Bragg reflection conditions. As will be discussed later, if the incident beam is slightly off the exact angle θ, which is a defined value for a given system (since d and λ are defined), the diffraction still happens and the angle between the diffracted and incident beam remains the same 2θ.

In TEM, it is possible to select a small area for diffraction, so it is common to get an SAED pattern of single crystals, while XRD single-crystal pattern requires a large sample compared with the diffracted crystal in TEM [1]. As shown in Fig. 4.2(a), in a crystal lattice there are many crystalline planes, such as planes parallel to planes 1–5. On the SAEDP pattern (Fig. 4.2b), the reflections in row 1 are diffracted by planes parallel to plane 1 with a perpendicular relationship between them. Similarly, the diffraction rows 2–5 are produced by the planes parallel to planes 2–5, respectively.

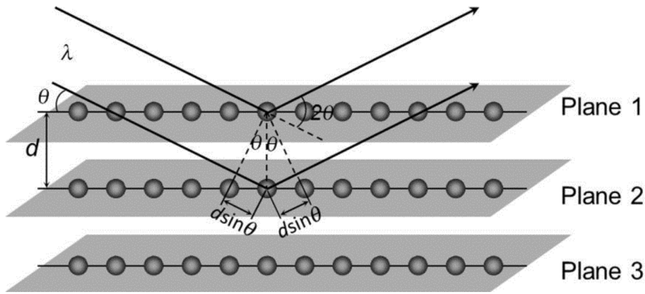

Fig. 4.1 Formation of diffraction pattern by Bragg's law in electron diffraction.

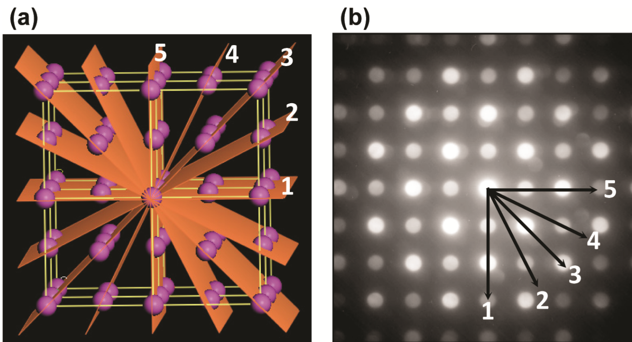

Fig. 4.2 Formation of single-crystal diffraction pattern. (a) Crystal lattice, with lattice planes marked with 1–5; (b) a single-crystal diffraction pattern.

Although the diffraction plane is perpendicular to the crystal lattice plane, however on the image, the diffraction pattern may be rotated with respect to the image (crystal lattice) by a magnetic rotation. Such a magnetic rotation may be corrected by the manufacture, or it is needed to calibrate using a known sample with defined shapes showing lattice directions (refer to Section 3.2.10). After the magnetic correction, one may draw the diffraction direction on an image and its perpendicular direction is the crystalline planes that diffracted the diffraction spots.

For each (*hkl*) reflection, it is possible to measure its lattice spacing d according to its distance r from the center direct beam. As shown in Fig. 4.3, when the crystal is at the Bragg diffraction orientation, we have the geometry relationship $2\theta = r/L$, where L is the camera length. According to Bragg's law, $2\sin\theta = \lambda/d$. Since θ is very small, θ approximately equals to $\sin\theta$, and thus

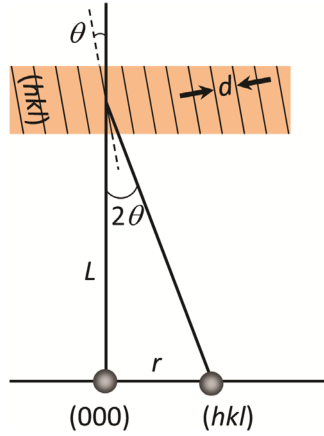

Fig. 4.3 Camera length L.

$$\frac{r}{L} = \frac{\lambda}{d}, \text{or } rd = L\lambda \tag{4.2}$$

Here, the product $L\lambda$ is camera constant, whose calibration is discussed in Section 3.2.9. If $L\lambda$ is calibrated for a given SAED pattern, the lattice distance d is thus

$$d = \frac{L\lambda}{r} \tag{4.3}$$

If the SAED pattern is acquired using CCD camera, the lattice spacing d may be given directly by the acquisition software.

4.2 Reciprocal Space

The electron diffraction pattern is an intersection of the reciprocal space lattice with the Ewald sphere, which is a sphere in the reciprocal space with radius of $1/\lambda$ (λ is the wavelength). Understanding the reciprocal space is very helpful to understand the electron diffraction.

The definition of the reciprocal space is shown in Fig. 4.4. For a given plane (hkl), the reciprocal vector **g** is along the normal direction of (hkl) plane, with length of

$$r = \frac{1}{d} \tag{4.4}$$

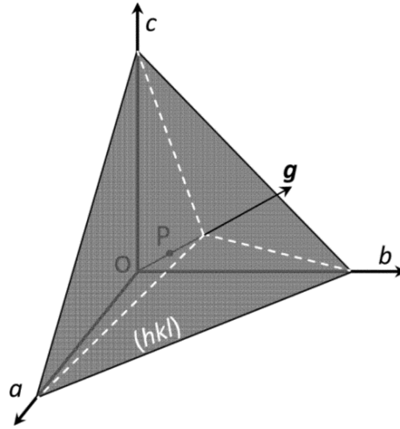

Fig. 4.4 Definition of reciprocal space.

As shown in Fig. 4.5, for a given 3D crystal lattice with a unit cell vectors **a**, **b**, and **c**, the reciprocal lattice vectors are defined as

$$\mathbf{a}^* = \frac{\mathbf{b}\times\mathbf{c}}{V_c},\quad \mathbf{b}^* = \frac{\mathbf{c}\times\mathbf{a}}{V_c},\quad \mathbf{c}^* = \frac{\mathbf{a}\times\mathbf{b}}{V_c} \tag{4.5}$$

Here, the font with bold indicates a vector, and V_c is the volume of the unit cell,

$$V_c = \mathbf{a}\cdot(\mathbf{b}\times\mathbf{c}) \tag{4.6}$$

Here, two kinds of vector operations are involved, as shown in Fig. 4.5(b):

1. $\mathbf{a}\times\mathbf{b}$, the result is still a vector, with direction perpendicular to the **a**–**b** plane from **a** to **b** by a right-hand rule. The magnitude is

$$|\mathbf{a}\times\mathbf{b}| = |\mathbf{a}|\cdot|\mathbf{b}|\cdot\sin\theta \tag{4.7}$$

2. $\mathbf{a}\cdot\mathbf{b}$, the result is a value only, with magnitude of

$$|\mathbf{a}\cdot\mathbf{b}| = |\mathbf{a}|\cdot|\mathbf{b}|\cdot\cos\theta \tag{4.8}$$

For an orthorhombic system, the angles between **a**, **b**, and **c** are all 90°, $|\mathbf{a}\times\mathbf{b}| = ab$, $|\mathbf{b}\times\mathbf{c}| = bc$, and $|\mathbf{c}\times\mathbf{a}| = ca$, and $V_c = abc$. Thus, Eq. 4.5 becomes

$$\mathbf{a}^* = \frac{1}{\mathbf{a}},\ \mathbf{b}^* = \frac{1}{\mathbf{b}},\ \mathbf{c}^* = \frac{1}{\mathbf{c}} \tag{4.9}$$

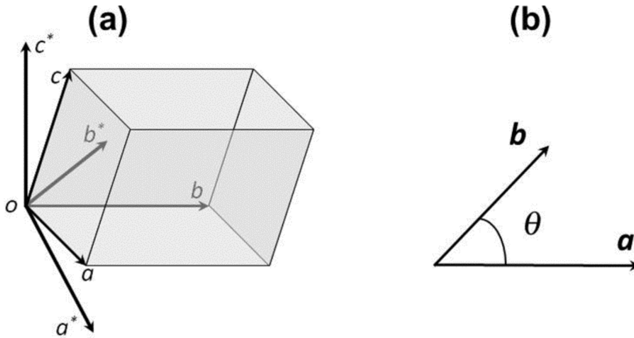

Fig. 4.5 (a) Reciprocal lattice vectors; (b) vector operations.

Here, the italic font indicates length, that is, $a = |\mathbf{a}|$.

From the definitions given in Eq. 4.5, it can be proven that the reciprocal space of a primitive cubic (PC) is still PC (Fig. 4.6a), whereas for a body-centered cubic (BCC) structure its reciprocal space is face-centered cubic (FCC) (Fig. 4.6b), and vice versa (Fig. 4.6c). For a hexagonal close-packed (HCP) structure, its reciprocal space is still hexagonal, the reciprocal vector $\mathbf{a}^*$ rotated 60° with respect to **a**, and the angle of $\mathbf{a}^*$ and $\mathbf{b}^*$ is 60°, rather than 120° between **a** and **b** (Fig. 4.6d).

Here, we give a proof about the FCC–BCC relationship between the real and reciprocal spaces. A BCC unit cell contains 2 atoms, so it is not a primitive cell. A primitive cell is selected, as shown in Fig. 4.7(a), which contains only 1 atom. Its basic vectors **a**, **b**, and **c** are outlined. Therefore, in the previous orthogonal coordinates,

$$\mathbf{a} = \frac{a}{2}(-\mathbf{i} + \mathbf{j} + \mathbf{k}) \tag{4.10a}$$

$$\mathbf{b} = \frac{a}{2}(\mathbf{i} - \mathbf{j} + \mathbf{k}) \tag{4.10b}$$

$$\mathbf{c} = \frac{a}{2}(\mathbf{i} + \mathbf{j} - \mathbf{k}) \tag{4.10c}$$

Therefore,

$$\mathbf{a}^* = \frac{\mathbf{b} \times \mathbf{c}}{V_c} = \frac{(a^2/4)(\mathbf{i} - \mathbf{j} + \mathbf{k}) \times (\mathbf{i} + \mathbf{j} - \mathbf{k})}{(a^3/2)} = \frac{1}{a}(\mathbf{j} + \mathbf{k}) \tag{4.11a}$$

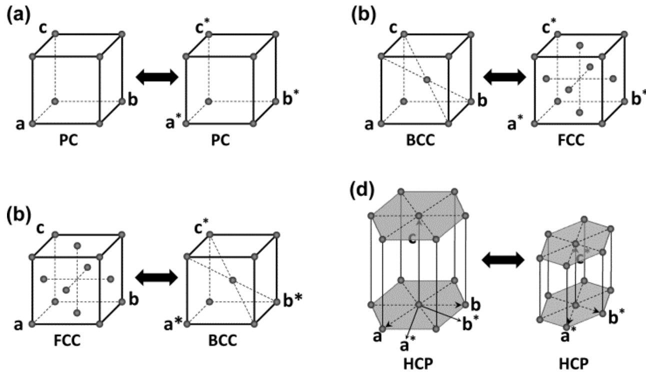

Fig. 4.6 Conversion to a reciprocal space (with basic vector of a^*, b^*, and c^*) from a real space (with basic vectors of a, b, and c) of PC (a), BCC (b), FCC (c), and HCP (d) lattices.

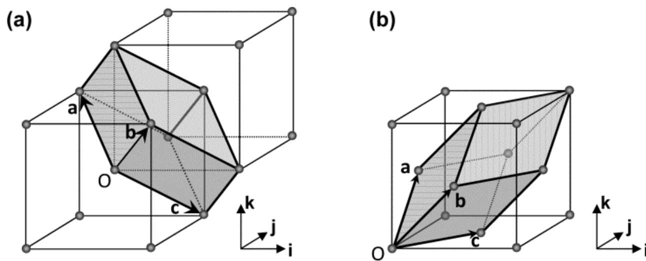

Fig. 4.7 Primitive cells of BCC (a) and FCC (b) systems.

Similarly,

$$\mathbf{b}^* = \frac{\mathbf{c}\times\mathbf{a}}{V_c} = \frac{(a^2/4)(\mathbf{i}+\mathbf{j}-\mathbf{k})(-\mathbf{i}+\mathbf{j}+\mathbf{k})}{(a^3/2)} = \frac{1}{a}(\mathbf{i}+\mathbf{k}) \qquad (4.11\text{b})$$

$$\mathbf{c}^* = \frac{\mathbf{a}\times\mathbf{b}}{V_c} = \frac{(a^2/4)(-\mathbf{i}+\mathbf{j}+\mathbf{k})(\mathbf{i}-\mathbf{j}+\mathbf{k})}{(a^3/2)} = \frac{1}{a}(\mathbf{i}+\mathbf{j}) \qquad (4.11\text{c})$$

A lattice with such $\mathbf{a}^*$, $\mathbf{b}^*$, and $\mathbf{c}^*$ basic vectors in Eq. 4.11 is FCC, that is, the reciprocal space of BCC is FCC.

In the same way to reduce the reciprocal space of the FCC lattice (Fig. 4.7b). A primitive unit cell is outlined, with basic vectors of

$$\mathbf{a} = \frac{a}{2}(\mathbf{j}+\mathbf{k}) \qquad (4.12\text{a})$$

$$\mathbf{b} = \frac{a}{2}(\mathbf{i} + \mathbf{k}) \tag{4.12b}$$

$$\mathbf{c} = \frac{a}{2}(\mathbf{i} + \mathbf{j}) \tag{4.12c}$$

Therefore,

$$\mathbf{a}^* = \frac{\mathbf{b} \times \mathbf{c}}{V_c} = \frac{(a^2/4)(\mathbf{i}+\mathbf{k})(\mathbf{i}+\mathbf{j})}{(a^3/2)} = \frac{1}{a}(-\mathbf{i}+\mathbf{j}+\mathbf{k}) \tag{4.13a}$$

$$\mathbf{b}^* = \frac{\mathbf{c} \times \mathbf{a}}{V_c} = \frac{(a^2/4)(\mathbf{i}+\mathbf{j})(\mathbf{j}+\mathbf{k})}{(a^3/2)} = \frac{1}{a}(\mathbf{i}-\mathbf{j}+\mathbf{k}) \tag{4.13b}$$

$$\mathbf{c}^* = \frac{\mathbf{a} \times \mathbf{b}}{V_c} = \frac{(a^2/4)(\mathbf{j}+\mathbf{k})(\mathbf{i}+\mathbf{k})}{(a^3/2)} = \frac{1}{a}(\mathbf{i}+\mathbf{j}-\mathbf{j}) \tag{4.13c}$$

A lattice with such **a***, **b***, and **c*** basic vectors is BCC, that is, the reciprocal space of FCC is BCC.

4.3 Indexing of Electron Diffraction Patterns

4.3.1 Indexing of Powder Patterns

The indexing of powder SAED patterns is analog to the indexing of XRD patterns, while the intensities may vary and some peaks may not show up on the SAED, since the area selected may contain limited number of crystals or limited orientations, keeping in mind that the powder pattern is in fact a mixture of many single-crystal patterns. If many crystals and orientations are collected, the powder pattern may contain polycrystalline rings, for example, the ring patterns from Al polycrystalline film (Figs. 3.26 and 3.27) are composed of SAED single-crystal patterns from many randomly oriented Al grains.

If limited crystals are selected to contribute to the pattern by using a small SAED aperture, the rings become discontinuous, and sometime only few spots appear on the ring. Fig. 4.8(a) is an example of SAED pattern from $Na_5V_{12}O_{32}$ nanowires [2]. The structure is monoclinic with space group of $P2_1/m$ (No. 11) and lattice parameters of a = 12.14 Å, b = 3.61Å, c = 7.32 Å, and β = 106.73°. Fig. 4.8(b) is the XRD pattern from this sample, which is well indexed as $Na_5V_{12}O_{32}$ phase (JCPDS

No. 24-1156). In order to index the pattern in Fig. 4.8(a), first of all, a set of rings are drawn on the pattern so that the rings cross the reflections. Set these drawn circles with ~70% transparency so that the original spots on the SAED are still visible. By measuring the spacing of each ring (refer to Section 3.2.9), the first ring spacing is 7.1 Å, which is close to the XRD pattern (001) peak with *d* = 7.010 Å. Note that in XRD the (001) is the strongest peak, while in SAED only few spots appear on this ring, since a limited area is selected. Compared with XRD peaks, other rings can be indexed similarly. Table 4.1 lists a comparison of the spacing of the rings with XRD peaks in Fig. 4.8(b). Basically they are consistent with each other.

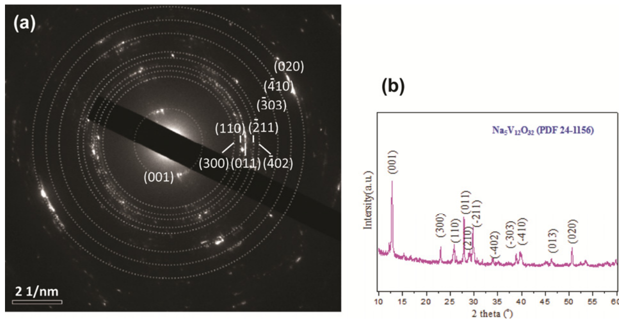

Fig. 4.8 Comparison of SAED and XRD patterns from $Na_5V_{12}O_{32}$. (a) Indexing of a powder SAED pattern; (b) indexing of XRD pattern.

Table 4.1 Indexing of diffraction rings of Fig. 4.8(a).

No.	SAED	XRD			*h*	*k*	*l*
	d (Å)	*d* (Å)	Theta	Intensity			
1	7.11	7.01	6.309	100	0	0	1
2	3.90	3.87	11.481	50	3	0	0
3	3.47	3.45	12.901	70	1	1	0
4	3.23	3.22	13.84	90	0	1	1
5	2.94	2.988	14.939	50	–2	1	1
6	2.76	2.64	16.964	30	–4	0	2
7	2.29	2.318	19.409	50	–3	0	3
8	2.12	2.269	19.845	30	–4	1	0
9	1.83	1.807	25.231	80	0	2	0

It should be mentioned that XRD can routinely provide accurate peak positions and intensities, while the routine SAED measurements may contain relatively large errors. For more accurate measurement, a calibration of the camera length should be done using polycrystalline Al foils, including the camera length calibration and any possible *y*/*x* vertical/horizontal distortion [3]. More details will be given in Volume 2.

4.3.2 Indexing of Single-Crystal Diffraction Patterns

A single SAED pattern is contributed by a single crystal lattice. As mentioned earlier, a crystal lattice is composed of many crystalline planes. The common axis of these planes, [*UVW*], is called the zone axis, as shown in Fig. 4.9. A set of parallel planes give rise to a row of reflections, such as reflection $\mathbf{g}_1$ is diffracted by planes parallel to plane 1, and $\mathbf{g}_2$ by planes parallel to plane 2. Here, $\mathbf{g}_1$ and $\mathbf{g}_2$ are vectors in the reciprocal space.

Since each reflection vector $\mathbf{g}_{hkl}$ is perpendicular to the (*hkl*) plane, which diffracts the beam to form it, while the [*UVW*] zone axis is in all (*hkl*) planes, $\mathbf{g}_{hkl}$ is perpendicular to the [*UVW*] zone axis, that is,

$$\mathbf{g}_{hkl}.[UVW]=0 \tag{4.14}$$

or

$$hU + kV + lW = 0 \tag{4.15}$$

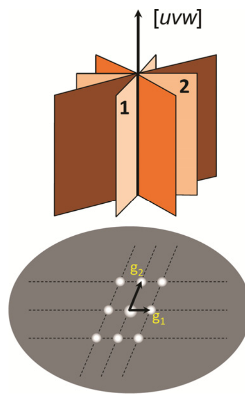

***Fig. 4.9** Zone axis [UVW] of a crystal lattice (upper) and diffraction pattern (bottom).*

Accordingly, if any two vectors that are not in a line are known, the zone axis can be obtained by

$$[UVW] = \mathbf{g}_1 \times \mathbf{g}_2 = \begin{vmatrix} i & j & k \\ h_1 & k_1 & l_1 \\ h_2 & k_2 & l_2 \end{vmatrix} = \begin{vmatrix} k_1 & l_1 \\ k_2 & l_2 \end{vmatrix} i - \begin{vmatrix} h_1 & l_1 \\ h_2 & l_2 \end{vmatrix} j + \begin{vmatrix} h_1 & k_1 \\ h_2 & k_2 \end{vmatrix} k$$

$$= (k_1 l_2 - l_1 k_2) i - (h_1 l_2 - l_1 h_2) j + (h_1 k_2 - k_1 h_2) k \tag{4.16}$$

and therefore,

$$U = (k_1 l_2 - l_1 k_2), \quad V = -(h_1 l_2 - l_1 h_2), \; W = (h_1 k_2 - k_1 h_2) \tag{4.17}$$

As shown in Fig. 4.10(a), a general way to index a single SAED pattern is descripted as follows:

1. Measure the lengths of two shortest reciprocal vectors r_1 (the shortest one) and r_2 (the shortest if available, or the second shortest one) along two different line directions, and measure the angle α between these two vectors.
2. Calculate the ratio of r_2/r_1 (≥ 1) and the greatest lattice spacing d_1 using $d_1 = (L\lambda)/r_1$, or using CCD acquisition software.
3. If the structure is known, compute all possible zone axis patterns in order of the ratio of r_2/r_1 and find out the indexes of $(h_1 k_1 l_1)$ and $(h_2 k_2 l_2)$.

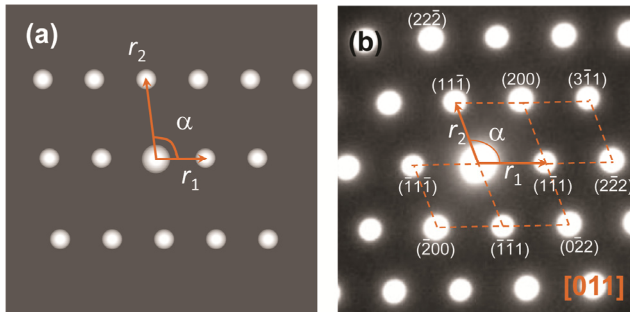

***Fig. 4.10** (a) Indexing SAED pattern using two shortest vectors r_1 and r_2; (b) indexing of an SAED pattern (FCC structure along [011] zone axis).*

Once two reflections are indexed, the entire pattern can be indexed, as shown in Fig. 4.10(b). Based on the vector summation or subtraction, all spots on the pattern are indexed. The author of this book has written a program that can compute the indexing table (refer to the appendices).

For an unknown structure, at least two different zone axis patterns should be obtained by tilting (with tilting angle known), so that a unit cell in the reciprocal space can be constructed [4, 5]. Normally, from the geometry of several major zone axis patterns, it is possible to deduce possible structures. For example, a square pattern possibly originates from cubic [001] or tetragonal [001] zone axes, and a hexagonal pattern, from hexagonal [0001] or cubic [111] zone axes. If all patterns can be indexed using a proposed structural model, the structural model is correct.

4.3.3 *Indexing of Compound Patterns: Twins*

Twins are often found in the TEM samples, especially in deformed samples as twinning is one of the fundamental deformation mechanisms.

A highly twinned microstructure in a 316L stainless steel (FCC structure) is presented in Fig. 4.11 [6]. In the bright-field (BF) image in Fig. 4.11(a), the twins are not very clear because of the presence of high-density dislocations. However, in the central dark-field (CDF) image formed by a reflection from the twin, parallel twin plates are clearly revealed (how to get CDF image will be discussed in Chapter 5). A typical twinned SAED pattern is shown in Fig. 4.11(c), which is obtained from an area covering both the matrix and the twins. A close measurement shows that extra spots appear at the 1/3 position along a row of spots. Note that close spaced spot row direction is perpendicular to the twinning interface, since there is no magnetic rotation between them by the TEM used. However, using a small SAED aperture to select areas from the matrix or twin only, single SAED patterns of the FCC lattices can be obtained, as shown in Fig. 4.11(e) and (f), respectively. Superimposing these two patterns would result a pattern with geometry similar to the twinned pattern in Fig. 4.11(c). In order to the keep their common plane index $(11\bar{1})$ the same, one zone axis is indexed as $[011]_M$, and the other one is indexed as $[0\bar{1}\bar{1}]_T$. Here, the subscripts M and T stand for

matrix and twin, respectively. Therefore, the twined pattern is indexed, as shown in Fig. 4.11(g). A magnified part is schematically shown in Fig. 4.11(h). The indexing shows that along the common twinning plane $(11\bar{1})$, the reflections from the matrix and twin are symmetrical, consistent with their real space lattice, which are symmetrical to their {111} twinning plane, as shown in Fig. 4.11(d). Therefore, in the TEM experiment, if a complex pattern is observed, try to use a smaller SAED aperture to find the origin of the complex pattern.

In the stainless steel sample, two twin variants can be found, as shown in Fig. 4.12. Their CDF images of twins 1 and 2 are shown in Fig. 4.12(b) and (c), respectively. A pattern from both twins 1 and 2 is shown in Fig. 4.12(d), which can be indexed by two steps: twin 1 and twin 2 separately, as shown in Fig. 4.12(e) and (f), respectively.

In HCP system, the twins can also be found, as shown in a severely deformed Ti–6Al–4V alloy in Fig. 4.13 [7]. Thin twinning plates are clearly shown in the CDF image in Fig. 4.13(b). From the indexing, the twinning plane is $(\bar{1}011)$. Similar to the FCC case, the reflections from the matrix and twin are symmetrical to their common twinning plane $(\bar{1}011)$.

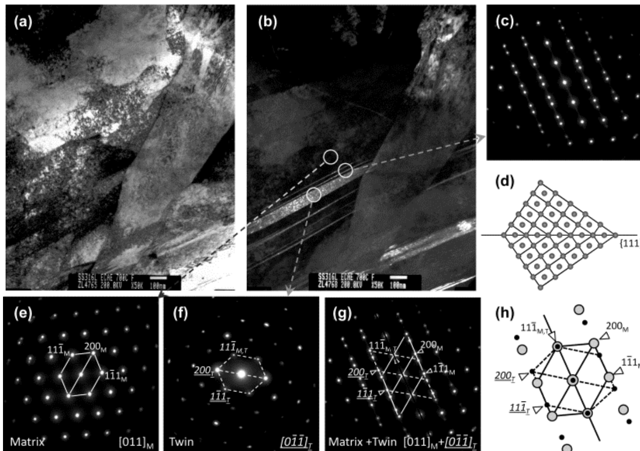

Fig. 4.11 Twinning microstructure of deformed stainless steel. (a) BF; (b) CDF, with SAED patterns from circled areas showing in (c, e, f); (c) SAED of twins; (d) structural model of twins; (e) SAED from the matrix; (f) SAED from the twin; (g) indexing of twins; (h) schematic indexing.

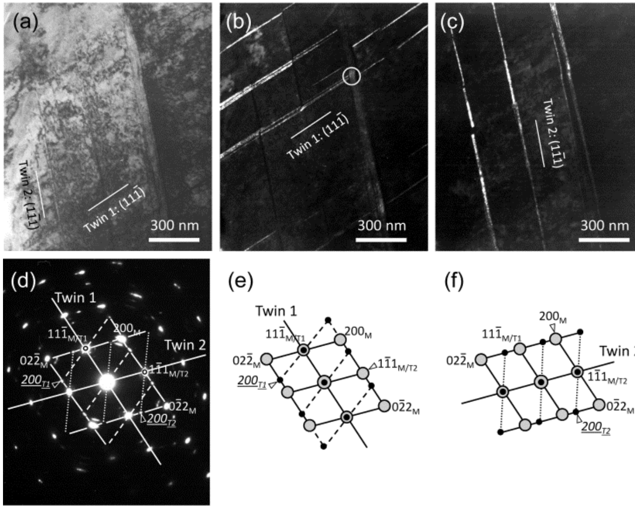

Fig. 4.12 Twinning microstructure of deformed stainless steel. (a) BF; (b) CDF showing twin 1; (c) CDF showing twin 2; (d) SAED showing two twinning variants; (e) indexing of twin 1; (f) indexing of twin 2.

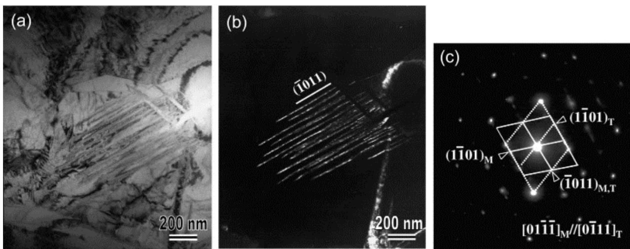

Fig. 4.13 Twining in a severely deformed Ti–6Al–4V with HCP structure. (a) BF; (b) CDF; (c) SAED pattern.

In addition to the twins with mirror symmetry to their common twining plane, there is another type of 90° or near 90° rotation twins, which are common in perovskite pseudo-cubic structures, or long-period structure. An example of a colossal magnetoresistive manganite (CMR) $Nd_{0.5}Sr_{0.5}MnO_3$ is shown in Fig. 4.14 [8]. At room temperature, its structure is orthorhombic, with space group of *Pnma* (Fig. 4.14d). In the image of Fig. 4.14(a), although twining boundaries (TBs) are visible, SAED patterns across the TBs are very similar, since it is not easy to find

the slight differences of d_{200} and d_{002}. However, at a low temperature, the mixed Mn^{3+} and Mn^{4+} are separated to form charge ordering (CO), so the structure is transformed to a monoclinic structure with space group of $P2_1/m$ (Fig. 4.14e). Because of the $2a \times b \times c$ ordering, the lattice spacing along (200) direction is doubled, so that it becomes very clear to see the 90° rotation across the TBs, as shown in Fig. 4.14(b) and (c).

Such near 90° rotation twins are also often found in long-period structures [9, 10]. An example of a Ni–Mn–Sn alloy is shown in Fig. 4.15 [10]. The martensite has a structure of 4*O*, with 4 layers stacked along its **c** direction (Fig. 4.15a). Therefore in the SAED pattern, weak spots with ¼ spacing appear between the fundamental reflections, as shown in Fig. 4.15(b). Along near 90° direction, there is another row with ¼ spacing, forming near 90° rotation twins.

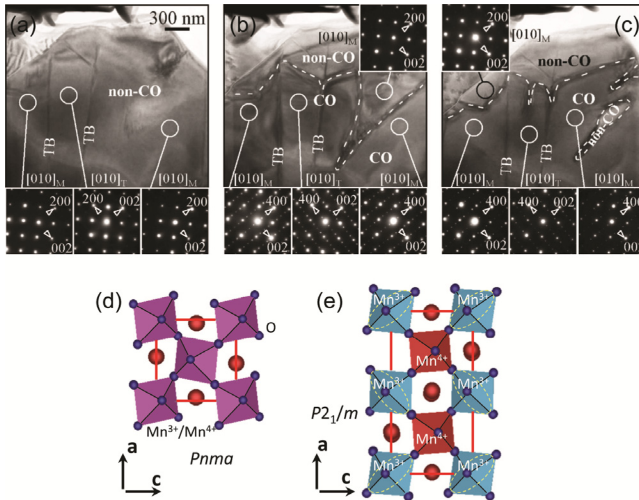

Fig. 4.14 90° rotation twins in CMR $Nd_{0.5}Sr_{0.5}MnO_3$. (a) BF at room temperature without CO; (b) BF at a low temperature of –179 °C with CO; (c) second cooling down to –179 °C after heating; (d) structure at room temperature without CO; (e) charge ordered structure at the low temperature.

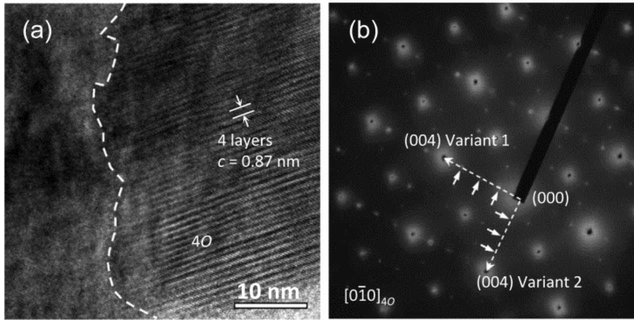

Fig. 4.15 (a) High-resolution TEM image showing 4-layer martensite; (b) SAED pattern from a large area showing two martensite variants.

4.3.4 Indexing of Compound Patterns: Multiple Phases

Electron diffraction in TEM can be used to identify different phases. In a B_4C/Al composite, as shown in Fig. 4.16, there are B_4C, Al matrix, and reactant AlB_{10} phases [11]. AlB_{10} is orthorhombic, which was formed by the reaction of B_4C and Al. In the BF image, Al matrix appears as dark contrast with dislocations, while B_4C and AlB_{10} appear as bright contrast without dislocation lines. The SAED patterns in Fig. 4.16(b) and (c) contain compound patterns. As mentioned early dealing with twins (Fig. 4.11), a good way to identify them is to use a small SAED aperture to get single-crystal SAED patterns from each area, as shown in Fig. 4.16(d)–(f), which are indexed as [031] AlB_{10}, [011] Al, and [001] AlB_{10}, respectively. Therefore, the SAED pattern in Fig. 4.16(b) can be indexed as the combination of Fig. 4.16(d) and (e), and pattern Fig. 4.16(c) as a combination of Fig. 4.16(e) and (f). Note that there are some extra reflections in Fig. 4.16(b) that are not indexed, which are formed by double diffraction that will be discussed next. If two phases have one or more planes parallel to each other, an OR can be found between them. In Fig. 4.16, no OR exists.

ORs are often found from the SAED patterns. In the SAED pattern in Fig. 4.17, the BCC is along [111] zone axis and the FCC is along [011]. It is found that $(\bar{1}01)_{BCC}$ is parallel to $(11\bar{1})_{FCC}$, that is, the line across (000) and $(\bar{1}01)_{BCC}$ is parallel to the line across (000) and $(11\bar{1})_{FCC}$. Therefore, the OR is expressed as

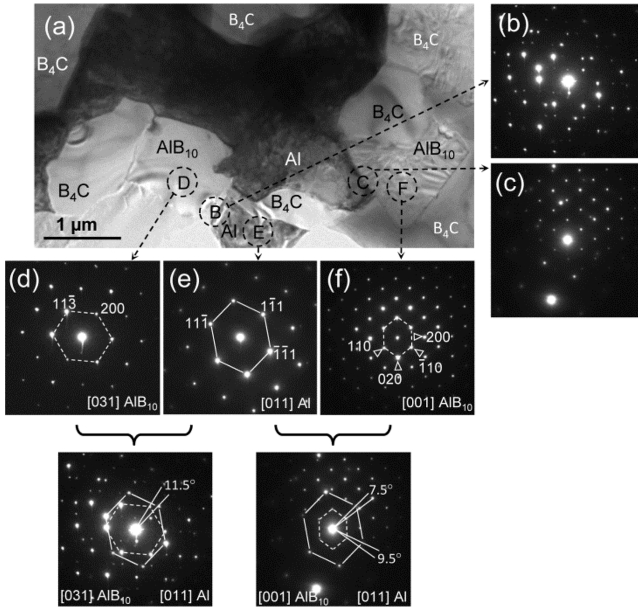

Fig. 4.16 Microstructure of B_4C/Al composite. (a) BF, with SAED patterns from the circled areas showing in (b–f).

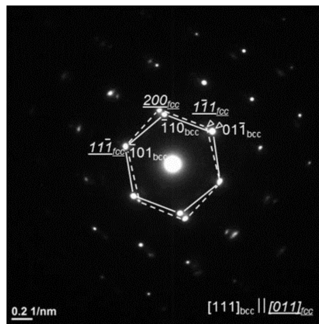

Fig. 4.17 SAED pattern from FCC and BCC phases showing an OR.

$$(\bar{1}01)_{BCC} \parallel (11\bar{1})_{FCC}$$

$$[111]_{BCC} \parallel [011]_{FCC} \tag{4.18}$$

This is the K–S OR between martensite and austenite.

Another example of hexagonal SiC and cubic $MgAl_2O_4$ spinel phase (FCC with a = 0.8075 nm) is shown in Fig. 4.18 [12]. In order to determine an OR, the intensities of all reflections must be symmetrical to the central direct beam (000), so that the pattern is almost along their zone axes within errors typically less than ±2° [13]. From the indexing in Fig. 4.18(b), the close-packed plane $(1\bar{1}1)$ of the spinel phase $MgAl_2O_4$ is parallel to the close-packed basal plane (0001) of the SiC phase, and thus their OR is determined as follows:

$$(0001)_{SiC} \parallel (1\bar{1}1)_{MgAl_2O_4}$$

$$[2\bar{1}\bar{1}0]_{SiC} \parallel [011]_{MgAl_2O_4} \tag{4.19}$$

According to this OR, stereographic projections of plane indexes of these two phases along $(0001)_{SiC}$ and $(1\bar{1}1)_{MgAl_2O_4}$ are superimposed, as shown in Fig. 4.18(c). Therefore, more parallel planes are found with this OR, such as $(2\bar{1}\bar{1}0)_{SiC} \parallel (011)_{MgAl_2O_4}$ and $(10\bar{1}0)_{SiC} \parallel (\bar{1}12)_{MgAl_2O_4}$.

4.3.5 Indexing of Compound Patterns: Double Diffraction

Double diffraction happens with the presence of multiple phases along interfaces, where the diffracted beam of the upper crystal, if it is strong, acts as a transmitted beam (direct beam) of the bottom crystal. In such a way, extra spots may be produced.

As illustrated in Fig. 4.19(a), if only the direct beam is diffracted by two crystals without double diffraction, the diffraction pattern will be two imposed regular SAED patterns (only bottom crystal pattern is

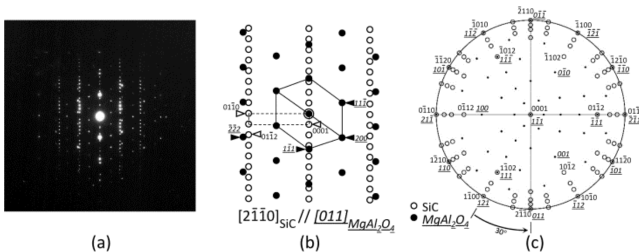

Fig. 4.18 (a) SAED pattern from SiC along its a-axis and $MgAl_2O_4$ spinel phase along [011] zone axis; (b) indexing of the SAED pattern; (c) stereographic projection showing the OR.

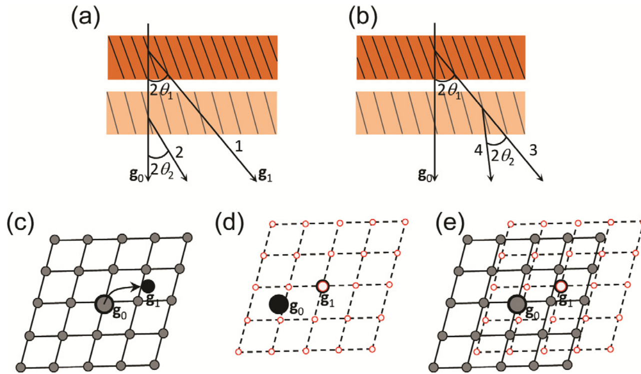

Fig. 4.19 ***(a) Two crystals without occurrence of double diffraction; (b) with double diffraction; (c) schematic bottom-crystal SAED from (a) with a strong reflection g_1 from the top crystal; (d) schematic extra SAED pattern from bottom crystal resulted from double diffraction; (e) superimposed of SAED patterns from the bottom crystal.***

shown in Fig. 4.19c, with a spot $\mathbf{g}_1$ from the top crystal). However, if the diffraction ray 1 from the upper crystal is strong enough, it may be diffracted by the lower crystal, as shown in Fig. 4.19(b). In this case, what happens to the lower crystal is that the incident beam is inclined instead of along the optical axis. This is the same effect of beam tilt, which causes the pattern transition and also intensity redistribution slightly, but the geometry remains the same if it is not at very large angle. Therefore, the entire pattern of the lower crystal moves from its (000) to the $\mathbf{g}_1$ position, as indicated by an arrow in Fig. 4.19(c). The pattern caused by the double diffraction is shown in Fig. 4.19(d). This pattern brings extra reflections to the original pattern, as shown in Fig. 4.19(e).

Fig. 4.20(a) shows a high-resolution TEM (HRTEM) image of the Al/B_4C interface [11]. Fringes with wider lattice spacing than that of B_4C are visible at the interface, and the fast Fourier transformation (FFT) pattern from the framed area, as shown in the inset, contains extra reflections as indicated by arrowheads. The Al matrix is at the orientation between [235] and [112] zone axes (the angle between [112] and [235] is 6.6°), so that its {111} reflections are strongly excited, as shown in Fig. 4.20(b). In the compound pattern in Fig. 4.20(d), the B_4C is at the [211] zone axis, while it shows no OR with the Al matrix. However, extra reflections are observed, as indicated by arrowheads. Such extra spots

are caused by double diffraction as follows. If the Al crystal is located above B_4C (Fig. 4.20c), its strong {111} reflections acts as the incident beam to the B_4C phase to produce these extra reflections. As demonstrated in Fig. 4.20(f), if $(11\bar{1})_{Al}$ acts as the incident beam of B_4C, $(000)_{B_4C}$ would move to $(11\bar{1})_{Al}$ position causing a set of extra weak spots. Similarly, the occurrence of $(\bar{1}\bar{1}1)_{Al}$ as incident beam to B_4C would move $(000)_{B_4C}$ to $(\bar{1}\bar{1}1)_{Al}$ position causing another set of extra weak spots (Fig. 4.20g). If both $(11\bar{1})_{Al}$ and $(\bar{1}\bar{1}1)_{Al}$ act as the incident beams, two sets of extra spots are generated, with the geometry of double spots as indicated by arrowheads in Fig. 4.20(h). Therefore, the fringes with anomalous wide spacing are not produced from a secondary phase, but formed by the interference of two overlapped crystals by the double diffraction phenomenon.

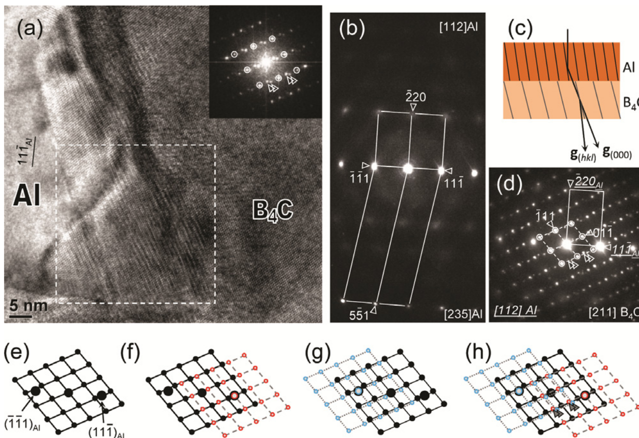

***Fig. 4.20** Double diffraction at Al–B_4C interface. (a) HRTEM image along the interface, with inserted FFT from the framed area; (b) SAED pattern from Al; (c) a model for the double diffraction; (d) SAED pattern from the interface showing extra spots as indicated; (e) $[211]_{B_4C}$ zone axis pattern and two strong spots from Al before the occurrence of double diffraction; (f) moving $(000)_{B_4C}$ to $(11\bar{1})_{Al}$ position causing a set of extra weak spots; (g) moving $(000)_{B_4C}$ to $(\bar{1}\bar{1}1)_{Al}$ position causing another set of extra weak spots; (h) moving $(000)_{B_4C}$ to both $(\bar{1}\bar{1}1)_{Al}$ and $(\bar{1}\bar{1}1)_{Al}$ position causing two sets of extra weak spots, with double spots as indicated.*

4.4 Experimental Procedures

To start with electron diffraction, first of all focus the pattern well. This can be done using overfocusing C2 (turn "Brightness" knob CW) so that the spots become weak, then use "Diffraction Focus" knob to focus the center spot. Correct any astigmatism to make the spots round, if needed.

Very occasionally the SAED pattern is already symmetric at zero tilt, that is, all spot intensities are symmetrical to the central (000) spot and no tilt is needed. If they are not symmetric, tilting is needed. The sample tilting directions are different for different TEMs.

On a JEOL 2010 TEM, the sample tilt is controlled by two foot pedals, as shown in Fig. 4.21. The arrows indicate the diffraction intensity moving directions. For example, press X-tilt + button increasing the X-tilt angle, while on the screen the diffraction spots moving toward the right side. With these four buttons, the diffraction spots can move along any direction. On an FEI Tecnai, the sample tilt is controlled by two pairs of key controls, as shown in Fig. 4.22. The moving directions are indicated by arrows. Before the diffraction experiment, the user should identify the moving directions on the TEM by using a large-size grain (single crystal).

During the sample tilt, the specimen may shift. It is important to set the specimen height at the eucentric position so that it does not move much for X-tilt, while it may move for the Y-tilt. It is often needed to check back in the image mode to ensure the same location. One may largely underfocus the pattern using "Diffraction Focus" knob to see an image in the diffraction spot to keep track of the location.

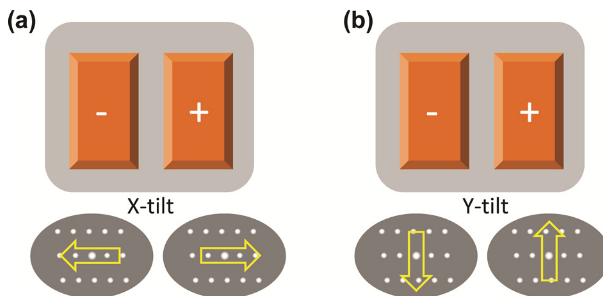

Fig. 4.21 SAED spot intensity moving directions by foot pedal controls on a JEOL 2010 TEM. (a) X-tilt control; (b) Y-tilt control. Arrows indicate the moving directions of the spot intensities on the SAED pattern.

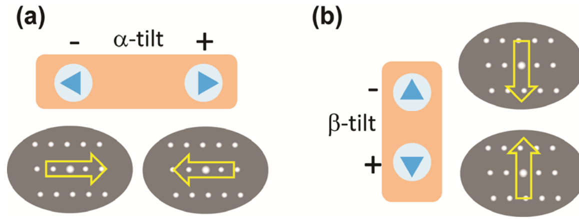

Fig. 4.22 SAED spot intensity moving directions on an FEI Tecnai. (a) α-tilt control; (b) β-tilt control. Arrows indicate the moving directions of the spot intensities on the SAED pattern.

If the stage is tilted from coordinates (X_1, Y_1) to another (X_2, Y_2), the sample tilting angle α is

$$\cos\alpha = \cos(X_2 - X_1) \cdot \cos(Y_2 - Y_1) \tag{4.20}$$

For a single-tilt holder, $Y_1 = Y_2 = 0$, and thus $\alpha = X_2 - X_1$.

An example for tilting experiment is shown in Fig. 4.23. The sample has an FCC structure. It is very off its [011] zone axis in Fig. 4.23(a). The intensities mainly distribute at the lower-left side, as marked with a circle, and the circle center is approximately the zone axis center, as marked with a "+" symbol. If the JEOL 2010 TEM is used (refer to Fig. 4.21), in order to move the zone axis to the center, one needs to apply X+ (moves to right) and then Y+ (moves up). Of course, one may press Y+ first, then X+, or even simultaneously by a skilled operator. However, if it is on the Tecnai TEM (refer to Fig. 4.22), one needs to press "α-tilt –" and "β-tilt +". The aligned SAED pattern is shown in Fig. 4.23(b), where the intensities are almost symmetric to the center (000).

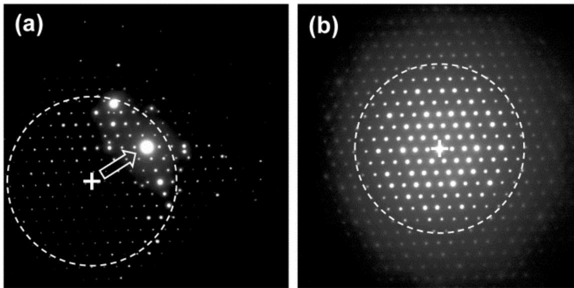

Fig. 4.23 (a) The SAED pattern is off its zone axis (marked with a cross which is the center of the circle of the intensity distribution); (b) After sample tilt, the pattern is along its zone axis (taken from the same area).

A technical trick for diffraction experiment is to use beam shift. If the sample zone axis is not along its optical axis, one may tilt the beam so that the beam can coincide with the zone axis to get an intensity-symmetric pattern. Following these steps for beam tilt:

1. Switch to a dark-field (DF) mode (the beam tilt will mess up the alignments, so keep the bright-field [BF] mode in a good shape for imaging since BF and DF are independent in alignments).
2. Tilt the beam toward getting more symmetrical intensities.
3. During the beam tilt, the entire pattern moves; thus, use Projector Lens Shift to move the pattern toward the screen center.
4. Repeat steps 2 and 3 until a satisfactory pattern is obtained. Record the pattern.
5. Reset the DF setting as needed, and switch back to BF mode.

To an experienced TEM user, the beam tilt is particularly useful, since it can quickly result a very symmetric pattern without mechanical movement by controlling the sample angles. However, bear in mind that the beam tilt messes up the alignments, so it can be done only in the DF mode, and remember to reset it and return back to BF mode.

4.5 Simulation of Diffraction Patterns

If the sample is very thin, the electron diffraction can be treated by kinematic scattering theory without considering multiple scattering events. In this case, the structure factor of (*hkl*) is

$$F_{hkl} = \sum_i f_i e^{2\pi i(hx_i + ky_i + lz_i)} \tag{4.21}$$

and thus

$$F_{hkl}^2 = [\sum_i f_i cos 2\pi(hx_i + ky_i + lz_i)]^2 + [\sum_i f_i sin 2\pi(hx_i + ky_i + lz_i)]^2 \tag{4.22}$$

Here, f_i is the atomic scattering factor of the *i*th atom at (x_i, y_i, z_i) coordinate, which is related to the type of elements and the scattering angle

θ [14–16]. (*hkl*) is the crystalline plane. The diffraction intensity I is proportional to F_{hkl}^2,

$$I \propto F_{hkl}^2 \tag{4.23}$$

According to Eq. 4.22, one may obtain the following reflection conditions:

1. PC: all reflections appear.
2. BCC:
   $F_{hkl} = 2f$ when $h + k + l = 2n$.
   $F_{hkl} = 0$ when $h + k + l = 2n + 1$.
3. FCC:
   $F_{hkl} = 4f$ when h, k, and l are all even or all odd
   $(h + k = 2n, k + l = 2n,$ and $l + h = 2n)$.
   $F_{hkl} = 0$ when h, k, and l are mixed with even and odd.
4. C-Centering: $F_{hkl} \neq 0$ when $h + k = 2n$, while for other (*hkl*), $F_{hkl} = 0$.

Here, n is an integer. When $F_{hkl} = 0$, the reflection does not appear, which is a systematic absence.

However, if the sample is thick, the kinematic scattering theory is no longer valid, but dynamic scattering theory should be considered to take into account of multiple scattering. In this dynamic approach, it is needed to know the atomic positions of the crystal, zone axis, sample thickness and centering, and some microscope parameters. Some commercial programs can conduct such simulations.

Fig. 4.24 presents simulated SAED patterns of $YBa_2Cu_3O_y$ orthorhombic crystal along [100] zone axis at different thicknesses. For a thin crystal with thickness t = 2 nm, there are only few reflections near the (000), as shown in Fig. 4.24(a). The (010) is weak, and the (001) is even not visible. As the thickness increases, the intensities change largely, as shown in Fig. 4.24(b)–(d).

The amplitude and phase changes with thickness t of (000), (010), and (001) three beams are shown in Fig. 4.25(a) and (b), respectively. These curves vary largely with t. In order to interpret an SAED pattern, dynamic simulation at appropriate thickness should be conducted.

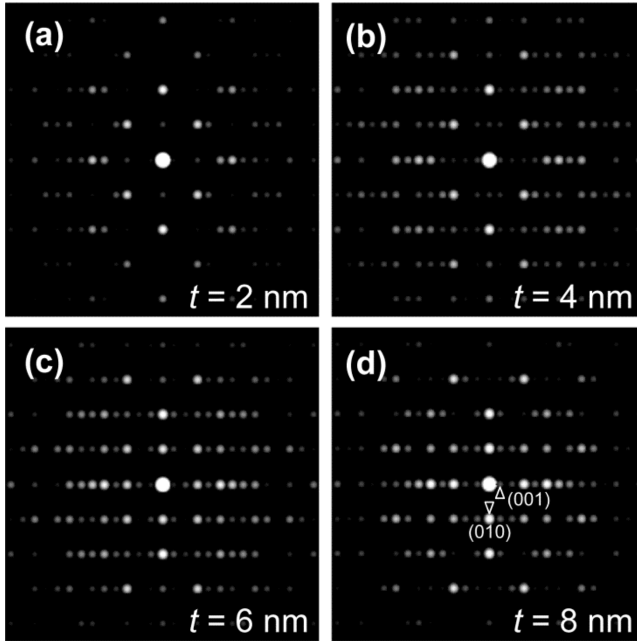

Fig. 4.24 Simulated [100] zone axis diffraction patterns of $YBa_2Cu_3O_y$ crystal at different thicknesses.

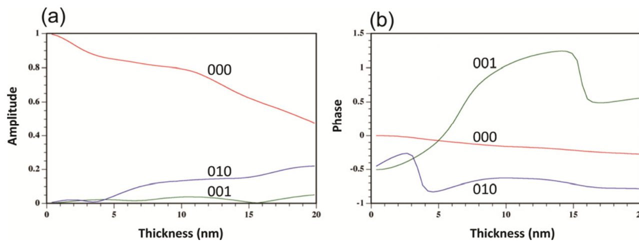

Fig. 4.25 Simulated amplitude (a) and phase (b) of $YBa_2Cu_3O_y$ crystal as a function of thickness.

References

[1] D.W. Deng, K.H. Kuo, Z.P. Luo, D.J. Miller, M.J. Kramer, K.W. Dennis. Crystal structure of the hexagonal Zn_3MgY phase. *J. Alloys Compd.* **373**, 156–160 (2004).

[2] Yunhe Cao, D. Fang, Chang Wang, Licheng Li, Weilin Xu, Z. Luo, Xiaoqing Liu, Chuanxi Xiong, Suqin Liu. Novel aligned

sodium vanadate nanowire arrays for high-performance lithium-ion battery electrodes. *RSC Adv.* **5**, 42955–42960 (2015).

[3] Z. Luo, Y. Vasquez, J.F. Bondi, and R.E. Schaak. Pawley and Rietveld refinements using electron diffraction from $L1_2$-type intermetallic Au_3Fe_{1-x} nanocrystals during their *in-situ* order-disorder transition. *Ultramicroscopy* **111**, 1295–1304 (2011).

[4] X. Zou, A. Hovmöller, S. Hovmöller. TRICE—A program for reconstructing 3D reciprocal space and determining unit-cell parameters. *Ultramicroscopy* **98**, 187–193 (2004).

[5] X.Z. Li. Computer programs for unit-cell determination in electron diffraction experiments. *Ultramicroscopy* **102**, 267–277 (2005).

[6] G.G. Yapici, I. Karaman, Z.P. Luo, J. J. Maier, Y.I. Chumlyakov. Microstructural refinement and deformation twinning during severe plastic deformation of 316L stainless steel at high temperatures. *J. Mater. Res.* **19**, 2268–2278 (2004).

[7] G.G. Yapici, I. Karaman, Z.-P. Luo. Mechanical twinning and texture evolution in severely deformed Ti-6Al-4V at high temperatures. *Acta Mater.* **54**, 3755–3771 (2006).

[8] Z.P. Luo, D.J. Miller, J.F. Mitchell. Structure and charge ordering behavior of the colossal magnetoresistive manganite $Nd_{0.5}Sr_{0.5}MnO_3$. *J. Appl. Phys.* **105**, 07D528 (2009) (3 pp).

[9] J. Pons, V.A. Chernenko, R. Santamarta, E. Cesari. Crystal structure of martensitic phases in Ni-Mn-Ga shape memory alloys. *Acta Mater.* **48**, 3027–3038 (2000).

[10] H. Zheng, W. Wang, S. Xue, Q. Zhai, J. Frenzel, Z. Luo. Composition-dependent crystal structure and martensitic transformation in Heusler Ni-Mn-Sn alloys. *Acta Mater.* **61**, 4648–4656 (2013).

[11] Z. Luo, Y. Song, S. Zhang, D.J. Miller. Interfacial microstructure in a B_4C/Al composite fabricated by pressureless infiltration. *Metall. Mater. Trans. A* **43**, 281–293 (2012).

[12] Z.P. Luo. Crystallography of SiC/$MgAl_2O_4$/Al interfaces in a pre-oxidized SiC reinforced SiC/Al composite. *Acta Mater.* **54**, 47–58 (2006).

[13] K.H. Kuo, C.L. Jia. Crystallography of $M_{23}C_6$ and M_6C precipitated in a low alloy steel. *Acta Metall.* **33**, 991–996 (1985).

[14] P.A. Doyle, P.S. Turner. Relativistic Hartree-Fock X-ray and electron scattering factors. *Acta Cryst.* **A24**, 390–397 (1968).

[15] A.G. Fox, M.A. O'Keefe, M.A. Tabbernor. Relativistic Hartree-Fock X-ray and electron atomic scattering factors at high angles. *Acta Cryst.* **A45**, 786–793 (1989).

[16] L.-M. Peng, G. Ren, S.L. Dudarev, M.J. Whelan. Robust parameterization of elastic and absorptive electron atomic scattering factors. *Acta Cryst.* **A52**, 257–276 (1996).

CHAPTER 5

Imaging I

Imaging is used to document the structure of investigated samples, including size, shape, location, and distribution. Typical examples are deposited sample objects on support films, sample internal grains, deformation microstructure and defects (twins, stacking faults, and dislocations), precipitates, and reactants. Depending on the sample type and information needed, different imaging techniques have been developed. Although taking images seems to be an easy job, especially with the aid of charge-coupled device (CCD) camera, how to take an image for a special purpose requires understanding of the imaging principles.

For accurate size measurement, the magnification should be well calibrated (refer to Section 3.2.8). The nominal magnification or scale bar given by the instrument manufacture, or a calibrated magnification, which was done a long time ago, could cause measurement error of 3%–10%. Although the transmission electron microscope (TEM) user does not need to calibrate the magnification each time unless required in the project, the magnifications should be calibrated as a routine instrumental maintenance.

5.1 Imaging Contrast

On a TEM image (also for any other image), to recognize a sample object, there should be sufficient contrast. The contrast C is defined by

$$C = \frac{(I_2 - I_1)}{I_1} = \frac{\Delta I}{I_1} \tag{5.1}$$

where ΔI is the intensity difference of I_1 and I_2 from two adjacent areas. Our eyes can only differentiate object with contrast greater than 5%–10% and we are unable to see the contrast below this limit. However, with the computer method, such contrast can be enhanced if the images are digitalized.

In TEM, the image contrast may be classified as scattering contrast (or amplitude contrast), which is based on the electron scattering events,

and phase contrast which is based on the phase changes for imaging (Fig. 5.1). The scattering contrast in the TEM mode includes mass-thickness contrast and diffraction contrast, which are the two principal types of scattering contrast. In the scanning TEM (STEM) mode, the images are based on scattering contrast, collected by dark-field (DF), annular dark-field (ADF), and high-angle ADF (HAADF) detectors. If the HAADF detector is used, the image contrast is Z-contrast, which represents the atomic number Z. The STEM contrast and phase contrast will be covered in Volume 2 for details.

5.2 Imaging with Mass-Thickness Contrast

Suppose the sample does not diffract electrons to form the Bragg diffraction, such as an amorphous sample, the image contrast in TEM is only from the mass and/or thickness effect. As shown in Fig. 5.2, a high mass region scatters electrons at larger angles than the low mass region. After deflection by the objective lens, the electrons at larger angles are excluded by the objective aperture, and thus fewer electrons from the high mass area contribute to the imaging, forming a darker imaging on the image plane. Oppositely, the counterpart of the low mass area thus forms a brighter area in the image.

Thickness makes similar effect as the mass. A thick area scatters electrons at larger angles than a thin area, and thus it appears as a darker area in the image.

By comparing Fig. 5.2(a) and (b), it is clear that a small objective aperture produces higher contrast but lower intensity on the image (the entire image appears darker), whereas a large objective aperture produces lower contrast but higher image intensity. Therefore, to get a higher contrast, a small objective aperture is preferred (the high-contrast aperture below the general objective aperture uses even smaller portion of the central beam to get a higher contrast, refer to Fig. 3.12).

The accelerating voltage also affects the mass-thickness contrast. If the accelerating voltage is lowered, both the scattering angle and the cross section increase, causing an increase of the contrast. Therefore, if the contrast is a major concern, such as polymer or biological samples, a lower voltage is used (80–120 kV). However, the lower voltage reduces the imaging resolution.

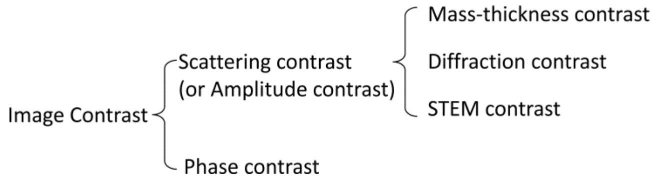

***Fig. 5.1** Classification of imaging contrast.*

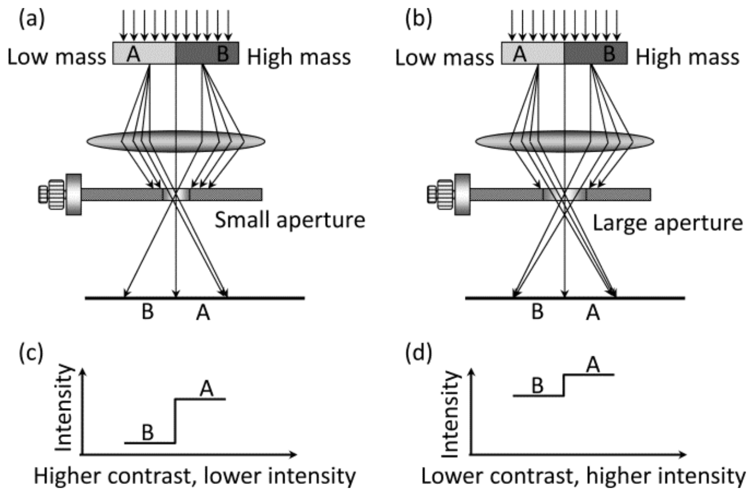

***Fig. 5.2** Mass-thickness contrast. Grain A has a low mass and grain B has high mass. A small objective aperture is used in (a) while a large aperture is used in (b), yielding higher contrast (while lower image intensity) and lower contrast (while higher image intensity), as shown in (c) and (d), respectively.*

5.3 Imaging with Diffraction Contrast

5.3.1 Formation of Diffraction Contrast

Diffraction contrast is induced by diffraction phenomena from crystalline samples. Its formation is illustrated in Fig. 5.3. The sample contains grains A and B. Grain A is at the Bragg diffraction position, so that part of the incident electrons are diffracted and the rest part of electrons transmitted. If the incident beam intensity is I_0 and diffracted beam is I_D, the transmitted beam intensity $I_1 = I_0 - I_D$. However, grain B is not at the Bragg

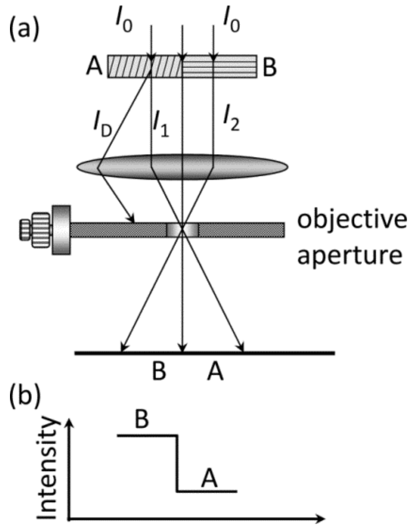

Fig. 5.3 (a) Formation of diffraction contrast; (b) image intensity.

diffraction conditions, so no diffraction happens and the transmitted beam intensity equals the original incident beam intensity, $I_2 = I_0$. Thus, $I_1 < I_2$. If a small objective aperture is used for imaging and the diffracted beam (with intensity I_D) is excluded, on the image grain A appears as darker than grain B, which is the diffraction contrast.

In real samples, if different grains are all at or near the Bragg diffraction conditions but at different zone axes, or at the same zone axis but they are slightly tilted, the diffraction contrast still contributes to imaging since the diffraction beam intensities are not exactly the same. Fig. 5.4(a) shows a bright-field (BF) image of a quartz sample with three grains A, B, and C. These grains are clearly shown in the DF image in Fig. 5.4(b). The quartz crystal is hexagonal, with a = 0.491 nm and c = 0.541 nm. The selected-area electron diffraction (SAED) pattern from grain A is at [001] zone axis with strong diffraction spots while the direct beam is weak, as shown in Fig. 5.4(c), so the grain A exhibits a dark contrast in the image. Grain B is at near [001] zone axis (Fig. 5.4d), so its image contrast is brighter than grain A. However, grain C is far off its [012] zone axis, as shown in Fig. 5.4(e). The center direct beam (000) is strong, and therefore on the image grain C appears as bright. After tilting, grain C reaches [012] zone axis, as shown in Fig. 5.4(f).

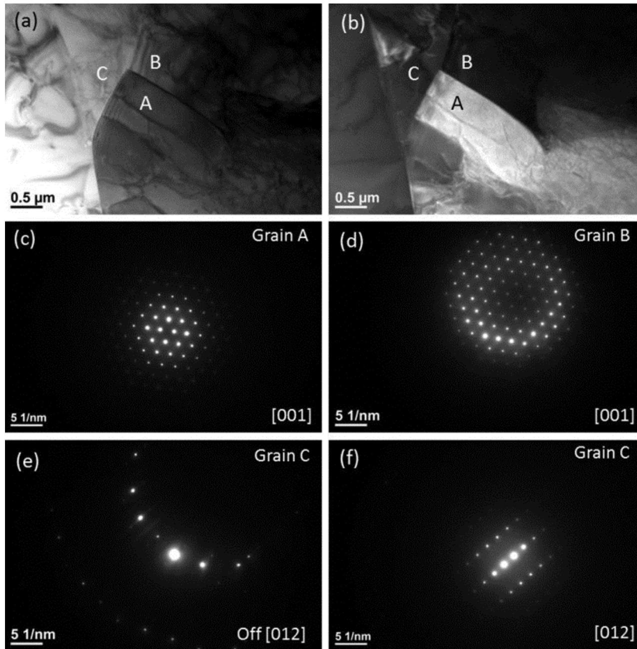

***Fig. 5.4** (a) BF image of a quartz sample showing three grains; (b) DF image; (c) SAED pattern from grain A along [001] zone axis; (d) SAED from grain B near [001] zone axis; (e) SAED from grain C that is far off [012]; (f) SAED from grain C after tilting to [012].*

Even within a grain, the diffraction contrast may appear due to the different diffraction conditions. Fig. 5.5(a) shows a BF image from a highly deformed stainless steel sample. High-density dislocation cells are present inside a grain, forming subgrains of dislocation cells with width ~200 nm. The SAED pattern in Fig. 5.5(b) exhibits highly distorted lattices. Although the strong spots are about at the [001] zone axis, lattices are rotated forming a pattern similar to polycrystal rings. The contrast in the image comes from the differences of the diffraction conditions.

In the BF image, areas exhibiting a darker contrast are most likely at or near Bragg diffraction conditions. Therefore, if SAED is needed, take patterns from these darker areas so that it is easier to get an SAED pattern, which is already at or near a zone axis with strong Bragg reflections.

In amorphous samples, since no diffraction happens over the sample, the image contrast comes only from mass-thickness contrast.

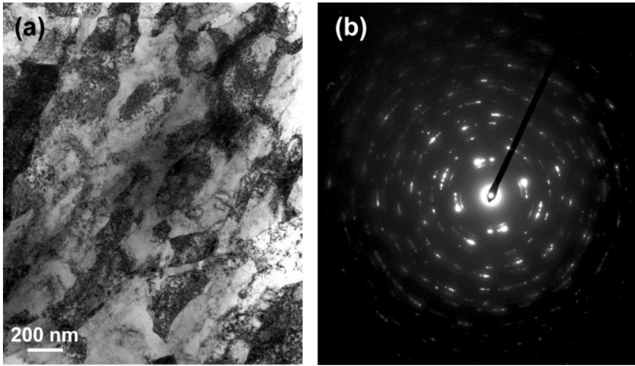

Fig. 5.5 (a) BF of a stainless steel sample shows subgrains composed of dislocations; (b) SAED pattern.

5.3.2 *Central Dark-Field Imaging*

Central dark-field imaging (CDF) is used for imaging objects with diffraction contrast. Fig. 5.6(a) shows a BF image from a NiTi alloy showing martensite plates [1]. From the dark area as indicated with a circle in Fig. 5.6(a), an SAED pattern in obtained, as shown in Fig. 5.6(c). By selecting the spot marked with a circle and tilting it into the center using beam tilt, the image then becomes a CDF image as shown in Fig. 5.6(b). Below are the operating procedures for CDF imaging:

1. In the BF image mode, select an area using diffraction aperture and get an SAED pattern in the diffraction mode.
2. Align the (000) spot to the center of the screen using Projector Lens Shift (neither beam shift nor beam tilt). Use binoculars to ensure the (000) is exactly at the center. Record the SAED pattern.
3. In the diffraction mode, switch to DF mode (the pattern may move depending on the previous alignment), move a selected spot to the center of the screen using beam tilt. Ensure the selected spot is exactly at the center using binoculars. Switch between BF and DF modes and ensure (000) and the selected spot coincide at the same position.
4. Insert the objective aperture (normally a very small one or the smallest one) to include the (000) or the selected spot.
5. Switch from diffraction mode to image mode. Then the image is a BF image in the BF mode or a CDF image in the DF mode. Adjust brightness to get optimum contrast as needed.

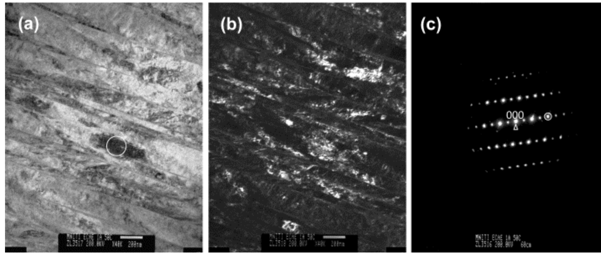

Fig. 5.6 CDF imaging. (a) BF; (b) CDF; (c) SAED; and the spot indicated with a circle is selected to move to the center to get the image in (b).

Note that in step 3, for the spot of interest and its counterpart on the other side of the direct beam (000), normally the weaker spot of the two spots is selected so that when it moves to the center, it becomes stronger to give a higher contrast of the CDF image. If a stronger spot is selected, it becomes darker when it is tilted to the center, causing weaker contrast of the CDF image.

To take a good CDF image, it is important to adjust the beam intensity in step 5 to get optimum contrast. The skilled user may even search in the DF mode while tilting the beam until a satisfactory CDF image is obtained. After tilting, it is necessary to check in the diffraction mode to ensure the correct beam was used for imaging.

A DF image may be simply formed by moving the objective aperture to select a spot. In this imaging way, the rays are off the optical axis, causing aberration and astigmatism, especially when the objective aperture is moved far away. However, on a C_s-corrected TEM, DF image can be taken in this way.

5.3.3 Two-Beam Condition

Two-beam condition is an approximation that only the direct beam $\mathbf{g}_0$ and a diffracted beam $\mathbf{g}$ are strong, whereas all other reflections are weak and their intensities are ignored. Since the reflection $\mathbf{g}$ is used for diffraction-contrast imaging, it is named as the operation vector. The experimental procedures to get a two-beam condition are described as follows:

1. Get a zone axis pattern and on the pattern, identify the direct beam $\mathbf{g}_0$ and the diffracted beam $\mathbf{g}$ for excitation. In Fig. 5.7(a), $\mathbf{g}$ = (200) is selected.

2. Draw a straight line across (000) and selected spot, as shown in Fig. 5.7(a), which is the rotation axis crossing the reflection **g**, that is, **g** is the tilting axis. Tilt the sample **largely** around **g** (while it is still near this zone axis) so that the center of the Laue zone axis moves along a perpendicular direction of the tilting axis (along either direction is fine). One may use a Kikuchi band to assist tilting (refer to Chapter 6 in Volume 2 for Kikuchi diffraction). In Fig. 5.7(b), the sample was tilted downward, and the center of the Laue zone axis is in the Kikuchi band across $\mathbf{g}_0$.
3. Tilting the sample **slightly** to make **g** strong. In Fig. 5.7(b), draw a line perpendicular to the previous $\mathbf{g}_0 - \mathbf{g}$ line and across the center of the Laue zone axis, which is the tilt axis for the slight tilt (it may not pass through $\mathbf{g}_0$ depending on the previous tilt). When the sample is tilted to the right side, **g** becomes stronger while **–g** becomes weaker. When the center of the Laue zone axis reaches the perpendicular bisector between $\mathbf{g}_0$ and **g**, it is the two-beam condition. If Kikuchi lines are visible, a dark line appears across $\mathbf{g}_0$ and a bright line across **g**.

Note that in Fig. 5.7(a), the sample can be tilted upward to select the same **g** downward. In Fig. 5.7(b), if the sample is tilted to the left side, ($\bar{2}00$) will be selected as the **g**.

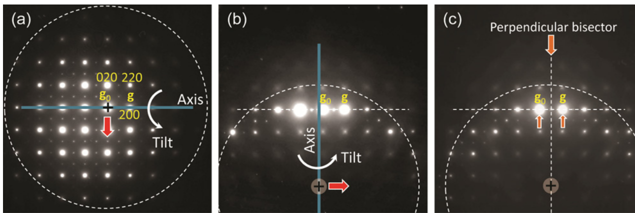

Fig. 5.7 Procedures to get a two-beam condition. (a) Zone-axis pattern, and g_{200} is selected; (b) SAED pattern after tilting downward from (a) for a larger angle; (c) SAED pattern after tilting to right from (b) for a small angle to get a two-beam pattern. The large circles represent the spot intensity distribution area, and the circle center (indicated with + sign), center of the Laue zone axis.

To get the two-beam condition, the sample must be physically tilted, and the beam tilt, as used to align the SAED patterns, cannot be used for the two-beam condition.

Fig. 5.8 shows a series of SAED patterns for two-beam conditions with different **g**. Fig. 5.8(a)–(d) are near [001] zone axis, while four different **g** vectors are selected. In Fig. 5.8(a), (220) is selected as **g**, and the Laue zone axis locates at the perpendicular bisector between (000) and (220). Tilting the sample downward (as indicated by an arrow) and controlling the orientation by the previously described method, $\mathbf{g}_{020}$ is obtained, as shown in Fig. 5.7(b). Again, the center of the Laue zone axis is located at the perpendicular bisector of $\mathbf{g}_0$ and $\mathbf{g}_{020}$. Similarly, $\mathbf{g}_{2\bar{2}0}$ and $\mathbf{g}_{200}$ are obtained, as shown in Fig. 5.8(c) and (d), respectively. Starting from Fig. 5.8(d), tilt the sample around $\mathbf{g}_{200}$ by a large angle to reach [011] zone axis (the ideal angle between [001] and [011] is 45°). Near the [011] zone axis, in a similar way four different **g** vectors are obtained, as shown in Fig. 5.8(e)–(h).

5.3.4 *Bragg-Diffracted Beam Intensity*

In case of two-beam condition, the intensity of Bragg-diffracted beam is

$$I_g = \left|\phi_g\right|^2 = \frac{\sin^2(\pi t S_{eff})}{(\xi_g S_{eff})^2} = 1 - I_0 \tag{5.2}$$

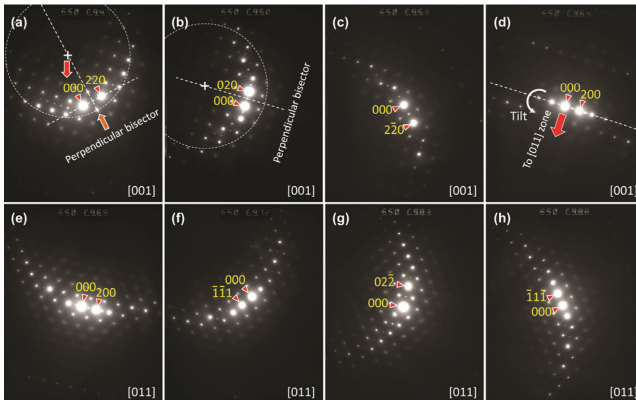

***Fig. 5.8** Two-beam conditions near [001] zone axis in (a–d) and near [011] zone axis in (e–h) after tilting around $\mathbf{g}_{200}$.*

Here, ϕ_g is the amplitude of the diffracted beam, t is the specimen thickness, s_{eff} is the effective excitation error, ξ_g is the extinction distance, and I_0 is the intensity of the direct beam. It is assumed that

$$I_g + I_0 = 1 \tag{5.3}$$

that is, there are only these two beams and all other beams are ignored. The effective excitation error s_{eff} is expressed as

$$s_{\text{eff}} = \sqrt{s^2 + \frac{1}{\xi_g^2}} \tag{5.4}$$

where s is the excitation error, which is defined from the ratio of distance x (between the Kikuchi bright line from the reflection **g**) to the distance R (between the direct beam and **g**) as follows:

$$s = \frac{x}{R}\frac{\lambda}{d^2} = \frac{x}{R}\lambda g^2 \tag{5.5}$$

Here, λ is the wavelength, d is the spacing of the reflection **g**, and $g = 1/d$. As will be mentioned in Chapter 6 in Volume 2, if the bright Kikuchi line goes across the reflection spot **g**, $s = 0$; if the bright line moves outward, $s > 0$; and if the bright line moves inward, $s < 0$. In the example shown in Fig. 5.9, $s > 0$.

The extinction distance ξ_g is expressed as

$$\xi_g = \frac{\pi V_c \cos\theta_B}{\lambda F_g} \tag{5.6}$$

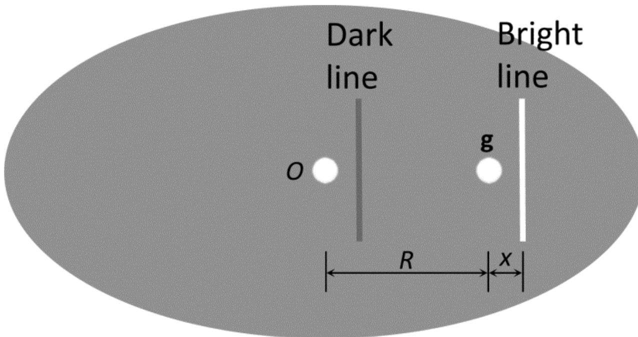

Fig. 5.9 Excitation error s is defined from the deviation of the bright Kikuchi line from g.

Here, V_c is the unit cell volume, θ_B is the Bragg angle, λ is the wavelength, and F_g is the structural factor $F(\theta)$ at the angle of θ_B. From Eq. 5.6, it follows that a higher voltage will result shorter λ and thus longer ξ_g, and a larger F (or higher atomic number Z) results in a shorter ξ_g.

In the open literature, there is limited or inconsistent ξ_g data on crystals [2, 3]. Here, we computed ξ_g of common metals at 100 and 200 kV, respectively, as listed in Tables 5.1–5.3. The lattice parameters are taken from reference [4], and the atomic scattering factors are calculated using the fitting parameters given by Doyle and Turner [5].

Taking the face-centered cubic (FCC) Al as an example (a = 4.0496 Å), $V_c = a^3 = 66.4104\,\text{Å}^3$. At 100 kV, λ = 0.0370 Å. When $\mathbf{g}$ = (111), d = 2.3380 Å, $\sin\theta = \dfrac{\lambda}{2d} = 0.0079$, and $\cos\theta$ = 1.0000. The scattering angle parameter $= \sin\theta / \lambda = 0.21385$, and thus f = 2.1221 according to the fitting parameters given by Doyle and Turner [5], and corrected f_{corr} = 2.5369 by multiplying with a relativistic factor of $(1 - v^2 / c^2)^{-1/2} = 1.1955$, where v is the speed of electrons at this accelerating voltage [3]. The structure factor $F = 4f_{corr} = 10.1477$ (Å). Therefore, according to Eq. 5.6,

$$\xi_g = \frac{\pi \times 66.4104 \times 1.0000}{0.0370 \times 10.1477} = 556\ (\text{Å})$$

For Mg with hexagonal close-packed (HCP) structure (a = 3.2094 Å, c = 5.2107 Å), $V_c = \dfrac{\sqrt{3}}{2}a^2c = 46.4809\,\text{Å}^3$. When $\mathbf{g}$ = (100), d = 2.7794 Å, $\sin\theta$ = 0.0067, $\cos\theta$ = 1.0000, s = 0.1799, f = 2.1941 (Å), f_{corr} = 2.6230 (Å), and F = f = 2.6230 (Å); thus, according to Eq. 5.6, ξ_g = 1,505 Å.

The ξ_g of compounds can be computed in a similar way. The ξ_g is an important parameter to compute the diffracted beam intensity in Eq. 5.2, and is used to estimate the sample thickness in the next section.

Table 5.1 Extinction distance ξ_g of FCC and diamond-structure crystals (Å).

Crystal	100 kV					200 kV				
	g_{111}	g_{200}	g_{220}	g_{311}	g_{400}	g_{111}	g_{200}	g_{220}	g_{311}	g_{400}
Al	556	664	1,064	1,316	1,659	704	842	1,347	1,667	2,101
γ-Fe	280	319	459	554	701	355	404	581	702	888
α-Co	265	301	430	518	653	335	381	545	656	828
Ni	262	297	421	505	634	332	376	533	639	803
Cu	290	322	440	522	649	367	408	557	661	823
Ag	238	263	358	428	541	302	333	453	542	686
Au	179	197	263	310	385	226	250	333	392	487
Si	619	–	760	1,338	1,245	784	–	962	1,694	1,577
Ge	483	–	511	843	726	611	–	647	1,068	919

Table 5.2 Extinction distance ξ_g of BCC crystals (Å).

Crystal	100 kV				200 kV			
	g_{110}	g_{200}	g_{211}	g_{310}	g_{110}	g_{200}	g_{211}	g_{310}
Fe	281	396	499	686	356	502	633	869
β-Ti	384	552	705	979	486	699	893	1,240
Nb	262	369	459	622	332	467	582	787
Mo	231	324	414	578	293	410	524	732
W	173	263	361	624	219	333	457	791

Table 5.3 Extinction distance ξ_g of HCP crystals (Å).

Crystal	100 kV				200 kV			
	g_{100}	g_{002}	g_{101}	g_{102}	g_{100}	g_{002}	g_{101}	g_{102}
Mg	1,505	933	864	1,160	1,906	1,181	1,094	1,470
α-Ti	689	432	390	514	873	548	495	650
ε-Co	500	305	279	356	634	387	353	451
Zn	672	369	362	431	851	467	458	547
Zr	599	369	331	422	759	467	420	534

5.3.5 *Thickness Fringes*

By ion milling or electropolishing method, the TEM specimens are mostly in wedged shapes. If the wedged sample is crystalline, thickness fringes can appear near the edges, which are the indications of thickness variations (Fig. 5.10a).

Suppose it is at the Bragg diffraction condition with $s = 0$, from Eq. 5.2, we have

$$I_g = \sin^2(\frac{\pi t}{\xi_g}) \tag{5.7}$$

Let $\frac{\pi t}{\xi_g} = (\frac{n}{2})\pi$, or

$$t = \frac{n}{2}\xi_g \tag{5.8}$$

where n is an integer.

If n is even, n = 0, 2, 4, …, or t = 0, ξ_g, $2\xi_g$, …, by Eq. 5.7 $I_g = 0$, and thus $I_0 = 1$. In this case, the direct beam has the intensity 1 but the diffracted beam intensity is zero (Fig. 5.10b). In the BF image, the image appears bright since only the direct beam is used for imaging. However, if **g** is used for image (DF image), the image appears dark.

If n is odd, n = 1, 3, 5, …, or $t = \frac{1}{2}\xi_g, \frac{3}{2}\xi_g, \frac{5}{2}\xi_g$, …, by Eq. 5.7 $I_g = 1$, and thus $I_0 = 0$. In this case, the direct beam intensity is zero, but the diffracted beam intensity is 1 (Fig. 5.10b). In the BF image using the direct beam, the image appears dark, that is, at these specific thickness positions dark fringes appear (between them are of course the bright fringes), as shown in Fig. 5.10(b). However, if **g** is used for image, at these thickness locations the image appears as bright fringes.

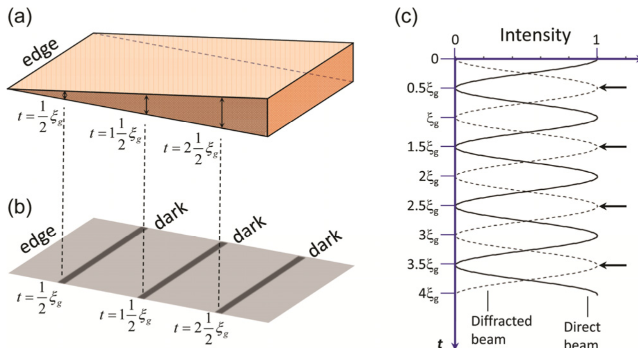

Fig. 5.10 (a, b) Formation of thickness fringes; (c) intensity of I_0 and I_g.

From Eq. 5.6, for a given same sample ξ_g is related to the wavelength λ. If the voltage is increased to get a shorter λ, ξ_g becomes longer, and consequently, the dark fringes in BF move toward thicker direction.

Thickness fringes are useful to estimate the sample thickness. The first dark fringe in BF corresponds to a sample thickness of $\frac{1}{2}\xi_g$. For Al at 200 kV, if **g** = (200), the thickness $t = \frac{1}{2}\xi_g = 421\,\text{Å}$. For high-resolution TEM (HRTEM) imaging, select thin areas near the wedge edge before the first dark fringe.

5.3.6 *Bend Contours*

For ductile TEM foils, such as metals, bending often happens during the sample preparation or handling. Sometime mishandling of the TEM foil by tweezers could severely bend the foil, even visible by eyes. Bending samples exhibit bend contours in the images.

As illustrated in Fig. 5.11, a crystalline sample is bent downward. Under parallel beam illumination condition, in certain areas the Bragg diffraction conditions are satisfied, yielding strong diffraction beams in these areas. Therefore, in the BF image using direct beam only, these areas appear as dark fringes. Since the sample is bent with a constant curvature, a pair of dark fringes appears on the image.

In DF image, these dark fringes may appear as bright lines if the diffracted beam is selected for imaging.

5.3.7 *Weak-Beam Dark-Field Imaging*

The CDF imaging mentioned in Section 5.3.2 is performed by moving normally a weak reflection toward center so that it becomes a stronger beam, and thus the CDF image has a sufficient high intensity. The weak-beam dark-field (WBDF) imaging is formed by moving the strong beam **g** in the two-beam condition to the center and then it becomes weak as it reached the center, and the consequently the DF image has a low intensity.

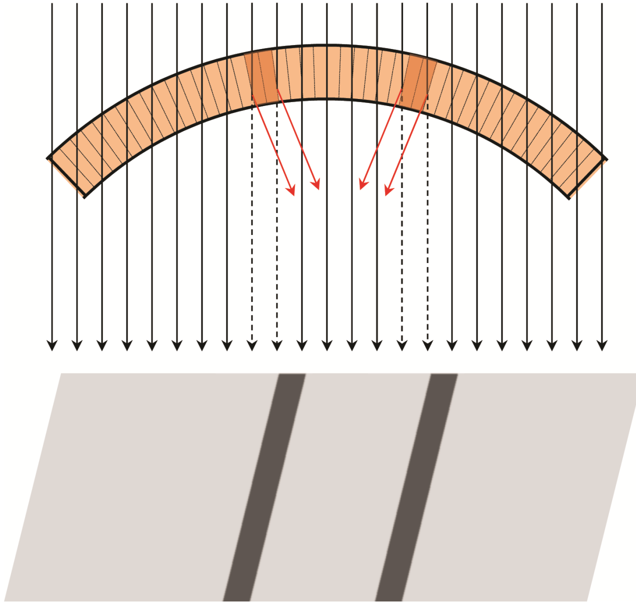

Fig. 5.11 Formation of bend contours.

The WBDF operation is illustrated in Fig. 5.12 with the following procedures:

1. Obtain a two-beam condition, that is, only the direct beam and diffracted beam **g** are strong, and the bright Kikuchi line crossing **g** (Fig. 5.12a). Use binoculars to align the direct beam exactly on the optical axis center (or screen center).
2. Switch to the DF mode and tilt the beam so that the strong reflection **g** moves toward the optical axis (the previous direct beam position). As it reaches the center, it becomes a weak beam (intensity is reduced). Use binoculars to ensure **g** is at the screen center. As shown in Fig. 5.12(b), since the sample remains the same position, by symmetric geometry relationship the 3**g** reflection now moves on the Ewald sphere, so both direct beam **O** and 3**g** become strong, while **g** and 2**g** are weak. Now the bright Kikuchi line is on 3**g**. Note that the Ewald sphere must pass through the direct beam **O**, and the (*hkl*) trace is on the perpendicular bisector of **g**–2**g** or **O**–3**g**.

3. Insert and align the smallest objective aperture on the screen center to include the **g** spot (also it is the same position of the previous direct beam position in BF mode).
4. Switch to the image mode to get a DF image, which is the WBDF image. Adjust the brightness to get an optimum intensity. However, it is often needed to go back to step 2 to ensure **g** is still in the center and 3**g** is still bright, and slightly adjust the beam tilt as needed.
5. Switch to BF mode, the image is then a BF image.

The WBDF image is very useful to reveal structure defects. Fig. 5.13 shows an example from a Ni-base superalloy [6, 7]. In the BF image in Fig. 5.13(a), the dislocations are not very clear due to the dislocation tangling, whereas in the WBDF image in Fig. 5.13(b) the hexagonal dislocation networks appear clearly. Thickness fringes can be found at the right side of the image.

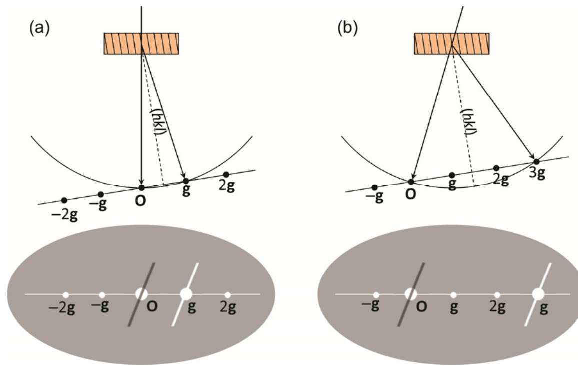

Fig. 5.12 Weak-beam dark-field imaging. (a) Two-beam condition; (b) g is tilted to the optical axis position to obtain a g/3g condition.

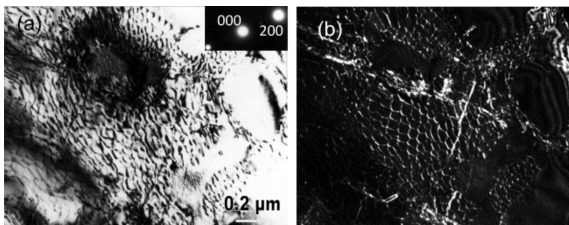

Fig. 5.13 Dislocation images in a Ni-base superalloy. (a) BF image; (b) WBDF image.

5.3.8 *Planar Defects*

Planar defects are formed by a transition or rotation between two crystals at their boundary, such as stacking faults (SFs), grain boundaries (GBs), phase boundaries (PBs) or anti-phase boundaries (APBs). In the TEM specimen, if these two crystals are aligned at the upper and down positions, and they are translated by a vector **R**, the resulted additional phase is

$$\alpha = 2\pi \mathbf{g} \cdot \mathbf{R} \tag{5.9}$$

Here, **g** is the operation vector. When

$$\mathbf{g} \cdot \mathbf{R} = 0 \tag{5.10}$$

the defect is invisible. Eq. 5.10 is the invisible criterion for defects, including other types of defects such as dislocations. If the defect is invisible using two operation vectors $\mathbf{g}_1$ or $\mathbf{g}_2$ (disappear under these two vectors, while appear using other **g** otherwise nobody knows there exists such a defect), the transition vector **R** is

$$\mathbf{R} \parallel \mathbf{g}_1 \times \mathbf{g}_2 \tag{5.11}$$

Common planar defects including:

- Stacking faults, with $\mathbf{R} = \frac{1}{3} < 111 >$, or $\mathbf{R} = \frac{1}{6} < 112 >$;
- Anti-phase boundaries, with $\mathbf{R} = \frac{1}{2} < 111 >$, or $\mathbf{R} = \frac{1}{4} < 110 >$.

A particular case is $\mathbf{R} = \frac{1}{3} < 111 >$-type SFs in FCC crystal. The $\mathbf{g} \cdot \mathbf{R}$ values are listed in Table 5.4.

Fig. 5.14 shows an example of SFs in a Ni-base superalloy [6, 7]. During the deformation at 873 K, $\frac{1}{3} < 112 >$-type partial dislocations shear Ni_3Al-type γ' phase, forming super stacking faults (SSFs). In Fig. 5.14(a) and (b), the SFs are visible with $\mathbf{g}_1$ = (020), while they are invisible when $\mathbf{g}_2$ = (220) as shown in Fig. 5.14(c). According to Table 5.4, there are some possibilities as follows:

1. $\mathbf{R} = \frac{1}{3}\left[\bar{1}11\right]$:

   $\mathbf{g}_1 \cdot \mathbf{R} = \frac{1}{3}(-0\times1+2\times1+0\times1) = \frac{2}{3}$, visible;

   $\mathbf{g}_2 \cdot \mathbf{R} = \frac{1}{3}(-2\times1+2\times1+0\times1) = 0$, invisible.

2. $\mathbf{R} = \frac{1}{3}\left[1\bar{1}1\right]$:

   $\mathbf{g}_1 \cdot \mathbf{R} = \frac{1}{3}(0\times1-2\times1+0\times1) = -\frac{2}{3}$, visible;

   $\mathbf{g}_2 \cdot \mathbf{R} = \frac{1}{3}(2\times1-2\times1+0\times1) = 0$, invisible.

In this example, these two operation vectors are not enough to identify either $\mathbf{R} = \frac{1}{3}[\bar{1}11]$ or $\mathbf{R} = \frac{1}{3}[1\bar{1}1]$. Normally it requires more operation vectors, even possibly from another zone axis, such as tilting from this [001] zone to [011] zone. Although in principle the vector **R** is uniquely determined whether two operation vectors $\mathbf{g}_1$ and $\mathbf{g}_2$ are found under which the defect is invisible, it is not necessarily to use it as the only way to determine **R**, as the **R** can be determined by the combination of the visibility conditions in Table 5.4 under other **g** conditions.

Table 5.4. Computed g.R values for $\mathbf{R} = \frac{1}{3} < 111 >$***-type SFs in FCC crystal.***

	$\mathbf{R} = \frac{1}{3}[111]$	$\mathbf{R} = \frac{1}{3}[\bar{1}11]$	$\mathbf{R} = \frac{1}{3}[1\bar{1}1]$	$\mathbf{R} = \frac{1}{3}[11\bar{1}]$
g = (200)	2/3	–2/3	2/3	2/3
g = (020)	2/3	2/3	–2/3	2/3
g = (002)	2/3	2/3	2/3	–2/3
g = (111)	1	1/3	1/3	1/3
g = $(\bar{1}11)$	1/3	1	–1/3	–1/3
g = $(1\bar{1}1)$	1/3	–1/3	1	–1/3
g = $(11\bar{1})$	1/3	–1/3	–1/3	1
g = (022)	4/3	4/3	0	0
g = $(02\bar{2})$	0	0	–4/3	4/3
g = (202)	4/3	0	4/3	0
g = $(20\bar{2})$	0	–4/3	0	4/3
g = (220)	4/3	0	0	4/3
g = $(2\bar{2}0)$	0	–4/3	4/3	0

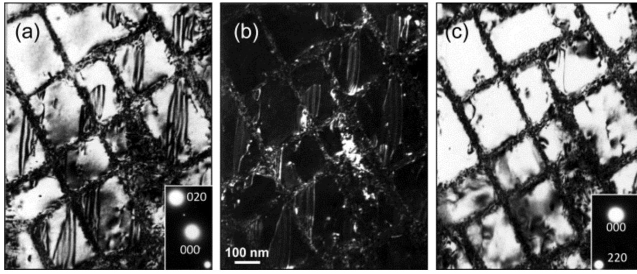

Fig. 5.14 Stacking faults in a Ni-base superalloy. (a) BF image with g = (020); (b) WBDF image of (a); (c) BF image with g = (220).

5.3.9 Dislocations

Dislocations are linear defects in the specimens, and such magnitude and direction of the lattice distortion in the crystal lattice are defined using a Burgers vector [8]. Dislocations are classified as (1) edge dislocations, whose Burgers vectors **b** are perpendicular to their lines; (2) screw dislocations, whose Burgers vectors **b** are parallel to their lines; and (3) mixed dislocations, with mixed characters of edge and screw dislocations. The following characters can be identified using TEM:

1. Burgers vector **b**. The general dislocation invisibility criterion is

$$\mathbf{g}\cdot\mathbf{b}=0 \tag{5.12}$$

   However, this $\mathbf{g}\cdot\mathbf{b}=0$ invisibility criterion holds not only for screw dislocations but also for edge dislocations if **g** is parallel to the dislocation line **u** [9]. In the case of pure edge dislocations, complete invisibility requires not only $\mathbf{g}\cdot\mathbf{b}=0$ but also an additional residual contrast criterion [9-14]

$$\mathbf{g}\cdot(\mathbf{b}\times\mathbf{u})=0 \tag{5.13}$$

2. Dislocation line direction **u**, which requires tilting experiment since a single TEM image gives only the direction of a 2D projection. When **u** is determined, it is possible to determine the dislocation character of edge, screw, or mixed dislocation.
3. Dislocation glide plane, which is $\mathbf{b}\times\mathbf{u}$.

If the value of $\mathbf{g} \cdot (\mathbf{b} \times \mathbf{u})$ is not zero even though $\mathbf{g} \cdot \mathbf{b} = \mathbf{0}$, residual contrast can appear [9–14].

When a dislocation is extinguished under $\mathbf{g}_1$ and $\mathbf{g}_2$ operations, $\mathbf{b}$ is therefore parallel to $\mathbf{g}_1 \times \mathbf{g}_2$, that is,

$$\mathbf{b} \parallel \mathbf{g}_1 \times \mathbf{g}_2 \tag{5.14}$$

The computed $\mathbf{g} \cdot \mathbf{b}$ values of FCC and body-centered cubic (BCC) crystals are listed in Tables 5.5 and 5.6, respectively. By using different $\mathbf{g}$ operations, the Burgers vector $\mathbf{b}$ can be determined.

Fig. 5.15 shows a geometrical analysis of the dislocations formed at 873 K in a Ni-base superalloy [7]. In Fig. 5.15(a) taken along the [001] zone, numerous parallel dislocation lines along [110] are present, even though they are mixed with other dislocations. The Burgers vector of these parallel dislocations is determined to be $\mathbf{b} = \frac{a}{2}[101]$ as they are

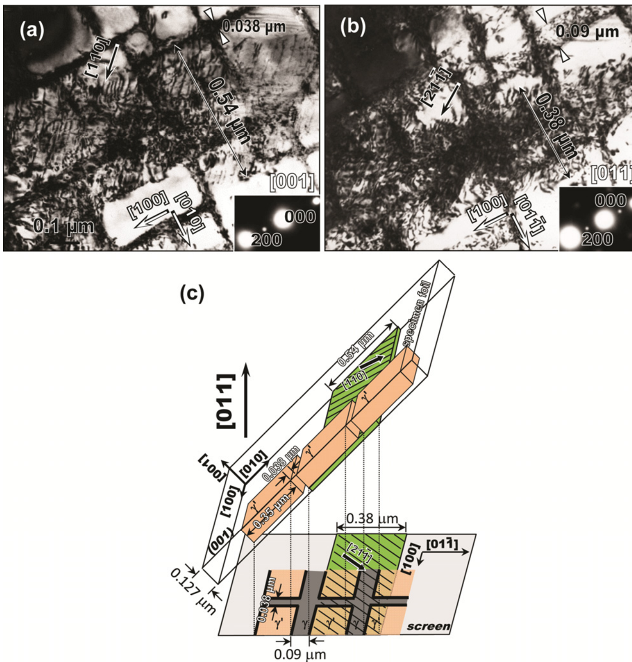

Fig. 5.15 Geometric analysis of a dislocation concentration using a tilting method from the [001] zone axis (a) to [011] (b). The schematic projection from [001] to [011] showing the geometric relationship of this region is shown in (c).

Table 5.5 Computed g·b values for perfect dislocations in FCC crystal.

	$b=\frac{1}{2}[110]$	$b=\frac{1}{2}[101]$	$b=\frac{1}{2}[011]$	$b=\frac{1}{2}[1\bar{1}0]$	$b=\frac{1}{2}[10\bar{1}]$	$b=\frac{1}{2}[01\bar{1}]$
$g=(111)$	1	1	1	0	0	0
$g=(\bar{1}11)$	0	0	1	–1	–1	0
$g=(1\bar{1}1)$	0	1	0	1	0	–1
$g=(11\bar{1})$	1	0	0	0	1	1
$g=(200)$	1	1	0	1	1	0
$g=(020)$	1	0	1	–1	0	1
$g=(002)$	0	1	1	0	–1	–1
$g=(220)$	2	1	1	0	1	1
$g=(202)$	1	2	1	1	0	–1
$g=(022)$	1	1	2	–1	–1	0
$g=(2\bar{2}0)$	0	1	–1	2	1	–1
$g=(20\bar{2})$	1	0	–1	1	2	1
$g=(02\bar{2})$	1	–1	0	–1	1	2

Table 5.6 Computed g·b values for perfect dislocations in BCC crystal.

	$b=\frac{1}{2}[111]$	$b=\frac{1}{2}[\bar{1}11]$	$b=\frac{1}{2}[1\bar{1}1]$	$b=\frac{1}{2}[11\bar{1}]$
$g=(110)$	1	0	0	1
$g=(101)$	1	0	1	0
$g=(011)$	1	1	0	0
$g=(1\bar{1}0)$	0	–1	1	0
$g=(10\bar{1})$	0	–1	0	1
$g=(01\bar{1})$	0	0	–1	1
$g=(200)$	1	–1	1	1
$g=(020)$	1	1	–1	1
$g=(002)$	1	1	1	–1
$g=(211)$	2	0	1	1
$g=(121)$	2	1	0	1
$g=(112)$	2	1	1	0
$g=(\bar{2}11)$	0	2	–1	–1
$g=(2\bar{1}1)$	1	–1	2	0
$g=(21\bar{1})$	1	–1	0	2
$g=(\bar{1}21)$	1	2	–1	0
$g=(1\bar{2}1)$	0	–1	2	–1
$g=(12\bar{1})$	1	0	–1	2
$g=(\bar{1}12)$	1	2	0	–1
$g=(1\bar{1}2)$	1	0	2	–1
$g=(11\bar{2})$	0	–1	–1	2

visible with **g** = ±(200), ±($\bar{2}20$) and ±(220) while invisible with **g** = ±(020) and ±($11\bar{1}$). These dislocation lines seem to be long and straight in Fig. 5.15(a), implying that they may lie in the (001) plane of the thin foil. This assumption is confirmed by a tilting experiment. Fig. 5.15(b) shows this same region at the [011] zone after tilting around the **g** = (200) vector from the [001] zone. The geometric relationship between them is illustrated in Fig. 5.15(c). It is seen that the width of the dislocation region is about 0.54 μm at the [001] zone in Fig. 5.15(a), while it shortens to about 0.38 μm after tilting to the [011] zone in Fig. 5.15(b). The ratio of these two widths is 1.42, which is near the expected value of $\sqrt{2}$ if the thickness of the concentration region in γ is small compared with the width. On the other hand, the projected width of the narrow γ phase along [100] broadens from 0.038 μm at [001] zone to

0.09 μm at the [011] zone, as shown at the top sides of Fig. 5.15(a) and (b), respectively. Hence, an estimate of the specimen thickness is 0.09 × $\sqrt{2}$ = 0.127 μm. It should be noted that dislocation lines along $[21\bar{1}]$ at the [011] zone are still visible in the high-density tangles in Fig. 5.15(b), which are the projections of the [110] direction dislocation lines at the [001] zone. As the line direction is **u** = [110], these dislocations are of a 60° (angle between **b** and **u**) character, that is, mixed dislocations.

The dislocation network microstructure is shown in Fig. 5.16 (the same area as Fig. 5.13). At the γ/γ' interfaces, regular dislocation networks are developed. A series of images are taken from the same area at the [001] zone (Fig. 5.16a–c) and the [011] zone (Fig. 5.16d–f) after tilting around the vector of **g** = (200). Table 5.7 lists the analysis results, and schematic illustrations of the visibility–invisibility of the hexagonal networks are placed at the bottom right corners, where the heavy solid lines represent visible and thin broken lines invisible. In the WBDF image with **g** = (200) in Fig. 5.16(a), the hexagonal dislocation networks are visible along all three directions, labeled as 1, 2, and 3. The framed region in Fig. 5.16(a) is enlarged in Fig. 5.17. The dislocation 1 is invisible with **g** = $(2\bar{2}0)$ (Fig. 5.16c) and **g** = $(\bar{1}1\bar{1})$ (Fig. 5.16e) while visible with other **g** conditions; thus $\mathbf{b}_1 = \frac{a}{2}$ [110]. Dislocation 2 is invisible with **g** = $(11\bar{1})$ (Fig. 5.16d) and **g** = $(\bar{2}\bar{2}0)$ (not shown in Fig. 5.16); thus $\mathbf{b}_2 = \frac{a}{2}[\bar{1}10]$. However, for dislocation 3 with line direction of $\mathbf{u}_3 = [010]$, it is invisible only with **g** = $(0\bar{2}0)$ in Fig. 5.16(b). There exist two kinds of possible Burgers vectors: one is $\mathbf{b}_3 = \frac{a}{2}[101]$ or $\mathbf{b}_3 = \frac{a}{2}[10\bar{1}]$, and the other one is $\mathbf{b}_3 = a[100]$, as shown in Fig. 5.18(a) and (b), respectively [11]. All of them are edge dislocations. In Fig. 5.18(a), the product of **b** = *a*[100] is produced whereas in Fig. 5.18(b) two pairs of $\frac{a}{2}$ <110> dislocations do not react. These dislocation lines may further rearrange to construct ideal hexagonal networks as shown in Fig. 5.18(c) and (d), respectively. After the rearrangement, the dislocations are no longer of edge character. It is unable to distinguish the two possibilities since their visibility–invisibility

conditions are the same under a variety of $\mathbf{g}$ conditions for both $\mathbf{g}\cdot\mathbf{b}=0$ and $\mathbf{g}\cdot(\mathbf{b}\times\mathbf{u})=0$ criteria [11]. For example, when $\mathbf{g}$ = $(02\overline{2})$ and $\mathbf{b}_3 = a[100]$, $\mathbf{g}\cdot\mathbf{b}_3=0$ while $\mathbf{g}\cdot(\mathbf{b}_3\times\mathbf{u}_3)=-2$, so it is still visible. Therefore, HRTEM imaging (refer to Chapter 7 in Volume 2) was used to identify the dislocation networks.

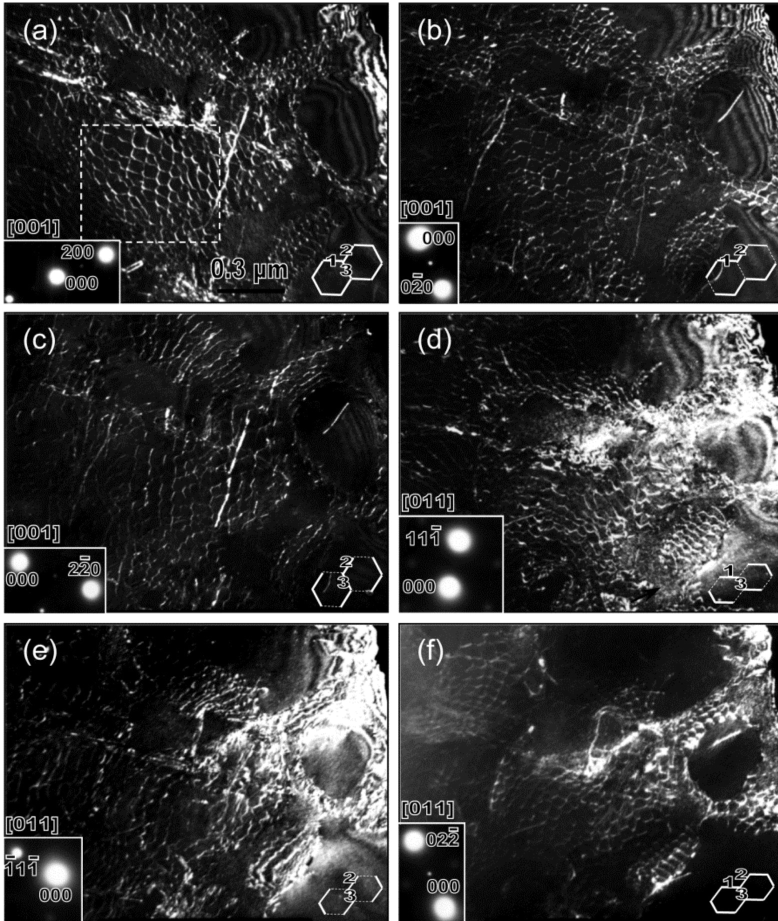

Fig. 5.16 Dislocation analysis along [001] (a–c) and [011] (d–f) zone axes after tilting.

Table 5.7 Dislocation analysis in Fig. 5.16 (vis: visible; inv: invisible).

Dislocation	g						b	u	Character	Glide plane (**b** × **u**)
	200	$0\bar{2}0$	$0\bar{2}0$	$11\bar{1}$	$\bar{1}1\bar{1}$	$02\bar{2}$				
1	vis	vis	inv	vis	inv	vis	$\frac{a}{2}[110]$	$[\bar{1}10]$*	edge*	(001)
								$[\sqrt{3}10]$ **	75°**	
2	vis	vis	vis	inv	vis	vis	$\frac{a}{2}[\bar{1}10]$	[110] *	edge*	$(00\bar{1})$
								$[\sqrt{3}10]$ **	75°**	
3	vis	inv	vis	vis	vis	vis	$\frac{a}{2}[101]$	[010]	edge	$(\bar{1}01)$
							$\frac{a}{2}[10\bar{1}]$	[010]	edge	(101)
							a [100]	[010]	edge	(001)

Note:
* These are obtained by considering dislocations 1 and 2 are perpendicular to each other, see Fig. 5.18(a) and (b).
** These are obtained by considering dislocations 1 and 2 are rearranged to form ideal hexagonal networks, see Fig. 5.18(c) and (d).

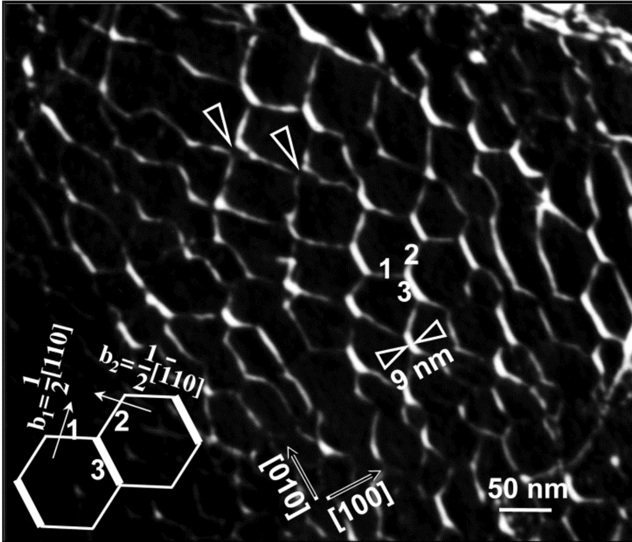

Fig. 5.17 Enlarged hexagonal dislocation networks in Fig. 5.16(a).

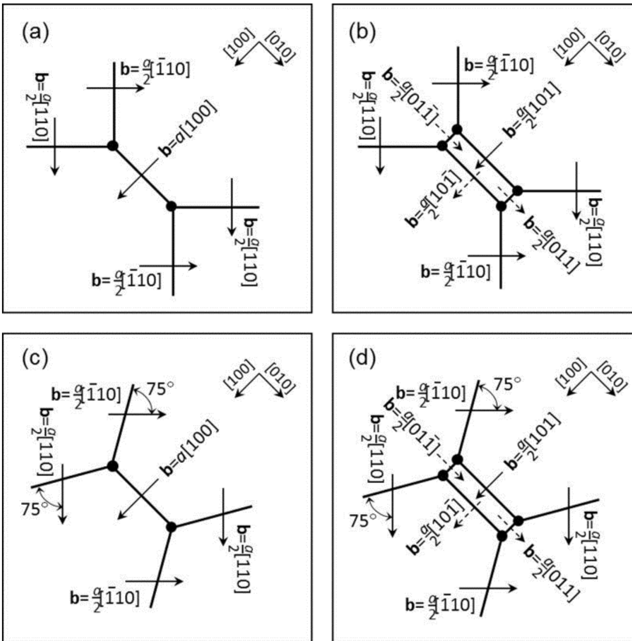

Fig. 5.18 Two kinds of possible dislocation networks after tensile deformation with large strains [11] (a, b), and ideal hexagonal configuration after further line rearrangement due to the line tensions (c, d).

Fig. 5.19(a) shows a typical HREM image of the networks. This image is taken from a relatively thick area away from the edge of the specimen and is presented at relatively low magnification to illustrate the regular hexagonal networks as projected along the [001] zone. In the thick region, dislocation lines parallel to the foil surface may exist; thus, it is possible to observe these dislocations in HREM images due to contrast induced by the strain fields around the dislocations. In Fig. 5.19(a), the dislocation lines are marked with broken lines, and the framed area is enlarged in Fig. 5.19(b), in which the lattice fringes are visible. The inset in Fig. 5.19(b) is a noise-eliminated enlargement of the region enclosed by black dotted lines at the top of Fig. 5.19(b). Within this inset, a simulated contrast image using the γ' phase structure along [001] (2×2 planar cells) is shown. Although γ/γ' may overlap along [001] in the specimen, the good agreement between the experimental image and the simulation based on γ' implies that the thickness of γ phase can be ignored. Here, the strong white image spots correspond to the Ni atoms, whereas the small image spots correspond to Al atoms. A planar unit cell is outlined by white dotted lines with dimension of 0.36 nm, which is the lattice parameter a of the γ' phase. Based on this unit cell, the principal directions [100] and [010] can be identified. It is seen that dislocation 3 segment lies along [010], which is composed of a pair of dislocations with a spacing of 9 nm, while segments 1 and 2 are almost perpendicular to each other approximately along <110>. Other pairs of dislocations are also observed only along the [010] direction. Based on a measurement of 49 such pairs from different areas in the sample, the average spacing was found to be 8.5 nm with standard deviation of 1.5 nm (pairs with large spacing over 13 nm are not taken into account). This average spacing is comparable to the width (9 nm) of segment 3 in Fig. 5.17. Moreover, the hexagonal cell size of 60 nm in Fig. 5.19(a) is also close to the cell size of 65 nm in Fig. 5.17. Thus, the configuration of segment 3 is a pair of $\frac{a}{2}\langle 110 \rangle$ dislocations (as in Fig. 5.18b) rather than a single $a\langle 100 \rangle$ dislocation (as in Fig. 5.18a). In fact, the width of segment 3 is much wider than segments 1 and 2 in Fig. 5.17, as also noted in reference [11] further supporting this conclusion. In some cases, the separation of these

dislocation pairs is visible even in the WBDF image in Fig. 5.17, as indicated by arrowheads. Separated pairs are observed only along the [010] direction.

Most networks observed in this experiment are composed of two pairs as shown above. Note that in some cases, even in the HREM images, segment 3 is observed as a single dislocation. An example is shown in Fig. 5.20 at the [001] zone in a relatively low magnification along the trace of the γ/γ' interface. Separated dislocation pairs along [010] are observed in the lower half of Fig. 5.20, whereas single-dislocation lines along [010] are seen in the upper half, as indicated by the arrowheads.

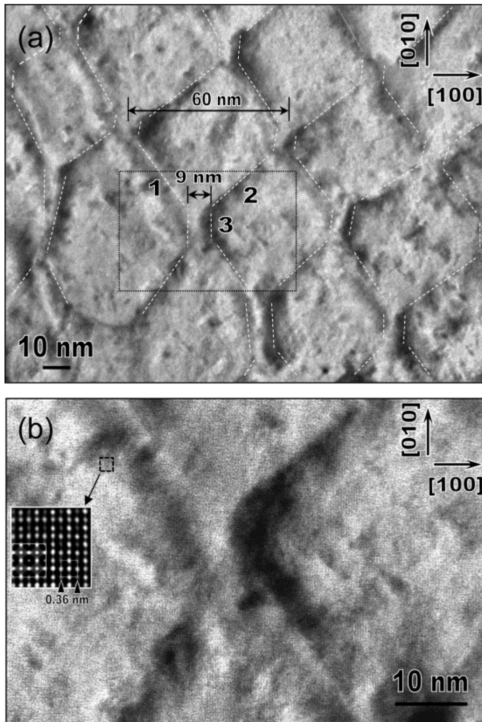

Fig. 5.19 (a) HREM image of the dislocation networks printed at a low magnification showing dislocation pairs of segment 3 in the networks; (b) enlarged image of framed region in (a). The insert at the left side of (b) is from the small framed region above it. This inset also includes a contrast simulated image of the γ' structure (voltage E = 400 kV, spherical aberration coefficient C_s = 1 mm, chromatic defocus spread Δ = 8 nm, semiangle of beam convergence q = 0.55 mrad, foil thickness t = 15 nm, and defocus Δf = –30 nm).

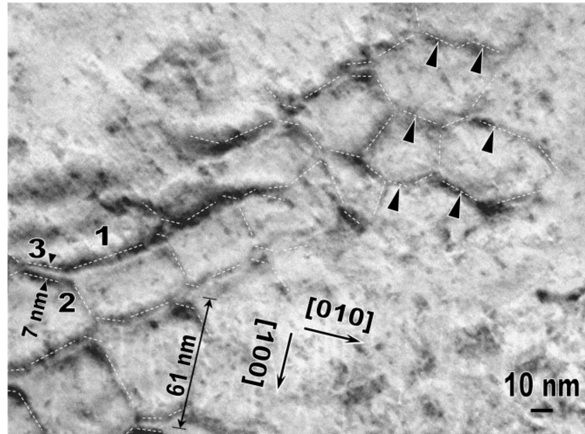

Fig. 5.20 HREM image of the dislocation networks printed at a low magnification showing dislocation pairs and single dislocations (indicated by arrowheads).

References

[1] I. Karaman, H.E. Karaca, H.J. Maier, Z.P. Luo. The effect of severe marforming on shape memory characteristics of a Ti-rich NiTi alloy processed using equal channel angular extrusion. *Metall. Mater. Trans.* **A34**, 2527–2539 (2003).

[2] D.B. Williams, C.B. Carter. *Transmission Electron Microscopy: A Textbook for Materials Science*. Springer, New York, 2009.

[3] A.K. Head. *Computed Electron Micrographs and Defect Identification*. North-Holland Pub. Co., Amsterdam, 1973.

[4] P. Villars, editor-in-chief; H. Okamoto, K. Cenzual, section editors. *Crystal Structures and Lattice Parameters of Allotropes of Metallic Elements*. ASM International, Materials Park, OH, 2007.

[5] P.A. Doyle, P.S. Turner. Relativistic Hartree-Fock X-ray and electron scattering factors. *Acta Cryst.* **A24**, 390–397 (1968).

[6] Z.P. Luo, Y. Tang, Z. Wu, M.J. Kramer, R.W. McCallum. The dislocation structure of a single-crystal $\gamma+\gamma'$ two-phase alloy after tensile deformation. *Mater. Charact.* **43**, 293–301 (1999).

[7] Z.P. Luo, Z.T. Wu, D.J. Miller. The dislocation microstructure of a nickel-base single-crystal superalloy after tensile fracture. *Mater. Sci. Eng.* **A354**, 358–368 (2003).

[8] P.B. Hirsch, A. Howie, R.B. Nicholson, D.W. Pashley, M.J. Whelan. *Electron Microscopy of Thin Crystals*. Krieger, Florida, 1977.

[9] M. Rühle, M. Wilkens. Transmission electron microscopy. In: R.W. Cahn, P. Haasen. *Physical Metallurgy*, Volume 1, Elsevier, The Netherlands. Pp. 1033–1114 (1996).

[10] J. Müller, G. Eggeler, E. Spiecker. On the identification of superdislocations in the γ′-phase of single-crystal Ni-base superalloys – An application of the LACBED method to complex microstructures. *Acta Mater.* **87**, 34–44 (2015).

[11] H. Gabrisch, D. Mukherji, R.P. Wahi. Deformation-induced dislocation networks at the γ–γ′ interfaces in the single-crystal superalloy SC16: A mechanism-based analysis. *Phil. Mag.* **74A**, 229–249 (1996).

[12] T. Link, C. Knobloch, U. Glatzel. <100> Burgers vector in single phase γ′ material verified by image simulation. *Scripta Mater.* **40**, 85–90 (1999).

[13] T. Link, A. Epishin, M. Klaus, U. Brückner, A. Reznicek. <1 0 0> dislocations in nickel-base superalloys: Formation and role in creep deformation. *Mater. Sci. Eng.* **A405**, 254–265 (2005).

[14] A. Kostka, G. Mälzer, G. Eggeler, A. Dlouhy, S. Reese, T. Mack. $L1_2$-phase cutting during high temperature and low stress creep of a Re-containing Ni-base single crystal superalloy. *J. Mater. Sci.* **42**, 3951–3957 (2007).

APPENDIX I

SAED Indexing Table of Primitive Cubic Structure

PC (indices are computed up to 6)

a = 1, b = 1, c = 1, alpha = 90°, beta = 90°, gamma = 90°

D1(max)	h	k	l
1	1	0	0
0.707	-1	1	0
0.577	1	1	-1
0.447	-2	1	0
0.408	2	1	-1
0.333	2	-2	1

R2/R1	Angle	D1(max)	H1	K1	L1	H2	K2	L2	U	V	W
1	60	0.707	-1	1	0	-1	0	1	1	1	1
1	113.58	0.447	-2	1	0	0	-2	1	1	2	4
1	80.41	0.408	2	1	-1	-1	2	-1	1	3	5
1	116.39	0.333	2	-2	1	1	2	-2	2	5	6
1	90	1	1	0	0	0	1	0	0	0	1
1.095	90	0.447	-2	1	0	-1	-2	1	1	2	5
1.095	100.52	0.447	-2	0	1	1	-2	1	2	3	4
1.225	90	0.707	-1	1	0	-1	-1	1	1	1	2
1.225	105.79	0.408	1	-2	1	2	1	-2	3	4	5
1.225	97.82	0.408	2	1	-1	-2	2	-1	1	4	6
1.291	104.96	0.577	1	1	-1	-2	1	0	1	2	3
1.342	90	0.447	-2	1	0	-1	-2	2	2	4	5
1.342	72.65	0.447	-2	1	0	-2	-2	1	1	2	6
1.414	73.57	0.447	0	-2	1	3	-1	0	1	3	6
1.414	98.13	0.447	0	-2	1	3	0	-1	2	3	6
1.414	90	1	1	0	0	0	1	-1	0	1	1
1.472	83.5	0.408	1	-2	1	3	0	-2	4	5	6
1.581	108.43	0.707	0	-1	1	2	0	-1	1	2	2
1.612	75.64	0.447	-2	0	1	0	-3	2	3	4	6
1.673	90	0.447	-2	0	1	1	-3	2	3	5	6
1.732	73.22	0.707	-1	1	0	-2	-1	1	1	1	3
1.732	78.9	0.577	1	1	-1	-2	2	-1	1	3	4
2.082	99.21	0.577	1	1	-1	-3	2	0	2	3	5
2.121	90	0.707	-1	1	0	-2	-2	1	1	1	4
2.121	76.37	0.707	-1	1	0	-2	-1	2	2	2	3
2.16	90	0.577	1	1	-1	-3	2	-1	1	4	5
2.236	102.92	0.707	0	-1	1	3	0	-1	1	3	3
2.236	90	1	1	0	0	0	2	-1	0	1	2
2.345	90	0.707	0	-1	1	3	-1	-1	2	3	3
2.646	79.11	0.707	-1	1	0	-3	-2	1	1	1	5
2.646	97.24	0.577	1	1	-1	-4	2	-1	1	5	6
2.915	90	0.707	-1	1	0	-2	-2	3	3	3	4
2.915	99.87	0.707	0	-1	1	4	0	-1	1	4	4
2.915	80.13	0.707	-1	1	0	-3	-2	2	2	2	5
3.082	90	0.707	-1	1	0	-3	-3	1	1	1	6
3.162	90	1	1	0	0	0	3	-1	0	1	3

R2/R1	Angle	D1(max)	(H1 K1 L1)	(H2 K2 L2)	[U V W]
3.24	81.12	0.707	0 -1 1	4 -2 -1	3 4 4
3.317	81.33	0.707	-1 1 0	-3 -2 3	3 3 5
3.606	97.97	0.707	0 -1 1	5 0 -1	1 5 5
3.606	90	1	1 0 0	0 3 -2	0 2 3
3.674	90	0.707	0 -1 1	5 -1 -1	2 5 5
3.808	82.45	0.707	-1 1 0	-3 -2 4	4 4 5
3.873	82.58	0.707	0 -1 1	5 -2 -1	3 5 5
4.062	90	0.707	0 -1 1	5 -2 -2	4 5 5
4.123	90	1	1 0 0	0 4 -1	0 1 4
4.301	96.68	0.707	0 -1 1	6 0 -1	1 6 6
4.637	90	0.707	-1 1 0	-3 -3 5	5 5 6
4.95	84.2	0.707	0 -1 1	6 -3 -2	5 6 6
5	90	1	1 0 0	0 4 -3	0 3 4
5.099	90	1	1 0 0	0 5 -1	0 1 5
5.385	90	1	1 0 0	0 5 -2	0 2 5
5.831	90	1	1 0 0	0 5 -3	0 3 5
6.083	90	1	1 0 0	0 6 -1	0 1 6
6.403	90	1	1 0 0	0 5 -4	0 4 5
7.81	90	1	1 0 0	0 6 -5	0 5 6

APPENDIX II

SAED Indexing Table of Body-Centered Cubic Structure

BCC (indices are computed up to 6)

a = 1, b = 1, c = 1, alpha = 90°, beta = 90°, gamma = 90°

D1(max)	h	k	l
0.707	-1	1	0
0.5	2	0	0
0.408	2	1	-1
0.316	-3	1	0
0.288	2	2	-2
0.267	3	1	-2

R2/R1	Angle	D1(max)	(H1 K1 L1)	(H2 K2 L2)	[U V W]
1	60	0.707	-1 1 0	-1 0 1	1 1 1
1	80.41	0.408	2 1 -1	-1 2 -1	1 3 5
1	73.4	0.267	3 1 -2	-1 3 -2	2 4 5
1	90	0.707	1 1 0	-1 1 0	0 0 1
1.08	90	0.289	2 2 -2	-3 2 -1	1 4 5
1.08	72.02	0.289	2 2 -2	-2 3 -1	2 3 5
1.095	68.58	0.316	-3 1 0	-2 -2 2	1 3 4
1.195	90	0.267	1 -3 2	4 0 -2	3 5 6
1.195	68.99	0.267	2 -3 1	4 0 -2	3 4 6
1.225	114.09	0.5	2 0 0	-1 2 -1	0 1 2
1.291	75.04	0.408	1 -2 1	3 0 -1	1 2 3
1.342	107.35	0.316	0 -3 1	4 1 -1	1 2 6
1.354	75.75	0.289	2 2 -2	-3 3 -2	1 5 6
1.414	90	0.707	0 -1 1	2 0 0	0 1 1
1.414	106.43	0.316	-3 1 0	0 -4 2	1 3 6
1.414	81.87	0.316	-3 0 1	0 -4 2	2 3 6
1.528	90	0.408	2 1 -1	-2 3 -1	1 2 4
1.581	90	0.5	2 0 0	0 3 -1	0 1 3
1.612	90	0.316	-3 0 1	1 -4 3	2 5 6
1.732	73.22	0.707	-1 1 0	-2 -1 1	1 1 3
1.826	79.48	0.408	1 -2 1	4 0 -2	2 3 4
1.826	90	0.408	1 2 -1	-4 2 0	1 2 5
1.871	105.5	0.5	2 0 0	-1 3 -2	0 2 3
2.121	103.63	0.5	2 0 0	-1 4 -1	0 1 4
2.236	102.92	0.707	0 -1 1	3 0 -1	1 3 3
2.38	81.95	0.408	1 -2 1	5 0 -3	3 4 5
2.449	90	0.707	-1 1 0	-2 -2 2	1 1 2
2.449	97.82	0.408	2 1 -1	-4 4 -2	1 4 6
2.55	101.31	0.5	2 0 0	-1 4 -3	0 3 4
2.55	90	0.5	2 0 0	0 5 -1	0 1 5
2.646	79.11	0.707	-1 1 0	-3 -2 1	1 1 5
2.739	100.52	0.5	2 0 0	-1 5 -2	0 2 5
2.915	90	0.5	2 0 0	0 5 -3	0 3 5
2.944	83.5	0.408	1 -2 1	6 0 -4	4 5 6

R2/R1	Angle	D1(max)	(H1 K1 L1)	(H2 K2 L2)	[U V W]
3	90	0.707	0 -1 1	4 -1 -1	1 2 2
3.082	99.34	0.5	2 0 0	-1 6 -1	0 1 6
3.24	98.88	0.5	2 0 0	-1 5 -4	0 4 5
3.317	81.33	0.707	-1 1 0	-3 -2 3	3 3 5
3.606	97.97	0.707	0 -1 1	5 0 -1	1 5 5
3.873	82.58	0.707	0 -1 1	5 -2 -1	3 5 5
3.937	97.3	0.5	2 0 0	-1 6 -5	0 5 6
4.123	90	0.707	-1 1 0	-3 -3 4	2 2 3
4.243	90	0.707	-1 1 0	-4 -4 2	1 1 4
4.69	90	0.707	0 -1 1	6 -2 -2	2 3 3
5.745	90	0.707	-1 1 0	-5 -5 4	2 2 5
5.745	90	0.707	0 -1 1	8 -1 -1	1 4 4
5.831	90	0.707	-1 1 0	-4 -4 6	3 3 4
6.164	90	0.707	-1 1 0	-6 -6 2	1 1 6
6.403	90	0.707	0 -1 1	8 -3 -3	3 4 4
7.348	90	0.707	0 -1 1	10 -2 -2	2 5 5
7.55	90	0.707	-1 1 0	-5 -5 8	4 4 5
8.124	90	0.707	0 -1 1	10 -4 -4	4 5 5
8.544	90	0.707	0 -1 1	12 -1 -1	1 6 6
9.274	90	0.707	-1 1 0	-6 -6 10	5 5 6
9.849	90	0.707	0 -1 1	12 -5 -5	5 6 6

APPENDIX III

SAED Indexing Table of Face-Centered Cubic Structure

FCC (indices are computed up to 6)

a = 1, b = 1, c = 1, alpha = 90°, beta = 90°, gamma = 90°

D1(max)	h	k	l
0.577	1	-1	1
0.5	2	0	0
0.353	-2	2	0
0.301	3	1	-1
0.229	3	-3	1
0.223	-4	2	0
0.204	4	2	-2
0.166	4	-4	2

R2/R1	Angle	D1(max)	(H1 K1 L1)	(H2 K2 L2)	[U V W]
1	109.47	0.577	1 -1 1	1 1 -1	0 1 1
1	60	0.354	-2 2 0	-2 0 2	1 1 1
1	113.58	0.224	-4 2 0	0 -4 2	1 2 4
1	84.78	0.302	3 1 -1	-1 3 -1	1 2 5
1	80.41	0.204	4 2 -2	-2 4 -2	1 3 5
1	116.39	0.167	4 -4 2	2 4 -4	2 5 6
1	118.27	0.229	3 -3 1	1 3 -3	3 5 6
1	90	0.5	2 0 0	0 2 0	0 0 1
1.095	100.52	0.224	-4 0 2	2 -4 2	2 3 4
1.173	64.76	0.354	-2 2 0	-3 -1 1	1 1 4
1.173	90	0.354	0 -2 2	3 -1 -1	2 3 3
1.225	97.82	0.204	4 2 -2	-4 4 -2	1 4 6
1.314	110.23	0.302	3 1 -1	-3 3 -1	1 3 6
1.314	78.02	0.302	-3 1 1	-1 -3 3	3 4 5
1.342	72.65	0.224	-4 2 0	-4 -4 2	1 2 6
1.342	90	0.224	-4 2 0	-2 -4 4	2 4 5
1.414	98.13	0.224	0 -4 2	6 0 -2	2 3 6
1.472	83.5	0.204	2 -4 2	6 0 -4	4 5 6
1.541	90	0.354	-2 2 0	-3 -3 1	1 1 6
1.541	71.07	0.354	-2 2 0	-3 -1 3	3 3 4
1.581	108.43	0.354	0 -2 2	4 0 -2	1 2 2
1.612	75.64	0.224	-4 0 2	0 -6 4	3 4 6
1.633	90	0.577	1 1 -1	-2 2 0	1 1 2
1.658	107.55	0.5	2 0 0	-1 3 -1	0 1 3
1.732	73.22	0.354	-2 2 0	-4 -2 2	1 1 3
1.837	90	0.354	0 -2 2	5 -1 -1	2 5 5
2.092	76.17	0.354	0 -2 2	5 -3 -1	4 5 5
2.121	76.37	0.354	-2 2 0	-4 -2 4	2 2 3
2.236	102.92	0.354	0 -2 2	6 0 -2	1 3 3
2.236	90	0.5	2 0 0	0 4 -2	0 1 2
2.318	90	0.354	-2 2 0	-3 -3 5	5 5 6
2.517	82.39	0.577	1 1 -1	-3 3 -1	1 2 3

R2/R1	Angle	D1(max)	(H1 K1 L1)	(H2 K2 L2)	[U V W]
2.598	101.1	0.5	2 0 0	-1 5 -1	0 1 5
2.646	79.11	0.354	-2 2 0	-6 -4 2	1 1 5
2.915	99.87	0.354	0 -2 2	8 0 -2	1 4 4
2.915	80.13	0.354	-2 2 0	-6 -4 4	2 2 5
2.958	99.73	0.5	2 0 0	-1 5 -3	0 3 5
3.24	81.12	0.354	0 -2 2	8 -4 -2	3 4 4
3.317	81.33	0.354	-2 2 0	-6 -4 6	3 3 5
3.416	95.6	0.577	1 1 -1	-5 3 -1	1 3 4
3.606	97.97	0.354	0 -2 2	10 0 -2	1 5 5
3.606	90	0.5	2 0 0	0 6 -4	0 2 3
3.808	82.45	0.354	-2 2 0	-6 -4 8	4 4 5
3.873	82.58	0.354	0 -2 2	10 -4 -2	3 5 5
4.123	90	0.5	2 0 0	0 8 -2	0 1 4
4.123	85.36	0.577	1 1 -1	-5 5 -1	2 3 5
4.301	96.68	0.354	0 -2 2	12 0 -2	1 6 6
4.32	90	0.577	1 1 -1	-6 4 -2	1 4 5
4.95	84.2	0.354	0 -2 2	12 -6 -4	5 6 6
5	90	0.5	2 0 0	0 8 -6	0 3 4
5.26	86.37	0.577	1 1 -1	-7 5 -3	1 5 6
5.385	90	0.5	2 0 0	0 10 -4	0 2 5
6.083	90	0.5	2 0 0	0 12 -2	0 1 6
6.403	90	0.5	2 0 0	0 10 -8	0 4 5
7.81	90	0.5	2 0 0	0 12 -10	0 5 6

APPENDIX IV

SAED Indexing Table of Close-Packed Hexagonal Structure

HCP (indices are computed up to 4)

a = 1, b = 1, c = 1.633, alpha = 90°, beta = 90°, gamma = 120°

D1(max)	(h	k	l)
1.633	0	0	1
0.866	1	0	0
0.765	-1	0	1
0.594	1	0	2
0.5	-2	1	0
0.478	1	1	-1
0.426	1	-2	2

R2/R1	Angle	D1(max)	(H1	K1	L1)	(H2	K2	L2)	[U	V	W]
1	72.9	0.594	-1	0	2	0	1	2	-2	2	-1
1	99.83	0.765	-1	0	1	1	-1	1	1	2	1
1	99.83	0.765	-1	0	1	0	1	1	-1	1	-1
1	60	0.866	1	0	0	0	1	0	0	0	1
1	72.9	0.594	-1	0	2	1	-1	2	2	4	1
1.019	82.31	0.426	-1	2	2	-2	0	1	2	-3	4
1.037	101.12	0.478	1	1	1	-1	0	3	3	-4	1
1.046	118.56	0.5	1	1	0	-2	1	1	1	-1	3
1.046	61.44	0.5	-2	1	0	-1	-1	1	1	2	3
1.085	90	0.5	1	1	0	-1	1	3	3	-3	2
1.085	117.44	0.5	1	1	0	-1	0	3	3	-3	1
1.121	104.76	0.478	1	1	1	-2	1	2	1	-4	3
1.132	63.79	0.866	-1	1	0	-1	0	1	1	1	1
1.132	63.79	0.866	1	0	0	0	1	-1	0	1	1
1.142	85.7	0.478	-2	1	1	0	2	1	-1	2	-4
1.142	85.7	0.478	1	1	-1	-2	2	-1	1	3	4
1.142	94.3	0.478	1	-2	1	2	0	-1	2	3	4
1.173	115.24	0.5	1	1	0	-2	1	2	2	-2	3
1.173	64.76	0.5	-2	1	0	-1	-1	2	2	4	3
1.195	90	0.5	1	1	0	-2	2	1	1	-1	4
1.195	90	0.5	-2	1	0	0	-2	1	1	2	4
1.243	77.7	0.594	-1	1	2	1	1	1	-1	3	-2
1.243	102.3	0.594	0	-1	2	2	-1	-1	3	4	2
1.243	110.8	0.594	-1	0	2	1	1	1	-2	3	-1
1.243	77.7	0.594	0	-1	2	2	-1	1	1	4	2
1.288	87.83	0.765	-1	0	1	1	-1	2	1	3	1
1.288	87.83	0.765	-1	0	1	0	1	2	-1	2	-1
1.288	92.17	0.765	1	-1	1	1	0	-2	2	3	1
1.354	111.67	0.5	1	1	0	-1	0	4	4	-4	1
1.393	97.28	0.594	-1	0	2	1	1	2	-2	4	-1
1.419	98.34	0.594	0	1	2	-2	0	1	1	-4	2
1.458	69.94	0.866	-1	1	0	-1	0	2	2	2	1
1.458	69.94	0.866	1	0	0	0	1	-2	0	2	1

R2/R1	Angle	D1(max)	(H1 K1 L1)			(H2 K2 L2)			[U V W]		
1.475	90	0.5	1	1	0	-2	2	3	3	-3	4
1.53	90	0.765	-1	1	1	1	1	0	-1	1	-2
1.53	90	0.765	0	-1	1	2	-1	0	1	2	2
1.581	108.43	0.5	1	1	0	-2	1	4	4	-4	3
1.66	80.7	0.765	-1	0	1	0	1	3	-1	3	-1
1.66	99.3	0.765	1	-1	1	1	0	-3	3	4	1
1.66	80.7	0.765	-1	0	1	1	-1	3	1	4	1
1.753	79.37	0.594	0	1	2	-2	0	3	3	-4	2
1.794	75.84	0.765	0	1	1	-2	1	2	1	-2	2
1.794	104.16	0.765	1	-1	1	1	1	-2	1	3	2
1.794	75.84	0.765	-1	0	1	1	-2	2	2	3	2
1.811	90	0.866	1	0	0	-1	2	-1	0	1	2
1.811	90	0.866	-1	1	0	-1	-1	1	1	1	2
1.815	97.45	0.594	-1	1	2	2	1	0	-2	4	-3
1.879	74.57	0.866	-1	1	0	-1	0	3	3	3	1
1.879	74.57	0.866	1	0	0	0	1	-3	0	3	1
1.886	90	1.633	0	0	1	1	0	0	0	1	0
1.886	90	1.633	0	0	1	1	-1	0	1	1	0
2.072	76.38	0.765	-1	0	1	0	1	4	-1	4	-1
2.258	93.1	0.765	-1	0	1	0	2	3	-2	3	-2
2.337	99.61	0.765	-1	1	1	2	1	0	-1	2	-3
2.337	99.61	0.765	0	-1	1	3	-1	0	1	3	3
2.337	80.39	0.765	0	-1	1	3	-2	0	2	3	3
2.345	77.69	0.866	-1	1	0	-1	0	4	4	4	1
2.345	77.69	0.866	1	0	0	0	1	-4	0	4	1
2.352	90	0.866	-1	1	0	-1	-1	3	3	3	2
2.352	90	0.866	1	0	0	-1	2	-3	0	3	2
2.518	88.89	0.765	0	1	1	-3	1	2	1	-3	3
2.518	91.11	0.765	1	-1	1	2	1	-2	1	4	3
2.518	88.89	0.765	-1	0	1	2	-3	2	3	4	3
2.698	79.32	0.866	-1	1	0	-2	-1	1	1	1	3
2.698	79.32	0.866	1	0	0	-1	3	-1	0	1	3
2.727	84.35	0.765	0	1	1	-3	1	3	2	-3	3
2.85	79.9	0.866	1	0	0	-1	3	-2	0	2	3
2.85	79.9	0.866	-1	1	0	-2	-1	2	2	2	3
3.096	85.93	0.765	-1	1	1	2	2	1	-1	3	-4
3.096	94.07	0.765	0	-1	1	4	-2	-1	3	4	4
3.096	85.93	0.765	0	-1	1	4	-2	1	1	4	4
3.246	95.17	0.765	-1	0	1	0	3	4	-3	4	-3
3.266	90	1.633	0	0	1	2	-1	0	1	2	0
3.266	90	1.633	0	0	1	1	1	0	-1	1	0
3.32	95.9	0.765	0	1	1	-4	1	2	1	-4	4
3.391	81.52	0.866	1	0	0	-1	3	-4	0	4	3
3.391	81.52	0.866	-1	1	0	-2	-1	4	4	4	3
3.504	90	0.866	-1	1	0	-2	-2	1	1	1	4
3.504	90	0.866	1	0	0	-2	4	-1	0	1	4
3.696	88.49	0.765	0	1	1	-4	1	4	3	-4	4
3.812	90	0.866	1	0	0	-2	4	-3	0	3	4
3.812	90	0.866	-1	1	0	-2	-2	3	3	3	4
4.989	90	1.633	0	0	1	3	-2	0	2	3	0
4.989	90	1.633	0	0	1	2	1	0	-1	2	0
4.989	90	1.633	0	0	1	3	-1	0	1	3	0
6.799	90	1.633	0	0	1	4	-1	0	1	4	0
6.799	90	1.633	0	0	1	4	-3	0	3	4	0
6.799	90	1.633	0	0	1	3	1	0	-1	3	0
8.219	90	1.633	0	0	1	3	2	0	-2	3	0
8.641	90	1.633	0	0	1	4	1	0	-1	4	0
11.47	90	1.633	0	0	1	4	3	0	-3	4	0

Illustration Credits

All the illustrations of this book have been prepared by the author with the following exceptions or reprints from the previously publications:

Fig. 4.14—AIP Publishing LLC.

Fig. 2.3—American Chemical Society.

Fig. 2.10(d) and (e), Fig. 4.11, Fig. 4.12—Cambridge University Press.

Fig. 2.12, Fig. 2.16(g) and (h), Fig. 4.13, Fig. 4.15, Fig. 4.18, Fig. 5.13–5.20—Elsevier.

Fig. 2.18(a–e)—JEOL Ltd.

Fig. 2.14(b) and (c)—John Wiley and Sons.

Fig. 4.8—Royal Society of Chemistry.

Fig. 4.16, Fig. 4.20, Fig. 5.6—Springer.

Fig. 2.10(c)—Taylor & Francis.

Index

Aberration
  chromatic, 62–63
  spherical, 61–62
Accelerating voltage effect on mass-thickness contrast, 110
Air drying, 18
Airy disk, 2, 3
Airy pattern. *See* Airy disk
Amplitude contrast. *See* Scattering contrast
Anticontamination device (ACD), 56, 79
Aperture
  alignment, 68–69
  condenser, 52–55
  diffraction, 57–58
  objective, 55–57
Astigmatism, 65–67
Atomic force microscope (AFM)
  vs. transmission electron microscope, 8
Auger electron spectroscopy (AES), 5
Auger electrons, signals of, 5

Backscattered electrons, signals of, 5
Backscatter imaging detectors (BSI), 5
Bare grids, 19
Beam shift, 60–61
Beam tilt, 60–61
Bend contours, 122
  formation of, 123
Biological samples, with TEM, 36–41
  cells and tissue samples, 39–41
  particulate samples, 37–39
Bragg-diffracted beam intensity, 117–120
Bragg's law, 7, 82, 83
Burgers vector, 127

Calibration
  camera length, 71–74
  magnetic rotation, 75
  magnification, 69–71
Camera
  length calibration, 71–74
  viewing, 59–60
Cathodoluminescence (CL), 5
Cells and tissue samples, preparation of, 39–41
  dehydration, 41
  embedding, 41
  fixation, 40
  sample extraction, 40
  staining, 41
  substitution, 41
  TEM observation, 41
  thin sectioning, 41
Central dark-field imaging (CDF), 113–115
Ceramics, 13, 14
Chromatic aberration, 62–63
Collecting, microtomy procedure, 34
Composites, 13, 14
Compound diffraction patterns
  double diffraction, 98–100
  multiple phases, 96–98
  twins, 92–96
Condenser apertures, construction of, 52–55
Condenser lenses, construction of, 52–55
Contrast, 109–110
  with diffraction, 111–137
  with mass-thickness, 110–111
Chemical analysis, 6, 10
Critical point drying, 18–19
Crystallography, 75
Cutting, ion milling procedure, 21

Depth of field, 63–64
Depth of focus, 63–64
Diffraction aperture, 57–58
Diffraction contrast, 111–137
  bend contours, 122
  Bragg-diffracted beam intensity, 117–120
  central dark-field imaging, 113–115
  dislocations, 127–137
  formation of, 111–113
  planar defects, 125–126
  thickness fringes, 120–122
  two-beam condition, 115–117
  weak-beam dark-field imaging, 122–125
Dimpling, ion milling procedure, 22, 23
Dislocations, 127–137
  in BCC crystal, 130
  in FCC crystal, 129
  images in Ni-base superalloy, 124
Double diffraction, 98–100
Drilling, ion milling procedure, 21
Ductile TEM foils, 122

Edge dislocations, 127
Effective excitation error, 118
Electromagnetic lens, construction of, 49–52
Electron backscatter diffraction (EBSD), 8
Electron beam, heat generated by, 6
Electron diffraction, 81–105
  compared with X-ray diffraction, 88–90
  experimental procedures, 101–103
  formation of, 82–84
  patterns, indexing
    compound patterns – double diffraction, 98–100
    compound patterns – multiple phases, 96–98
    compound patterns – twins, 92–96
    powder patterns, 88–90
    single-crystal diffraction patterns, 90–92
  patterns, simulation of, 103–105
  reciprocal space, 84–88
Electron energy-loss spectroscopy (EELS), 5, 45
Electron gun, construction of, 45–49
Electron microprobe analyzer (EMPA) or Electron probe microanalyzer (EPMA), 1
  vs. transmission electron microscope (TEM), 7–8, 10
Electron microscopy (EM), 1
Electrons interactions, with specimen, 4–6
Electropolishing, 26–30, 120
Embedding, microtomy procedure, 33
Energy-dispersive spectroscopy (EDS), 15
Excitation error, 118
Extinction distance, 118–119
  of BCC crystals, 120
  of FCC and diamond-structure crystals, 120
  of HCP crystals, 120

Fast Fourier transformation (FFT), 66–67
Field-emission gun (FEG), 45
  construction of, 48–49
Focused ion beam (FIB), 30–31
Focus of lens, 52
Freeze drying, 18

Grinding, ion milling procedure, 21

Hexamethyldisilazane (HMDS), 18–19
HREM image, 135
  dislocation pairs and single dislocations, 137
  of dislocation pairs of segment 3, 136

Imaging
contrast, 109–110
with diffraction contrast, 111–137
with mass-thickness contrast, 110–111
Intermediate lens, 57–58
Ion milling, 20–26, 120

Laue zone axis, 116
Lens
condenser, 52–55
electromagnetic, 49–52
focus of, 52
intermediate, 57–58
objective, 55–57
optical, 50
projector, 59
Lift-out method, in FIB, 30–31
example of, 31, 32
Light microscope (LM), 1
vs. transmission electron microscope (TEM), 7, 8–9, 10

Magnetic rotation calibration, 75
Magnification calibration, 69–71
Mass-thickness contrast, imaging with, 110–111
Material samples, with TEM, 14–36
electropolishing, 26–30
focused ion beam, 30–31
ion milling, 20–26
microtomy, 31–36
TEM grids, 15–20
Metals and alloys, 13, 14
Microtomy, procedure of, 31–36
Multiple phases, compound diffraction patterns of, 96–98

Negative staining process, 37–39
Ni-base superalloy
dislocations images in, 124
stacking faults in, 127
Numerical aperture (NA), 2

Objective aperture, construction of, 55–57
Objective lens, construction of, 55–57
Optical lens, 50

Particulate samples, 37–39
Phase contrast, 110
Planar defects, 125–126
Planar unit cell, 135
Projector lens, 59
Projector Lens Shift, 114

Rayleigh criterion, 2, 3
Reciprocal space, 84–88
Resolution, of TEM, 2–4
methods to improve, 3–4
numerical aperture (NA), 2
Rayleigh criterion, 2, 3
Sample preparation, with TEM, 13–41
biological samples, 36–41
material samples, 14–36
sample requirements, 13

Scanning Auger microprobe (SAM), 1
vs. transmission electron microscope, 7–8, 10
Scanning electron microscope (SEM), 1
carbon nano fiber samples using, 11
vs. transmission electron microscope, 7–8, 10
Scanning TEM (STEM) mode, 110
Scattering contrast, 110
Screen, viewing, 59–60
Screw dislocations, 127
Secondary electron imaging (SEI), 5
Secondary electrons, signals of, 5
Sectioning, microtomy procedure, 34
Selected-area electron diffraction (SAED), 72, 75, 81, 84, 101, 104, 112–117
aperture, 58
compound patterns, 96–100

Selected-area electron diffraction (SAED) (*Continued*)
indexing table
of body-centered cubic structure, 141–142
of close-packed hexagonal structure, 145–146
of face-centered cubic structure, 143–144
of primitive cubic structure, 139–140
powder patterns, 88–90
single crystal diffraction patterns, 90–91
spot intensities, 101, 102
twinned pattern, 92–96
Simulation, of diffraction patterns, 103–105
Single-crystal diffraction patterns, 83, 90–92
Slide projector
vs. transmission electron microscope, 7, 9
Solid thin film samples, 24–26
cross-sectional view sample preparation, 25–26
plane-view sample preparation, 24–25
Specimen crystallinity, 81
Specimen height, 64–65
Spherical aberration, 61–62
Support film, 15

Thermionic gun, construction of, 45–47, 49
Thickness fringes, 120–122
Transmission electron microscope (TEM)
carbon nano fiber samples using, 11
electrons with specimen, interactions of, 4–6
operating procedures of, 76–79
air drying, 18
critical point drying, 18–19
freeze drying, 18
image contrast in, 110
introduction to, 1–11
operating procedures of, 76–79
alignments, 77–78
data recording, 78
finishing, 78–79
specimen loading and unloading, 76
startup, 76
vs. other microscopy techniques, 6–11
resolution of, 2–4
Transmitted electrons, in TEM, 4–5
Trimming, microtomy procedure, 33
Twin-jet electropolishing, 27–29
Twins, compound diffraction patterns of, 92–96
Two-beam condition, 115–117

Visible lights, in TEM, 5

Wavelength-dispersive spectroscopy (WDS), 6
Weak-beam dark-field imaging (WBDF), 122–125

X-ray diffraction (XRD)
compared with electron diffraction, 88–90
X-ray energy-dispersive spectroscopy (XEDS), 6
X-rays, in TEM, 4

Z-contrast, 110
Zone axis pattern, 115

OTHER TITLES IN OUR MATERIALS CHARACTERIZATION AND ANALYSIS COLLECTION

C. Richard Brundle, *Editor*

- *Secondary Ion Mass Spectrometry: Applications for Depth Profiling and Surface Characterization* by Fred Stevie
- *Auger Electron Spectroscopy: Practical Application to Materials Analysis and Characterization of Surfaces, Interfaces, and Thin Films* by John Wolstenholme
- *Spectroscopic Ellipsometry: Practical Application to Thin Film Characterization* by Harland G. Tompkins and James N. Hilfiker
- *A Practical Guide to Transmission Electron Microscopy, Volume 2: Advanced Microscopy* by Zhiping Luo

Momentum Press is one of the leading book publishers in the field of engineering, mathematics, health, and applied sciences. Momentum Press offers over 30 collections, including Aerospace, Biomedical, Civil, Environmental, Nanomaterials, Geotechnical, and many others.

Momentum Press is actively seeking collection editors as well as authors. For more information about becoming an MP author or collection editor, please visit http://www.momentumpress.net/contact

Announcing Digital Content Crafted by Librarians

Momentum Press offers digital content as authoritative treatments of advanced engineering topics by leaders in their field. Hosted on ebrary, MP provides practitioners, researchers, faculty, and students in engineering, science, and industry with innovative electronic content in sensors and controls engineering, advanced energy engineering, manufacturing, and materials science.

Momentum Press offers library-friendly terms:

- perpetual access for a one-time fee
- no subscriptions or access fees required
- unlimited concurrent usage permitted
- downloadable PDFs provided
- free MARC records included
- free trials

The **Momentum Press** digital library is very affordable, with no obligation to buy in future years.

For more information, please visit **www.momentumpress.net/library** or to set up a trial in the US, please contact **mpsales@globalepress.com.**

EBOOKS FOR THE ENGINEERING LIBRARY

Create your own Customized Content Bundle — the more books you buy, the higher your discount!

THE CONTENT

- *Manufacturing Engineering*
- *Mechanical & Chemical Engineering*
- *Materials Science & Engineering*
- *Civil & Environmental Engineering*
- *Electrical Engineering*

THE TERMS

- *Perpetual access for a one time fee*
- *No subscriptions or access fees*
- *Unlimited concurrent usage*
- *Downloadable PDFs*
- *Free MARC records*

For further information, a free trial, or to order, contact:
sales@momentumpress.net

A Practical Guide to Transmission Electron Microscopy

Fundamentals

Zhiping Luo

Transmission electron microscope (TEM) is a very powerful tool for characterizing various types of materials. Using a light microscope, the imaging resolution is at several hundred nanometers, and for a scanning electron microscope at several nanometers. The imaging resolution of the TEM, however, can routinely reach several angstroms on a modem instrument. In addition, the TEM can also provide material structural information, since the electrons penetrate through the thin specimens, and chemical compositional information due to the strong electron specimen atom interactions.

This book provides a concise practical guide to the TEM user, starting from the beginner level, including upper-division undergraduates, graduates, researchers, and engineers, on how to learn TEM efficiently in a short period of time. It covers most of the areas using TEM, including the instrumentation, sample preparation, diffraction, imaging, analytical microscopy, and some newly developed advanced microscopy techniques. This book may serve as a textbook for a TEM course or workshop, or a reference book for the TEM user to improve their TEM skills.

Dr. Zhiping Luo is an associate professor in the department of chemistry and physics at Fayetteville State University, North Carolina. He started electron microscopy in early 1990s. While he was conducting his PhD thesis work on rare earths-containing magnesium alloys, he encountered with fine complex intermetallic phases, so he used TEM as a major research method. From 1996 to 1997 he was at Okayama University of Science, Japan as a postdoctoral researcher to study electron microscopy with Professor H. Hashimoto. In 1998, he moved to materials science division, Argonne National Laboratory, as a visiting scholar and became the assistant scientist in 2001. Between 2001 and 2012, he worked as a TEM instrumental scientist at the Microscopy and Imaging Center at Texas A&M University, where he taught TEM courses and trained many TEM users. Dr. Luo has authored over 200 articles in peer-reviewed journals, and most of them involved TEM investigations.

MOMENTUM PRESS
ENGINEERING